A Climate-friendly Energy Future: Prospects for Wind

A Climate-friendly Energy Future: Prospects for Wind

A dissertation presented

by

Junling Huang

to

The school of Engineering and Applied Sciences

in partial fulfillment of the requirements

for the degree of

Doctor of Philosophy

in the subject of

Engineering Sciences

Harvard University

Cambridge, Massachusetts

April 2014

Dissertation Advisor: Michael B. McElroy Junling Huang

A Climate-friendly Energy Future: Prospects for Wind

Abstract

The objective of this thesis is to evaluate the potential for wind as an alternative energy source to replace fossil fuels and reduce global CO_2 emissions. From 1995 to 2007, fossil fuels as the major energy source accounted for an addition of 89.3 Gt of carbon to the atmosphere over this period, 29 % of which was transferred to the ocean, 15 % to the global biosphere, with the balance (57 %) retained in the atmosphere. Building a low-carbon and climate-friendly energy system is becoming increasingly urgent to combat the threat of global warming.

Onshore wind resources in the contiguous US could readily accommodate present and anticipated future US demand for electricity. The problem with the output from a single wind farm located in any particular region is that it is variable on time scales ranging from minutes to days posing difficulties to incorporate relevant outputs into an integrated power system. The issue of interconnection of wind farms is studied with specific attention to the physical factors that determine the temporal variability of winds in the near surface region of the atmosphere.

From a global perspective, generation of electricity from wind is determined ultimately by the balance between the production and dissipation of kinetic energy in the atmosphere. The origin of wind energy from 1979 to 2010 is investigated. The atmosphere acts as a thermal engine to produce wind energy, absorbing heat at higher temperatures (approximately 256 K), releasing heat at lower temperatures (approximately 253 K), as a consequence producing wind energy at a rate of 2.45 W/m^2, with a thermodynamic efficiency of 1.03 %.

The continuous blowing of wind is maintained by the thermodynamic instability of the atmospheric system. A framework is constructed to probe the relationship between the energy and entropy of the atmosphere, and to quantify two variables, the maximum work and the maximum increase in entropy which represent the thermodynamic instability. A large value for either variable corresponds to high thermodynamic instability and large potential for the atmosphere to produce wind energy. The results offer a fresh perspective on the energetics of the atmosphere.

Table of Contents

List of Figures

List of Tables

Acknowledgements

I own an enormous debt of gratitude to my advisor, *Michael B. McElroy*, who introduced me to the challenging and exciting issues of renewable energy in the context of global warming and taught me how to do research in an enjoyable way. I have benefited tremendously from his broad and profound knowledge. I am really grateful for his generous support and patient guidance on every stage of my progress.

I would like to thank my committee members: *James G. Anderson*, *Michael J. Aziz*, *Zhiming Kuang* for being supportive and offering me numerous insightful suggestions. A special thank to *Brian F. Farrell*, *Eli Tziperman*, *Michael J. Aziz*, and *Zhiming Kuang* for offering me instructive guidance throughout my research. I would like to thank *Chris P. Nielson* and *Xi Lu* for providing me with timely help and making my work connect to other disciplines. I have been privileged to work with many remarkable people at Harvard, with whom I have shared ideas, working experiences, and friendship over the past years. Many thanks to *Cecilia McCormack*, *Brenda Mathieu*, *William Walker* and *Jill Larson* for their administrative assistance.

I am deeply grateful to my parents, *Ming Huang* and *Dinghua Shen* for their unfailing love and continuous encouragement through my life. I sincerely thank *Yixiao Zhou* for her wholehearted support and daily encouragement.

I would like to acknowledge funding from the Graduate Consortium on Energy and Environment at Harvard and the National Science Foundation.

To my

Mother, Ming Huang

and

Father, Dinghua Shen

Chapter 1

Overview of this dissertation

The present research is motivated by an ambition to evaluate the potential of wind energy as an alternative energy source to replace fossil fuels and reduce emissions of the greenhouse gas CO_2. The dissertation begins with an analysis of the contemporary and historical budget of atmospheric CO_2 (see Chapter 2). The analysis developed a quantitative understanding of the relative importance of ocean uptake, exchange with the biosphere and combustion of fossil fuel in determining the change in CO_2 that has taken place in the atmosphere over the past hundred years. The results suggest that the contemporary increase in the concentration of CO_2 in the atmosphere is due mainly to emissions associated with the combustion of fossil fuels. Since 1995, approximately $57\ \%$ of the carbon released as a result of the fossil fuel source has persisted in the atmosphere, $29\ \%$ has been transferred to the ocean, and the balance ($15\ \%$) has been absorbed by the biosphere. From a long term perspective, the results indicate that the biosphere was responsible for a net source of CO_2 from 1840 to about 1940, and after 1940, the biosphere switched from a net source to a net sink.

The atmospheric concentration of CO_2 has reached approximately 390 ppm at the end of 2011. The increasing concentration of greenhouse gas in the atmosphere has caused an imbalance in the energy budget of the Earth: it is absorbing more energy from the sun than it is returning to space. The radiative forcing of CO_2 for 2011 relative to 1750 is $1.82\ W/m^2$, reflecting its dominate contribution to the total anthropogenic radiative forcing of $2.29\ W/m^2$ (IPCC 2013). The globally averaged combined land and ocean surface temperature data indicates a warming of $0.85\ K$ over the period 1880 to 2012. Changes in extreme weather and climate

events have been observed since about 1950. If we are to avoid unacceptable future disruption of the global climate system, it will be necessary to constrain future growth in the concentration of the key climate altering gas CO_2.

The U.S. was the second largest CO_2 emitting country in 2012, with the electricity sector accounting for more than a third of total CO_2 emission. Wind energy received special attention in recent years as an abundant and economically competitive energy source. Lu et al. (2009) argued that an onshore network of GE 2.5 MW turbines installed in the contiguous U.S. could supply as much as 16 times total current U.S. demand for electricity. A study by the U.S. Department of Energy concluded that wind could account economically for 20 % of total U.S. demand for electricity by 2030 (DOE 2008). The problem with the output from a single wind farm located in any particular region is that it is variable on time scales ranging from minutes to days posing difficulties to incorporate relevant contributions into the integrated power system. The variability of wind over the Central Plains region considered here is associated primarily with the passage of transient waves with a characteristic time scale of a few days. Using 5 years of assimilated wind data from the Modern Era Retrospective-analysis for Research and Applications (MERRA) compilation covering the period Dec 2002 to Nov 2007, the study on interconnection (see Chapter 3) was conducted with specific attention to the physical factors that determine the temporal variability of winds in the near surface region of the atmosphere. The results show that the high frequency variability of wind-generated power can be eliminated by coupling outputs from 5-10 wind farms dispersed uniformly over the ten state region emphasized in this study. More than 95 % of the variability of the coupled system is concentrated at time scales longer than a day, allowing operators of the overall system to take advantage of multiple day weather forecasts in scheduling projected contributions from wind. The high frequency variability of

outputs from individual wind farms is determined mainly by small scale turbulence associated with local conditions. Combining uncorrelated high frequency outputs from multiple locations serves to markedly reduce the variability of the overall system output.

From a global viewpoint, wind energy has been experiencing rapid growth through the past decade, with total capacity doubling every three years. The global installed wind capacity reached a level of more than $237\ GW$ at the end of 2011, of which approximately $40\ GW$ were added in 2011, the highest level recorded to date. Wind turbines installed worldwide were capable by the end of 2011 of providing $500\ TWh$ of electricity per year, accounting for approximately 3 % of total global production of electricity. A key question is whether there is a physical limit to the extraction of energy from wind. Various groups have attempted to answer this question based on numerical modeling (e.g. Miller et al. 2011; Marvel et al. 2012; Jacobson and Archer 2012; Adams and Keith 2011). There is a notable discrepancy among their results. Answering the question of the ultimate limit of the atmosphere as a source of wind-generated electric power requires a detailed study of the underlying physics of kinetics of the global atmosphere.

Based on MERRA data for the period January 1979 to December 2010, the origin of wind energy is investigated from both mechanical and thermodynamic perspectives (see Chapter 4). The atmosphere acts as a thermal engine, absorbing heat at higher temperatures, approximately $256K$, releasing heat at lower temperatures, approximately $253\ K$. The process produces work at a rate of $2.46\ W/m^2$ sustaining thus the circulation of the atmosphere, with a thermodynamic efficiency of $1.03\ \%$. The analysis indicates upward trends in both kinetic energy production and thermodynamic efficiency over the past 32 years, indicating that wind energy resources may be increasing in the current warming climate.

The circulation of the atmosphere can be split into two components: the zonal mean meridional circulation and the eddies. Accordingly, the production of kinetic energy of wind can be partitioned into a contribution from the meridional circulation and a contribution from eddies (Peixoto and Oort 1992). The meridional circulation consists of three systems: the Hadley system in the tropics, the Ferrel system at mid-latitudes and the Polar system at high-latitudes. An approach was developed to investigate the key thermodynamic properties of the Hadley and Ferrel systems, quantifying them using MERRA data covering the period January 1979 to December 2010 (see Chapter 5). The results indicate that the thermodynamic efficiency of the Hadley system, considered as a heat engine, has been relatively constant over the 32 year period covered by the analysis, averaging 2.6 %. Over the same interval, the power generated by the Hadley regime has risen at an average rate of about 0.51 TW per year, reflecting an increase in energy input to the system consistent with the observed upward trend in tropical sea surface temperatures. The Ferrel system acts as a heat pump with a coefficient of performance of 12.1, consuming kinetic energy at an approximate rate of 275 TW, exceeding the power production of the Hadley system by 77 TW. The Polar meridional cell is too weak to allow its contribution to be calculated following the procedure adopted for the Hadley and Ferrel systems.

Motions of the atmosphere against friction convert kinetic energy of wind to internal energy. This process is thermally irreversible, resulting in an increase in entropy. The continuous production of kinetic energy is maintained as a result of the thermodynamic instability of the atmosphere. A framework is constructed to probe the relationship between energy and entropy of the atmosphere, and quantify two variables, the maximum work and the maximum increase in entropy associated with the thermodynamic instability (see Chapter 6). A large value for either

variable corresponds to high thermodynamic instability and a large potential to produce wind energy. The results offer a fresh perspective on the energetics of the atmosphere.

References

Adams, A. S., and D. W. Keith, 2013: Are global wind power resource estimates overstated? *Environ. Res. Lett.*, **8**, 015021.

DOE, 2008: 20% Wind Energy by 2030: Increasing Wind Energy's Contribution to U.S. Electricity Supply. Washington, DC. Available from: http://www.nrel.gov/docs/fy08osti/41869.pdf

IPCC, 2013: Summary for Policymakers. In: Climate Change 2013: The Physical Science Basis. Contribution of Working Group I to the Fifth Assessment Report of the Intergovernmental Panel on Climate Change [Stocker, T.F., D. Qin, G.-K. Plattner, M. Tignor, S.K. Allen, J. Boschung, A. Nauels, Y. Xia, V. Bex and P.M. Midgley (eds.)]. Cambridge University Press, Cambridge, United Kingdom and New York, NY, USA.

Jacobson, M. Z., and C. L. Archer, 2012: Saturation wind power potential and its implications for wind energy. *Proc. Natl. Acad. Sci.*, **109**, 15679-15684.

Lu, X., M. B. McElroy, and J. Kiviluoma, 2009: Global potential for wind-generated electricity. *Proc. Natl. Acad. Sci.*, **106**, 10933-10938.

Marvel, K., B. Kravitz, and K. Caldeira, 2012: Geophysical limits to global wind power. *Nat. Clim. Change*, **3**, 118-121.

McElroy, M. B., 2010: Challenge of global climate change: Prospects for a new energy paradigm. *Front. Environ. Sci. Engin*. China., **4**, 2-11.

Miller, L. M., F. Gans, and A. Kleidon, 2011: Estimating maximum global land surface wind power extractability and associated climatic consequences. *Earth System Dynamics*, **2**, 1-12.

Peixoto, J. P., and A. H. Oort, 1992: *Physics of climate*. American institute of physics, 520pp.

Chapter 2

The contemporary and historical budget of atmospheric CO_2

[Huang, J., and M. B. McElroy, 2012: The contemporary and historical budget of atmospheric CO_2. *Canadian Journal of Physics*, **90**, 707-716.]

Abstract

Observations of CO_2 and O_2 are interpreted to develop an understanding of the changes in the abundance of atmospheric CO_2 that have arisen over the period 1995 to 2007. Fossil fuels accounted for an addition of 89.3 Gt of carbon to the atmosphere over this time period, 29 % of which was transferred to the ocean, 15 % to the global biosphere, with the balance, 57 %, retained by the atmosphere. Analysis of historical data for CO_2 derived from studies of gases trapped in ice at Law Dome in Antarctica indicate that the biosphere represented a net source of atmospheric CO_2 prior to 1940, switching subsequently to a net sink.

2.1 Introduction

The bulk of the Earth's carbon resides in the sediments. The ocean ranks number two, followed by soils, the atmosphere and the biosphere. The concentration of CO_2 in the atmosphere has varied between about 180 ppm and 280 ppm over much of the past million years or so --- low during glacial epochs, high during the relatively short duration interglacial environments that

punctuated global climate conditions over this interval. The glacial/interglacial variability of atmospheric CO_2 reflects primarily a redistribution of carbon between the atmosphere on the one hand and the combined ocean/biosphere/soil reservoir on the other.

The lifetime of carbon in sediments is measured in hundreds of millions of years. Carbon is returned from sediments to the ocean/atmosphere/biosphere/soil when sediments are uplifted and weathered or when the sediments are drawn down into the mantle and cooked. Return in the latter case occurs in conjunction with hot springs and volcanoes. Changes in sediment cycling rates over time have resulted in a variety of different levels of carbon in the atmosphere and for a wide range of different climate conditions. The lifetime of carbon in the ocean/atmosphere/biosphere/soil reservoir is a few hundred thousand years. We would expect variations in CO_2 occasioned by temporary imbalances in the sediment source/sink to be manifest therefore on time scales at least this long. The challenge at the moment is that demands for the fossil fuels (coal, oil and natural gas) and cement production in our modern economy are seriously accelerating the natural rate at which carbon is returned to the atmosphere from sediments, by more than a factor of 50. It is not surprising under the circumstances that the abundance of CO_2 in the atmosphere is rising rapidly at the present time.

The increase began in the late 18^{th} century roughly coincident with the industrial revolution. It has risen in the interim from a level of about 285 ppm characteristic of typical unperturbed (natural) interglacial conditions to a contemporary value of approximately 400 ppm. There can be little doubt that combustion of fossil fuel has been a major contributor to the recent rise in the abundance of atmospheric CO_2. A portion of the CO_2 added to the atmosphere over the past several hundred years has been absorbed by the ocean. At the same time there have been important changes in the quantity of carbon stored in the biosphere and soils. The early rise in

CO_2 was clearly due to a net release of carbon from the biosphere and most likely also from soils. Conversion of forested land to agriculture in the eastern region of North America in the late 18th and early 19th centuries for example resulted without question in a net transfer of carbon to the atmosphere: the observed increase in the abundance of atmospheric CO_2 in this period exceeds by a significant factor the quantity of CO_2 produced as a consequence of the early use of fossil fuels. As richer soils in the interior of the continent were opened up for development, poorer lands in the east were abandoned and forests were allowed to regrow. Plowing the carbon rich soils of the Mid West resulted almost certainly in an additional net transfer of carbon to the atmosphere. Regrowth of the forests previously depleted in the east would have resulted in a net sink for atmospheric carbon. Closer to present, it is apparent that clearance of land in the tropics and subtropics, deforestation, has contributed an important additional source of atmospheric CO_2. On the other hand, as we shall see, the biosphere/soil system on a global scale is presently responsible for a net sink.

The objective for this paper is to develop a quantitative understanding of the relative importance of ocean uptake, exchange with the biosphere/soil system and combustion of fossil fuel in determining the change in CO_2 that has taken place in the atmosphere over the past several hundred years. The late Charles David Keeling was the early pioneer in developing a high quality record of modern changes in the abundance of atmospheric CO_2. Data from the stations he established on Mauna Loa, Hawaii, and at the South Pole have provided an essentially continuous record of the changes in the abundance of CO_2 at these stations since the late 1950's. Keeling's ambition was to use precise measurements of CO_2 as a window on the carbon cycle. He extended his observations later to include measurements of the isotopic composition of atmospheric CO_2, the ratio of ^{13}C to ^{12}C. The photosynthetic process favors

absorption of ^{12}C over ^{13}C. As a consequence, reduced forms of carbon (carbon in biosphere, soil, and fossil fuel materials) are isotopically light relative to carbon in the atmosphere. Combustion of fossil fuels adds a source of isotopically light carbon to the atmosphere. Net transfer of carbon from the atmosphere to the biosphere (in what follows we use biosphere as a shorthand to indicate the combination of above ground and below ground sources of organic carbon) would result in a net increase in the abundance of ^{13}C relative to ^{12}C in the atmosphere, a net decrease if the biosphere should act as a net source of atmospheric CO_2. Isotopic fractionation associated with transfer of carbon between the atmosphere and ocean is much less than the fractionation associated with exchange between the atmosphere and biosphere.

The isotopic composition of a sample containing carbon (the abundance of ^{13}C relative to ^{12}C) is expressed in terms of a quantity $\delta^{13}C$ defined as follows:

$$\delta^{13}C(\text{‰}) = [\frac{R_{\text{sample}} - R_{\text{standard}}}{R_{\text{standard}}}] \times 10^3 \qquad (2.1)$$

where $\delta^{13}C$ is expressed in parts per thousand ($^0/_{00}$), and R_{sample} and $R_{standard}$ express the molar ratios of ^{13}C relative to ^{12}C in the sample and in a standard gas respectively. Addition of carbon to the atmosphere associated with combustion of fossil fuel has resulted in a net decrease of about 0.7 $^0/_{00}$ in the value of $\delta^{13}C$ for atmospheric CO_2. A number of authors, including Charles David Keeling, have exploited observations of the abundance of CO_2 in the atmosphere in combination with measurements of $\delta^{13}C$ over the past 30 years to distinguish the relative contributions of atmosphere/biosphere and atmosphere/ocean exchange to the overall budget of atmospheric CO_2 (Friedli et al. 1986; Ciais et al. 1995; Battle et al. 2000; Keeling et al. 2001). An alternate approach, based on a combination of measurements for CO_2 together with data on the changing abundance of atmospheric O_2 is adopted for purposes of the present analysis.

The premise of the oxygen approach is basically simple. If you know the concentrations of atmospheric CO_2 and O_2 at time t and if you also know the concentrations at some later time $t+\Delta t$, the question is how you make the transition from the conditions appropriate for time t to those applicable at time $t+\Delta t$. Combustion of fossil fuel is responsible for a net increase in the abundance of CO_2 with an associated decrease in the abundance of O_2. Consider a two dimensional diagram in which one axis is represented by the concentration of CO_2, the other measures the concentration of O_2. If you know the composition of the fossil fuels that are consumed, and this can be determined, you can immediately draw a line indicating the trajectory in the 2-dimensional diagram representing the change attributable to the fossil fuel source. Uptake of CO_2 by the ocean will cause the trajectory to continue along an essentially horizontal path since exchange with the ocean is not expected to result in any significant change in the abundance of O_2 (oxygen is relatively insoluble in the ocean). The challenge then is to arrive at the final destination. Biospheric exchange results in a predictable change in the ratio of the change in CO_2 as compared to the change in O_2 (i.e. the slope of the final segment of the trajectory is predetermined). The procedure, subject to its assumptions, results in a unique determination of the magnitude of the ocean sink and the magnitude of either the source or sink associated with the biosphere. A schematic illustration of this procedure is plotted in Figure 2.1. There is a minor complication to this analysis to be discussed later. The ocean on a short time scale could contribute either a small source or sink for O_2 reflecting a temporary imbalance in rates for photosynthesis and compensatory respiration and decay. Additional release of CO_2 from the ocean to the atmosphere could arise as a result of net warming of surface ocean waters. The assumption is that by averaging data over several (relatively short) years, the limitations imposed by these complications can be minimized. The oxygen approach was developed by another

member of the Keeling family, Charles David's son Ralph. It would not strain credulity too much to assert that a large fraction of what we now know about the contemporary atmospheric CO_2 budget can be attributed to the ingenuity and persistence of a pair of talented individuals from a single family, the Keelings.

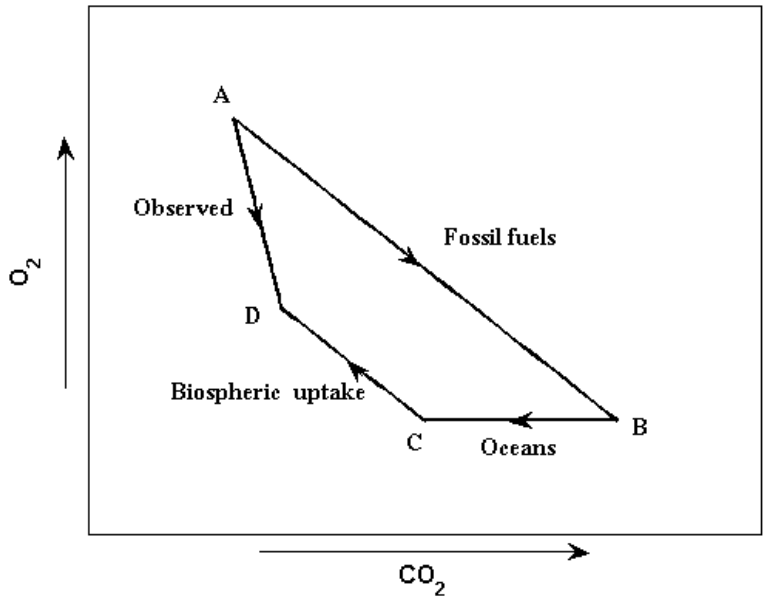

Figure 2.1 Schematic illustration of trends in CO_2 and O_2.

The data on CO_2 and O_2 adopted for this analysis together with information on the emissions of CO_2 from fossil fuel are described in Section 2.2. Results from a global balance model are presented in Section 2.3, which includes an account of the physical and chemical processes regulating uptake of CO_2 by the ocean. The model is applied on a hemispheric basis in Section 2.4. The analysis in Sections 2.3 and 2.4 is limited by the available O_2 data to the time interval 1995-2007. The time horizon is extended in Section 2.5 to cover the period 1840 to 2007 based in this case on consideration of what is known as the air borne fraction, the fraction of CO_2 emitted that persists in the atmosphere rather than being incorporated in the ocean. Summary concluding remarks are presented in Section 2.6.

2.2 Data sources for the study

Our objective here is to develop a record establishing the changes in the global average concentrations of CO_2 and O_2 that have arisen in the past. Observations of O_2 are available only for the period subsequent to 1995. Data from analyses of gases trapped in ice cores allow the record of CO_2 to be extended much further into the past. As indicated above, the time horizon selected for purposes of the studies described in Sections 2.3 and 2.4 is 1995-2007. The time horizon addressed in Section 2.5 extends back to 1840.

To calculate global and hemispheric average concentrations of CO_2 for the recent time period we selected observations from 11 stations covering a latitude domain extending from 82.3 ^{o}N (Alert, NWT, Canada) to the South Pole. The observational CO_2 data used in the research is from Scripps Institute of Oceanography CO_2 program (http://scrippsco2.ucsd.edu/data/data.html). The choice of stations is summarized in Table 1. The stations are located in remote regions such that data from these stations are not expected to be impacted significantly by either local sources or sinks. Measurements from individual stations are assumed to be representative of conditions in the latitude zones in which the stations are located. Hemispheric and global averages were computed by weighting monthly averages of station data in proportion to the surface area of the Earth appropriate for the latitude zones to which the stations were assigned. Trends in global averages and hemispheric contrast computed in this fashion are presented in Figures 2.2a and 2.2b. Measurements of gases trapped in a series of three cores drilled at Law Dome in East Antarctica were used to extend the CO_2 record back to 1830. These data were selected in recognition of the fact that the Law Dome cores are characterized by a relatively high accumulation rates, low concentrations of impurities and regular stratigraphic layering

unperturbed either by surface winds or by ice flow at depth (Etheridge et al. 1996). The ice core results, taken as representative of global average conditions, are displayed in Figure 2.3.

Table 2.1 Stations included in the global & hemispheric CO_2 averaging process.

Station	Latitude (deg.)	Longitude (deg.)	Elevation (m)
Alert, NWT, Canada	82.3 ^{o}N	62.3 ^{o}W	210
Point Barrow, Alaska	71.3 ^{o}N	156.6 ^{o}W	11
La Jolla Pier, California	32.9 ^{o}N	117.3 ^{o}W	10
Baja California Sur, Mexico	23.3 ^{o}N	110.2 ^{o}W	4
Cape Kumukahi, Hawaii	19.5 ^{o}N	154.8 ^{o}W	3
Christmas Island	2.0 ^{o}N	157.3 ^{o}W	2
American Samoa	14.2 ^{o}S	170.6 ^{o}W	30
Kermadec Island	29.2 ^{o}S	177.9 ^{o}W	2
Baring Head, New Zealand	41.4 ^{o}S	174.9 ^{o}E	85
Palmer Station, Antarctica	64.9 ^{o}S	64.0 ^{o}W	10
South Pole	90.0 ^{o}S		2810

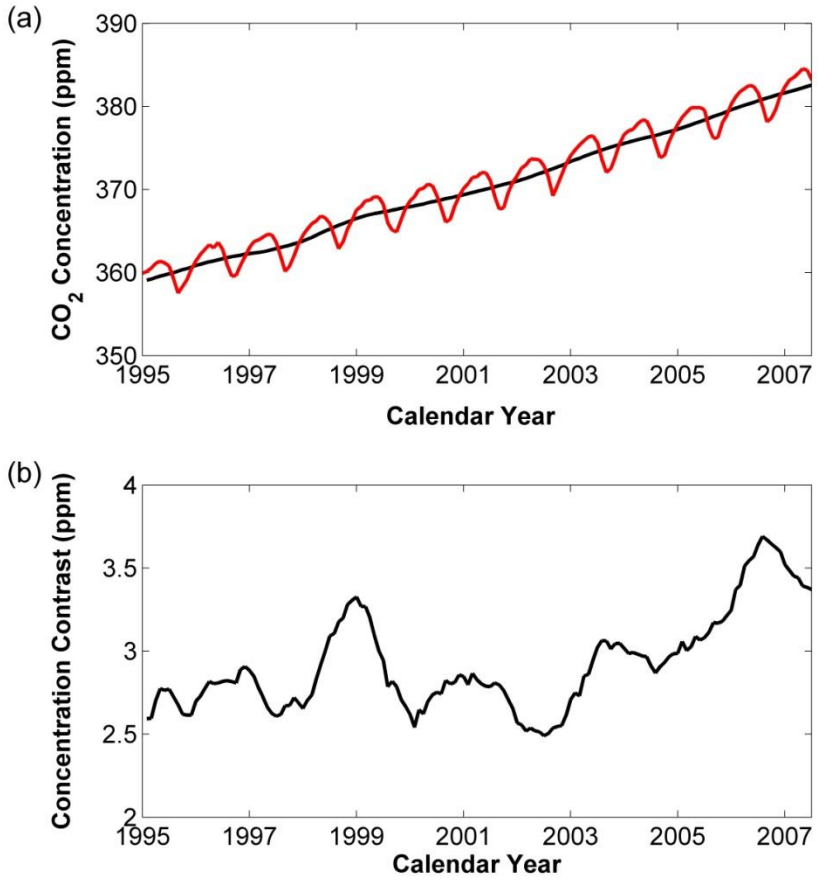

Figure 2.2 (a) Global atmospheric CO_2 concentration from 1995 to 2007, in ppm, derived by weighting monthly averages of station data in proportion to the surface area of the appropriate for the latitude zones to which the stations were assigned. The red line is with the seasonal cycle, the black line with the seasonal cycle removed. (b) Hemispheric CO_2 contrast (northern hemisphere CO_2 concentration minus southern hemisphere concentration) from 1995 to 2007, in ppm, reflecting the fact that fossil fuel combustion is largely concentrated in the northern hemisphere.

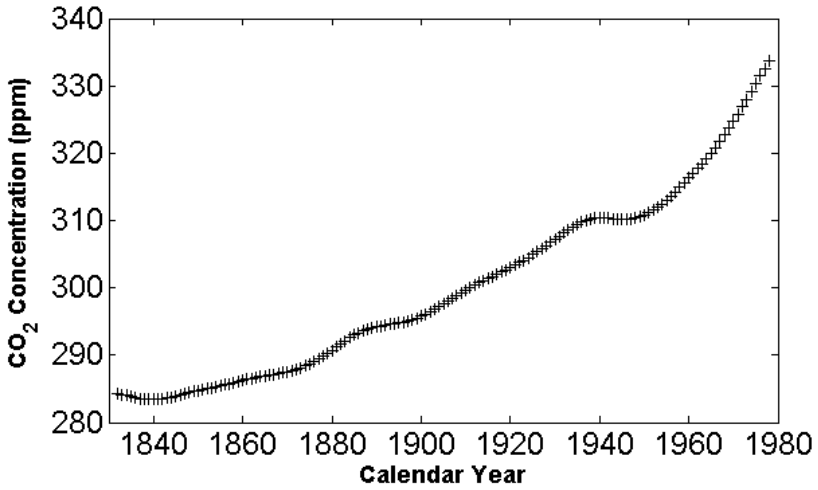

Figure 2.3 CO_2 concentration from DE08 and DE08-2 ice cores records smoothed using a spline fit with a 20 year cutoff.

Changes in the abundance of O_2 are expressed in terms of changes in the ratio of the concentration of O_2 relative to N_2. Expressed using the δ notation, the fractional difference in the O_2 content of a sample relative to the concentration in a reference gas is given by:

$$\delta(\frac{O_2}{N_2}) = \frac{(\frac{O_2}{N_2})_{sample}}{(\frac{O_2}{N_2})_{reference}} - 1 \qquad (2.2)$$

where δ (O_2/ N_2) denotes the ratio of the concentration of O_2 relative to N_2 in the sample and defines the ratio for the reference gas. Values of δ (O_2/ N_2) are quoted conventionally in units of per meg. One per meg equals 0.0001 percent. The observational CO_2 data used in this article are taken from the Scripps Institute of Oceanography O_2 program (http://scrippso2.ucsd.edu/osub2sub-data). The choice of stations is summarized in Table 2. The trend in global average δ (O_2/ N_2) was computed using the same procedure as was applied to

compute the averages for CO_2 displayed in Figure 2.2, and is presented in Figure 2.4a. As indicated, the abundance of O_2 relative to N_2 decreased by approximately 250 per meg between 1995 and 2007. Over the same period, as illustrated in Figure 2.2a, the concentration of globally averaged CO_2 increased by 25 ppm. The contrast in O_2/ N_2 between the northern and southern hemisphere is illustrated in Figure 2.4b. As expected, the abundance of O_2 in the northern hemisphere is lower than that in the southern hemisphere, reflecting the fact that fossil fuel combustion is largely concentrated in the northern hemisphere.

Table 2.2 Stations included in the global & hemispheric O_2 averaging process.

Station	**Latitude (^{o})**	**Longitude (^{o})**
Alert, NWT, Canada	82 ^{o}N	62 ^{o}W
Cold Bay, Alaska	55 ^{o}N	163 ^{o}W
Cape Kumukahi, Hawaii	20 ^{o}N	155 ^{o}W
La Jolla Pier, California	33 ^{o}N	117 ^{o}W
Mauna Loa Observatory, Hawaii	20 ^{o}N	156 ^{o}W
American Samoa	14 ^{o}S	170 ^{o}W
Cape Grim, Australia	41 ^{o}N	150 ^{o}W
Palmer Station, Antarctica	65 ^{o}S	64 ^{o}W
South Pole	90 ^{o}S	

Trends in emissions of CO_2 associated with combustion of fossil fuels and production of cement are presented in Figure 2.5: for the period 1995 – 2009 in Figure 2.5a and for the longer record extending back to 1750 in Figure 2.5b. CO_2 emission data are available from *Carbon Dioxide Information Analysis Center* (CDIAC) (http://cdiac.ornl.gov/trends/emis/meth_reg.html). Data for the recent period were derived using procedures developed by Marland and Rotty (1984)

(Marland et al. 1984) applied to energy statistics published by the United Nations (2010) (United Nations 2008) compiled on the basis of annual questionnaires distributed by the U.N. Statistical Office. Etemad et al. (1991) published a compilation of data on the production of coal, brown coal, peat and crude oil by nation and year back to 1751. Historical data on trade in fossil fuels were presented in a series of papers by Mitchell (1983, 1992, 1993, 1995). The results displayed in Figure 2.5b were computed using a combination of the data presented by Etemad et al. (1991) and Mitchell (1983, 1992, 1993, 1995). They indicate that approximately 350 billion tons of carbon have been released to the atmosphere from a combination of fossil fuel consumption and cement manufacture since 1751, amounting to half of the total since the mid 1970's.

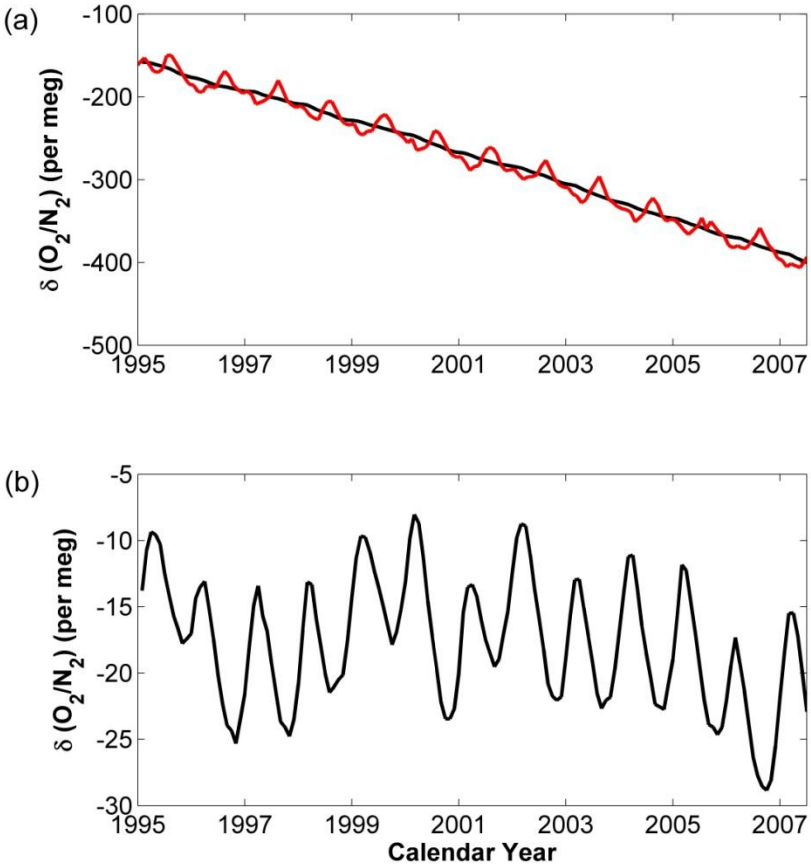

Figure 2.4 (a) Global atmospheric δ (O_2/ N_2) from 1995 to 2007, in per meg. The red line includes the seasonal cycle, the black line has the seasonal cycle removed. (b) Hemispheric O_2 contrast (northern hemisphere CO_2 concentration minus southern hemisphere concentration) from 1995 to 2007, in per meg, reflecting that fact that fossil fuel combustion is largely concentrated in the northern hemisphere.

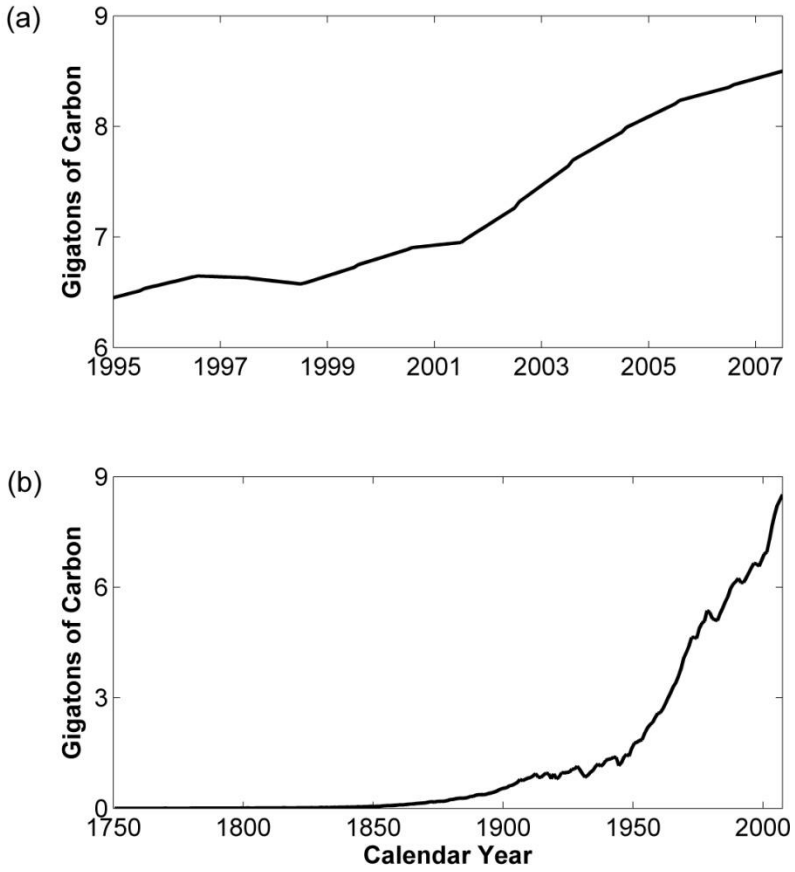

Figure 2.5 Carbon Dioxide Emissions from Fossil-Fuel Consumption and Cement Manufacture. One gigaton equals one billion metric tons. (a) period from 1995 to mid 2007. (b) period from 1750 to mid 2007.

2.3 Post-1995 global CO_2 budget

Given the mix and composition of the fossil fuels included in the contemporary global energy economy, it is estimated that 1.43 moles of O_2 are consumed for every mole of CO_2 released as a result of fuel combustion (Keeling 1988). Uptake (release) of carbon by the biosphere is estimated to be responsible for a source (sink) of 1.1 mole of O_2 for every mole of CO_2 involved in the atmosphere/biosphere exchange process (Severlnghaus 1995). The larger

value for the ratio of O_2 relative to CO_2 associated with fossil fuel combustion as compared to biospheric exchange reflects the influence of hydrogen rich components in the fuel mix. Combustion of CH_4 in natural gas is responsible, for example, for consumption of 2 moles of O_2 associated with production of every mole of CO_2. The slopes of the fossil fuel and biospheric segments of the CO_2 /O_2 trend curves discussed above are set by these considerations.

Results derived using the monthly averages of global concentrations for CO_2 and O_2 summarized in Figures 2.2 and 2.4 are presented in Figure 2.6. The data in Figure 2.6a indicate significant interannual variations in both ocean and biospheric uptake. A portion of this variability may be attributed to changes in the tropics associated for example with the ENSO phenomenon. A number of writers (Murray et al. 1994; Feely et al 1995; Chavez et al. 1999; Feely et al. 1999; Keeling et al. 2001) have pointed out that the reduction in upwelling in the tropical Pacific ocean during the warm (El Nino) phase serves to decrease what would normally be a source of CO_2 from the ocean in this region contributing therefore to a net increase in the overall global ocean sink for CO_2 (smaller source in the tropics, continuing sink at mid and higher latitudes implies a global increase in uptake). At the same time, there is evidence for a significant source of CO_2 from the biosphere in the tropics during the warm El Nino phase (Hashimoto et al. 2004; Zeng et al. 2005; Knorr et al. 2005). The region of intense rainfall shifts during this phase from the region near Indonesia to the middle of the Pacific. Subsequent drying out of vegetation in the previously moist region results in net release of CO_2, arising both as a consequence of natural processes but also, at least in some years, as the result of an increase in unsanctioned burning and clearance of land. A portion of the interannual variability may be attributed to the potential year-to-year changes in release and uptake of O_2 by the ocean discussed earlier (Keeling et al. 1993; Benter et al. 1996; Bender and Battle 1999). Ralph

Keeling notes that global warming may cause a decrease in the oceanic O_2 inventory with associated outgassing of O_2. The change in the oceanic inventory through the 1990s is estimated at $0.3 \pm 0.4\times10^{14}$ mol of O_2 per year (Keeling and Garcia 2001). The assumption of a source of O_2 from the ocean would result in an increase in the magnitude of the sink attributed to the biosphere in the present analysis. Conversely, if the ocean represents a sink for O_2, the sink attributed to the biosphere would be reduced accordingly.

The ambiguities introduced by short period fluctuations in biospheric and ocean exchange can be reduced by averaging data over multiple years. Results inferred for the cumulative uptakes of CO_2 by the ocean and biosphere post 1995 are presented in Figure 2.6b. Net uptake of CO_2 by the ocean and biosphere between 1995 and mid 2007 amounted to 25.7 and 13.1 Gt C respectively. Over the same period, fossil fuels added 89.3 Gt C to the atmosphere and the abundance in the atmosphere increased by 50.5 Gt C. Defining the airborne fraction as the fraction of net carbon added to the atmosphere that persists in the atmosphere, these results imply an airborne fraction of 56.5%. An alternate definition of the airborne fraction concept focuses exclusively on the fate of the fossil fuel source. The present results would imply that the increase in the abundance of CO_2 In the atmosphere between 1995 and 2007 was equivalent to 66.3 % of the fossil fuel source.

Uptake of CO_2 by the ocean is determined by the difference between the partial pressures of CO_2 in the air and in surface waters of the ocean. The abundance of CO_2 in the ocean is regulated by an equilibrium among the three primary forms of inorganic carbon dissolved in sea water, HCO_3^-, CO_3^{2-} and CO_2. Uptake of CO_2 may be described by the net reaction:

$$CO_2 + CO_3^{2-} \overset{H_2O}{\Leftrightarrow} 2HCO_3^- \qquad (2.3)$$

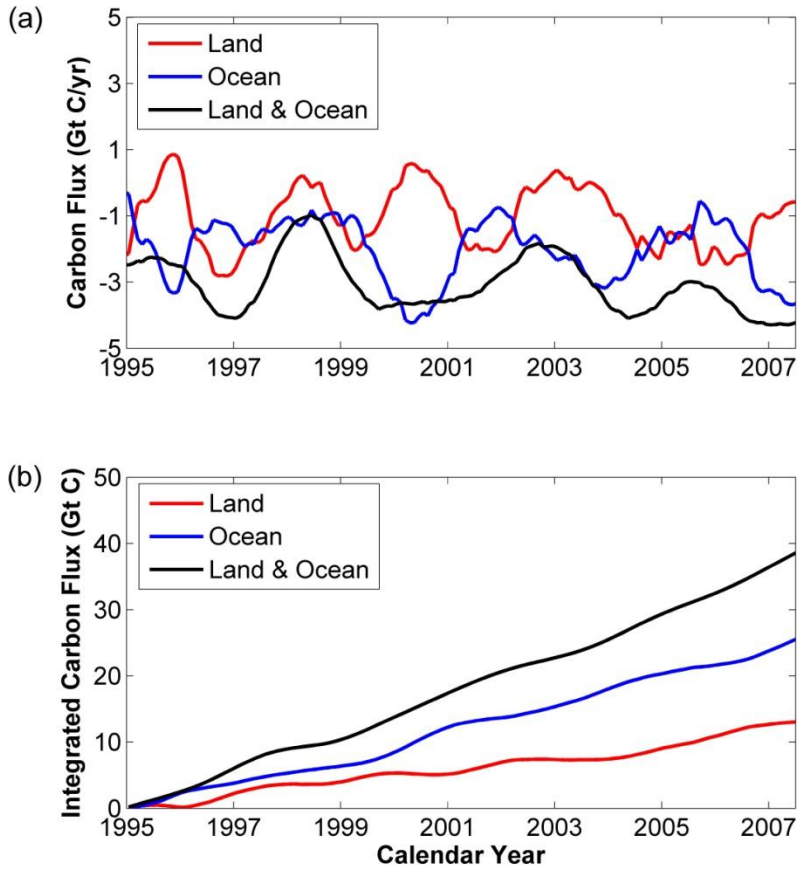

Figure 2.6 Terrestrial and oceanic carbon sink (or source) derived though analysis of global CO_2 concentrations and $\delta(O_2/N_2)$. (a) terrestrial and oceanic annual carbon flux, in Gt C/yr. Negative sign means that the carbon goes into the terrestrial or ocean from the atmosphere. (b) integrated terrestrial and oceanic carbon flux over time since 1995, in Gt C.

It follows that transfer of CO_2 from the atmosphere to the ocean is limited ultimately by the supply of CO_3^{2-} to the surface waters that are exposed to the atmosphere. A comprehensive discussion of ocean chemistry is presented in Broecker and Peng (1982). Following some algebraic manipulation, the airborne fraction may be defined in terms of the partial pressure of CO_2, $(P_{CO_2})_0$, in the atmosphere prior to disturbance (the pre-industrial reference), the value for the contemporary partial pressure of CO_2, P_{CO_2}, the initial abundance of carbonate ion $[CO_3^{2-}]_0$ in

upper-level ocean waters, the total abundance of CO_2 in the atmosphere prior to disturbance M_0, and the volume of ocean water V that has been in contact with the atmosphere over the intervening interval of time:

$$f_{atms} = [1 + \frac{(P_{CO_2})_0}{P_{CO_2}} [CO_3^{2-}]_0 \frac{V}{M_0}]^{-1} \quad (2.4)$$

Assuming a value of 280 ppm for the initial concentration of atmospheric CO_2 corresponding to a value of 5×10^{16} moles for M_0, with the concentration of CO_3^{2-} taken equal to 200×10^{-6} mol l^{-1}, it follows that if 10% of the ocean water had been exposed to the atmosphere over time since the industrial revolution (a reasonable assumption), the airborne fraction at the present time (P_{CO_2} = 390 ppm) would be equal to about 70%. The estimate quoted above for the airborne fraction appropriate for the 1995-2007 time interval, accounting both for the fossil fuel source and the biospheric sink, 66.3%, is consistent with an assumption that 12.8 % of ocean water has been exposed to the atmosphere since the industrial revolution. The airborne fraction is predicted to increase with time as sources of CO_3^{2-} available to neutralize CO_2 are depleted, a projection supported by analyses of the contemporary CO_2 budget (Le Quéré et al. 2009). Using a tracer technique proposed initially by Gruber et al. (1996) and Sabine et al. (2004) concluded that uptake by the ocean accounted for approximately 48% of the carbon added to the atmosphere as a result of fossil fuel combustion and cement manufacture over the period 1800 and 1994. This would imply an airborne fraction for the fossil fuel/cement source of 52% in reasonable agreement with expectation based on (4): the actual value for the airborne fraction should be adjusted to account for the cumulative contribution associated with exchange of carbon between the atmosphere and biosphere. The tracer technique suggests that the North Atlantic (representing only 15% of the total surface area of the ocean) accounts for 23% of the

anthropogenic carbon incorporated in the ocean. More than 40% of the total sink is identified with regions of the ocean between 30 ^{o}S and 50 ^{o}S. Approximately 60% of the total is incorporated in oceans of the Southern Hemisphere, in rough proportion to the surface area of the oceans in this hemisphere (Sabine et al. 2004).

2.4 Hemispheric Budgets

Exchange of air within hemispheres (north and south) proceeds significantly more rapidly than transfer between the hemispheres. This provides an important opportunity to exploit hemispheric average observations of the concentrations of CO_2 and O_2 to develop hemispheric budgets for CO_2. SF_6 is widely deployed as an electrical insulator in the modern world. The concentration of the gas in the atmosphere has increased by two orders of magnitude since 1970 (Levin et al. 2010). Its source is largely confined to the northern hemisphere and the extended lifetime of the gas in the atmosphere, estimated at as much as 3200 years (Ravishankara et al. 1993), establishes it as an ideal tracer for calibration of rates for inter-hemispheric exchange (Lovelock 1971; Maiss and Levin 1994).

The rate of change of the average concentrations for SF_6 in the northern and southern hemispheres may be described by the following equations:

$$dC_{SH}(t)/dt = (C_{NH}(t) - C_{SH}(t))/\tau_{ex} \tag{2.5}$$

$$dC_{NH}(t)/dt = S(t) - (C_{NH}(t) - C_{SH}(t))/\tau_{ex}$$

where $C_{SH}(t)$ and $C_{NH}(t)$ denote the abundances of the gas in the northern and southern hemispheres respectively, τ_{ex} defines the rate at which air is exchanged between the hemispheres (assumed to be proportional to the difference in hemispheric concentrations) , and S denotes the

magnitude of the source (assumed to be confined to the northern hemisphere). Extensive measurements of atmospheric SF_6 are available since 1995 from the Halocarbon and other Atmospheric Trace Species (HATS) program at NOAA. Measurements from flask samples began in 1995, focusing initially on 8 stations, extended later to include sampling from 12 remote locations. Data from the flask program have been complemented more recently with in situ measurements from gas chromatographic instrumentation installed at six field stations. The gas chromatographic measurements provide an hourly record of changes in the concentrations of SF_6 at these stations. Hemispheric average concentrations of SF_6 were computed on the basis of the NOAA measurements following the procedures described earlier to calculate hemispheric average concentrations for CO_2 and O_2. Data for this analysis were taken from the Earth System Research Laboratory compilation (http://www.esrl.noaa.gov/gmd/hats/combined/SF6.html). Details of the data source are described in Elkins and Dutton (2009) and Rigby et al. (2010). Using trends in $C_{NH}(t)$ and $C_{SH}(t)$ derived from the observational data, equation (2.5) can be employed to calculate temporal variations both in S and in τ_{ex}. Observed changes in the average north-south concentration contrasts, together with results inferred for the changes in S and τ_{ex} with time, are presented in Figure 2.7. Over the period from 1995 to mid 2007, the average global annual source of SF_6 is estimated at 5.81 Gg, and the average exchange time is equal to 1.2 yr.

Hemispheric budgets for CO_2 computed using results for τ_{ex} derived from the SF_6 analysis are displayed for the northern and southern hemispheres in Figures 2.8 and 2.9 respectively. Trends in biospheric and ocean uptake as a function of time are summarized in Figures 2.8a and 2.9a with results for cumulative uptake displayed in Figures 2.8b and 2.9b. The results presented here indicate significant contributions from both the biosphere and ocean to the net sink for CO_2

in the northern hemisphere. Uptake by the ocean is important in both hemispheres with the contribution from the southern hemisphere exceeding that from the northern hemisphere by about 50% (a cumulative total of 15 Gt C in the former case as compared to 9 Gt C in the latter). The inference that the sink associated with the biosphere is located primarily in the northern hemisphere is consistent with conclusions reached earlier by Keeling et al. (1996) and by Fan et al. (1998). Fan et al. (1998) suggested that removal of atmospheric CO_2 by the biosphere was concentrated mainly in mid-latitude regions of Eurasia and North America, averaging approximately 2 Gt C yr^{-1} between 1981 and 1987 with a somewhat higher rate inferred for removal between 1988 and 1992.

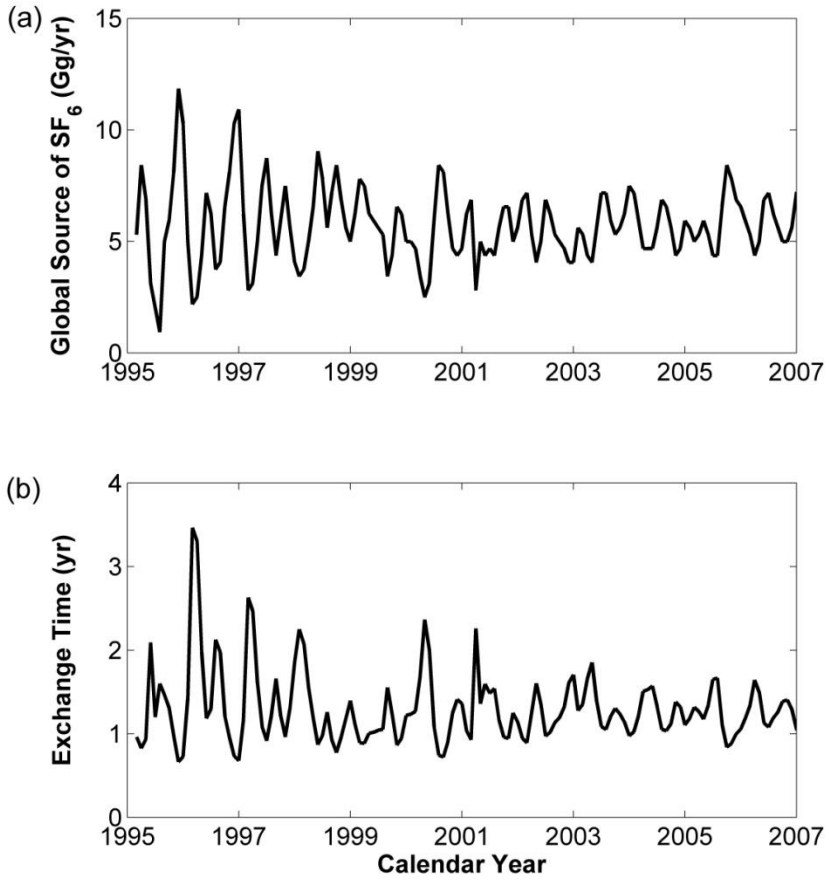

Figure 2.7 (a) Global source of SF_6 calculated using equation (2.5). (b) Exchange time calculated with equation (2.5), assuming that SF_6 is well mixed within each hemisphere.

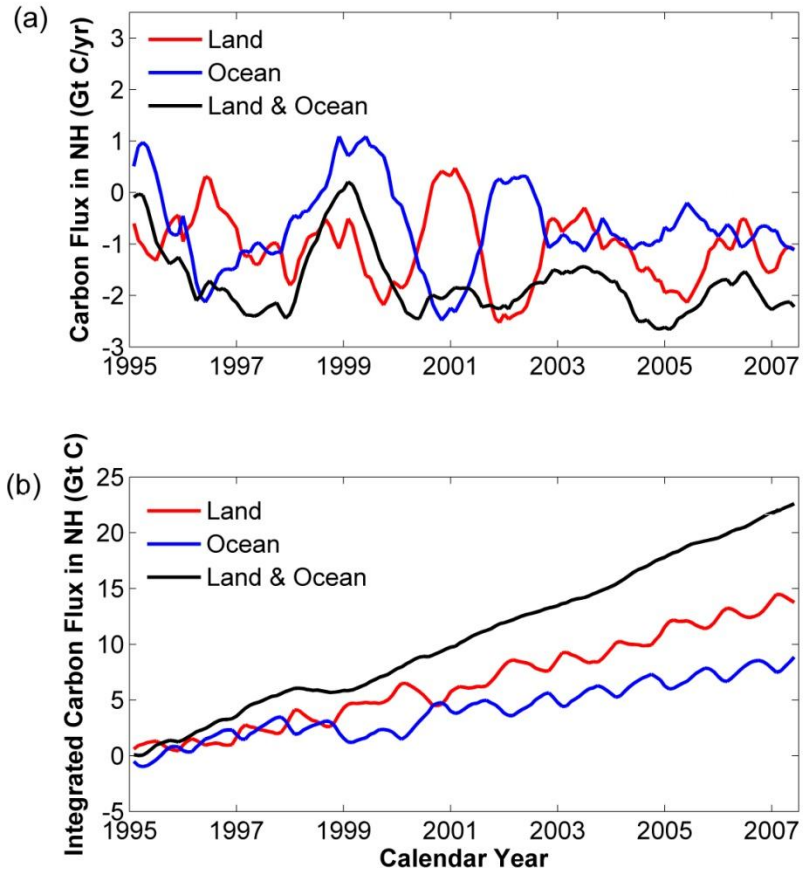

Figure 2.8 Same as Figure 2.6, but for the northern hemisphere.

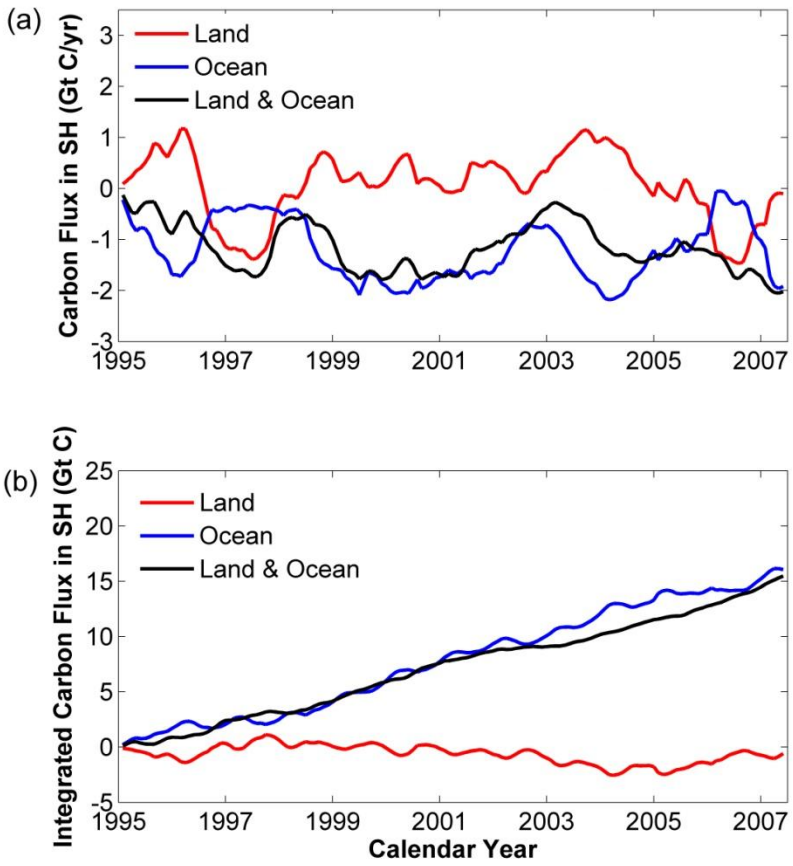

Figure 2.9 Same as Figure 2.6, but for the southern hemisphere.

The results in Figure 2.8b imply an average rate for removal by the northern hemispheric biosphere as a whole of about 1.3 Gt C yr^{-1}. It is possible that the composite sink inferred here could reflect the combination of a mid-latitude sink offset to some extent by a source at higher latitudes. A study of the carbon balance of a mature black spruce forest in Central Canada by Goulden et al. (1998) indicated a small though significant net source of CO_2 from soils in this ecosystem over the period 1994-1996. Soils at high latitude represent an important reservoir for organic carbon, estimated to include as much as 500 Gt C (Post et al. 1982). Release of carbon from this environment triggered by regional warming could be responsible for a significant

present, and potentially even more important future, source not only of CO_2 but also of CH_4 (Davidson et al. 2006; Schuur et al. 2008).

2.5 Longer term trends

Keeling et al. (1995) presented an analysis of the CO_2 record from1958 to 1995 in which the data were interpreted initially in terms of a constant airborne fraction of 55.9% with an assumption that fossil fuel combustion and cement manufacture were responsible for the dominant source of CO_2. This simple procedure resulted in a remarkably accurate representation of the data record over the entire time interval. They proceeded to focus on an interpretation of the departures of the data from the reference fit, attributing these anomalies primarily to fluctuations in the rate of exchange of carbon between the atmosphere and biosphere. A similar approach is adopted here to a study of the longer-term record of CO_2 dating back to 1830.

A summary of prior analyses of the historical CO_2 budget is presented in Table 3. Separate entries in the Table refer to the time periods 1800-1994 and 1850-2000. The data for 1800-1994 imply an overall value for the average airborne fraction of 0.583, with 0.556 for the interval 1850-2000. As indicated earlier, we expect the value of the airborne fraction to increase with time as the supply of CO_3^{2-} to surface waters is depleted. Our analysis of the budget from 1995 to 2007 indicated an airborne fraction of 0.663. Given the inevitable uncertainty in the appropriate value for the airborne fraction and the expectation that it may have varied significantly over time, we elect for present purposes to consider a range of values, from a low of 0.56 to a high of 0.66.

Table 2.3 A summary of prior analyses of the historical CO_2 budget.

	1800 to 1994	1850 to 2000
Emission from fossil fuels and cement production	244 ± 20 Gt C [a]	275 Gt C [c]
Atmospheric increase	165 ± 4 Gt C [a]	175 Gt C [d]
Oceanic uptake	118 ± 19 Gt C [a]	140 Gt C [e]
Net terrestrial source	-39 ± 28 Gt C [a]	-40 Gt C
Land-use change (source)	-174 Gt C [b]	-156 Gt C [b]
Residual terrestrial sink	135 Gt C	116 Gt C
Air-Borne Fraction	0.583	0.556

a: Sabine et al. 2004

b: Houghton 2003

c: Keeling 1973; Andres et al. 1999

d: Prentice et al. 2011

e: Joos et al. 1999

Following Keeling et al. (1995), we assume that the dominant contributions to the rise in CO_2 over the past century and a half can be attributed to the combination of fossil fuel combustion and cement manufacture. With this assumption, the historical record for CO_2 is fitted adopting a constant value for the airborne fraction, either 0.56 or 0.66. Departures from the fits are interpreted as indications of the contributions to the observed trend attributable to exchange with the biosphere. Results are presented in Figure 2.10. The analysis suggests that the biosphere was responsible for a net source of CO_2 from 1840 to about 1940. This conclusion appears to be relatively independent of the choice of airborne fraction. Assuming an airborne fraction of 0.56,

the biospheric source, integrated from 1840 to 1940 is estimated at about 55 Gt C corresponding to an annual source of about 0.55 Gt C yr^{-1}. The rise in CO_2 is dominated by the fossil fuel – cement source only for the period subsequent to about 1900. After 1940, the biosphere switches from a net source to a net sink. The imputed biospheric source, as would be expected, is slightly less if we assume a larger value for the airborne fraction. With an airborne fraction of 0.66, the transition from biosphere dominated source to fossil fuel-cement dominated source also occurs in about 1900. The integrated biospheric source from 1840 to 1940 is estimated at 44 Gt C.

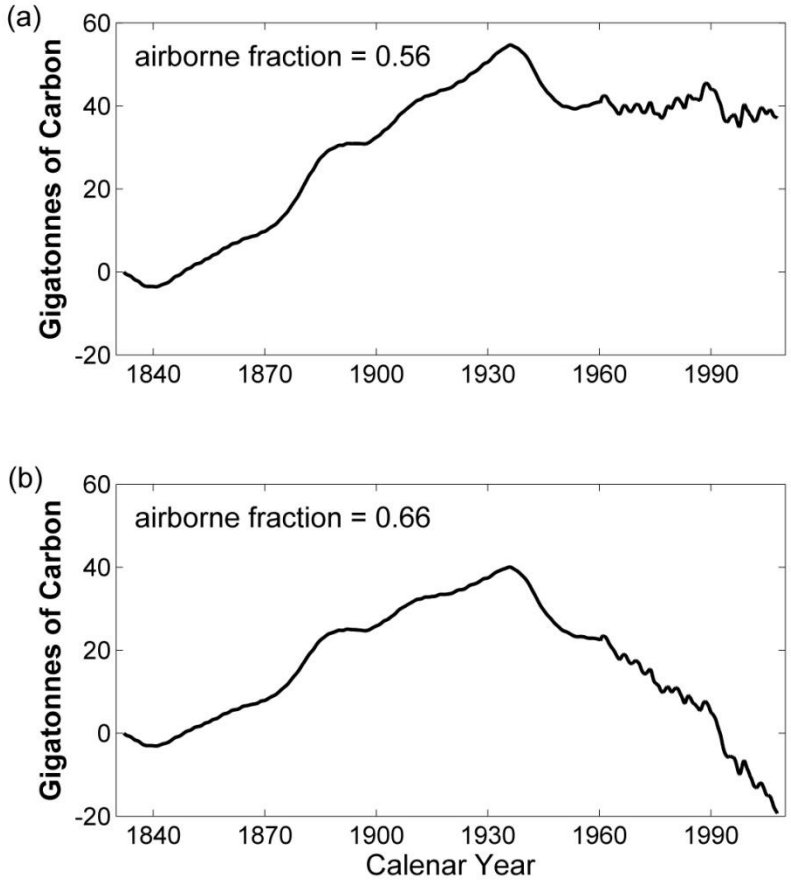

Figure 2.10 Cumulative terrestrial carbon fluxes: (a) assumes an airborne fraction of 0.56; (b) airborne fraction equal to 0.66.

2.6 Concluding remarks

The contemporary increase in the concentration of CO_2 in the atmosphere is due mainly to emissions associated with combustion of fossil fuels. Since 1995, approximately 57% of the carbon released as a result of the fossil fuel source has persisted in the atmosphere, 29% has been transferred to the ocean, and the balance, 15%, has been absorbed by the biosphere. It is clearly important to define the nature of the biospheric sink and indeed its location. Evidence suggests that it is concentrated primarily at mid-latitudes of the northern hemisphere. Possible explanations include a climate induced extension of the growing season, enhanced uptake by photosynthesis prompted by the increasing level of CO_2 in the atmosphere, and, potentially, regrowth of vegetation representing return to conditions prevalent prior to the mid 20^{th} century when the biosphere is estimated to have provided a net source rather than a net sink for CO_2 (regrowth of forests depleted previously in conjunction with conversion of land for purposes of agriculture). Compounding the challenge is the likelihood that soils at high latitude may be responsible for a net source of CO_2 and that there may be additional release associated with deforestation in the tropics (in countries such as Brazil and Indonesia), the latter representing a repeat of what happened earlier in the mid-latitude regime. Natural forests are important as a source of environmental services. The sad fact is that eliminating these systems and converting them to either pasture or agriculture can provide a more immediate return to those who own or control the land. Current economic accounting fails regrettably to recognize the intrinsic value of the environmental services provided by these natural ecosystems.

If we are to avoid unacceptable future disruption to the global climate system, it will be necessary to constrain future growth in the concentration of the key greenhouse gases, not only CO_2 but also CH_4 and N_2O. Reduction in emissions of CO_2 from fossil fuels can make an

important contribution to this objective but will require a major shift from the current fossil fuel dominated energy economy to one emphasizing low or zero carbon energy alternatives. It will be critical also in meeting our objective to preserve a supportive global climate system to develop an improved understanding of the complex functions of the global biosphere, its role not only in regulating the concentrations of the key greenhouse gases in the atmosphere but also the contribution it makes to maintaining an accommodating hydrological cycle. We have learned a great deal about the function of the carbon cycle over the past 50 years, due in no small measure to the contributions of Charles David and Ralph Keeling and their colleagues. The present paper is offered as a status report on where we are: it is clear though that there is more work to be done.

Acknowledgements

The work described here was supported by the National Science Foundation under grant ATM-1019134 to Harvard University.

References

Andres, R. J., D. J. Fielding, G. Marland, T. A. Boden, N. Kumar, and A. T. Kearney, 1999: Carbon dioxide emissions from fossil-fuel use, 1751–1950. *Tellus B*, **51**, 759-765.

Battle, M., M. L. Bender, P. P. Tans, J. W. C. White, J. T. Ellis, T. Conway and R. J. Francey, 2000: Global carbon sinks and their variability inferred from atmospheric O2 and δ13C. *Science*, **287**, 2467-2470.

Bender, M., T. Ellis, P. Tans, R. Francey, and D. Lowe 1996: Variability in the O_2/N_2 ratio of southern hemisphere air, 1991–1994: Implications for the carbon cycle. *Global Biogeochem. Cycles*, **10**, 9-21.

Bender, M. L., and M. O. Battle, 1999: Carbon cycle studies based on the distribution of O_2 in air. *Tellus B*, **51**, 165-169.

Broecker, W. S., and T. H.Peng, 1982: Tracers in the Sea. Palisades, N.Y.: Eldigio Press.

Chavez, F. P., and P. G. Strutton, G. E. Friederich, R. A. Feely, G. C. Feldman, D. G. Foley, and M. J. McPhaden, 1999: Biological and chemical response of the equatorial Pacific Ocean to the 1997-98 El Niño. *Science*, **286**, 2126-2131.

Ciais, P., P. P. Tans, M. Trolier, J. W. C. White and R. J. Francey, 1995: A large northern hemisphere terrestrial CO_2 sink indicated by the $^{13}C/^{12}C$ ratio of atmospheric CO_2. SCIENCE-NEW YORK THEN WASHINGTON, 1098-1098.

Davidson, E. A., and I. A. Janssens, 2006: Temperature sensitivity of soil carbon decomposition and feedbacks to climate change. *Nature*, **440**, 165-173.

Elkins, J. W., and G. S. Dutton, 2009: Nitrous oxide and sulfur hexafluoride. *Bull. Am. Meteorol. Soc.*, **90**, S38-S39.

Etemad, B., J. Luciani, P. Bairoch, and J. C. Toutain, 1991: World Energy Production 1800-1985. Librarie DROZ, Switzerland.

Etheridge, D. M., L. P. Steele, R. L. Langenfelds, R. J. Francey, J. M. Barnola, and V. I. Morgan, 1996: Natural and anthropogenic changes in atmospheric CO_2 over the last 1000 years from air in Antarctic ice and firn. *J. Geophys. Res.: Atmos.*, **101**, 4115-4128.

Fan, S., M. Gloor, J. Mahlman, S. Pacala, J. Sarmiento, T. Takahashi, and P. Tans, 1998: A large terrestrial carbon sink in North America implied by atmospheric and oceanic carbon dioxide data and models. *Science,* **282**, 442-446.

Feely, R. A., R. Wanninkhof, C. E. Cosca, P. P. Murphy, M. F. Lamb, and M. D. Steckley, 1995: CO_2 distributions in the equatorial Pacific during the 1991–1992 ENSO event. *Deep Sea Res., Part II*, **42**, 365-386.

Feely, R. A., R. Wanninkhof, T. Takahashi, and P. Tans, 1999: Influence of El Nino on the equatorial Pacific contribution to atmospheric CO_2 accumulation. *Nature*, **398**, 597-601.

Friedli, H., H. Lötscher, H. Oeschger, U. Siegenthaler and B. Stauffer, 1986: Ice core record of the $^{13}C/^{12}C$ ratio of atmospheric CO_2 in the past two centuries. *Nature,* **324**, 237-238.

Goulden, M. L., S. C. Wofsy, J. W. Harden, S. E. Trumbore, P. M. Crill, S. T. Gower, and J. W. Munger, 1998: Sensitivity of boreal forest carbon balance to soil thaw. *Science*, **279**, 214-217.

Gruber, N., J. L. Sarmiento, and T. F. Stocker, 1996: An improved method for detecting anthropogenic CO_2 in the oceans. *Global Biogeochem. Cycles*, **10**, 809-837.

Hashimoto, H., R. R. Nemani, M. A. White, W. M. Jolly, S. C. Piper, C. D. Keeling, and S. W. Running, 2004: El Niño–Southern Oscillation–induced variability in terrestrial carbon cycling. *J. Geophys. Res.: Atmos.*, **109**.

Houghton, R. A., 2003: Revised estimates of the annual net flux of carbon to the atmosphere from changes in land use and land management 1850–2000. *Tellus B*, **55**, 378-390.

Joos, F., R. Meyer, M. Bruno and M. Leuenberger, 1999: The variability in the carbon sinks as reconstructed for the last 1000 years. *Geophys. Res. Lett.*, **26**, 1437-1440.

Keeling, C. D., 1973: Industrial production of carbon dioxide from fossil fuels and limestone. *Tellus*, **25**, 174-198.

Keeling, C. D., T. P. Whorf, M. Wahlen, and J. V. D. Plicht, 1995: Interannual extremes in the rate of rise of atmospheric carbon dioxide since 1980. *Nature*, **375**, 666-670.

Keeling, C. D., S. C. Piper, R. B. Bacastow, M. Wahlen, T. P. Whorf, M. Heimann and H. A. Meijer, 2001: SIO Reference Series, No. 01-06, Scripps Institution of Oceanography, San Diego, 88 pp.

Keeling, R. F., 1988: thesis, Harvard Univ.

Keeling, R. F., and H. E. Garcia, 2002: The change in oceanic O_2 inventory associated with recent global warming. *Proc. Natl. Acad. Sci. U. S. A.*, **99**, 7848-7853.

Keeling, R. F., R. P. Najjar, M. L. Bender, and P. P. Tans, 1993: What atmospheric oxygen measurements can tell us about the global carbon cycle. *Global Biogeochem. Cycles*, **7**, 37-67.

Keeling, R. F., S. C. Piper and M. Heimann, 1996: Global and hemispheric CO2 sinks deduced from changes in atmospheric O_2 concentration. *Nature*, **381**, 218-21.

Knorr, W., M. Scholze, N. Gobron, B. Pinty, and T. Kaminski, 2005: Global scale drought caused atmospheric CO_2 increase. *Trans., Am. Geophys. Union*, **86**, 178-181.

Le Quéré, C., M. R. Raupach, J. G. Canadell, G. Marland, L. Bopp, P. Ciais, and F. I. Woodward, 2009: Trends in the sources and sinks of carbon dioxide. *Nat. Geosci.*, **2**, 831-836.

Levin, I., T. Naegler, R. Heinz, D. Osusko, E. Cuevas, A. Engel, and S. A. Zimov, 2010: The global SF_6 source inferred from long-term high precision atmospheric measurements and its comparison with emission inventories. *Atmos. Chem. Phys.*, **10**, 2655-2662.

Lovelock, J. E., 1971: Atmospheric fluorine compounds as indicators of air movements. *Nature*, **230**, 379.

Maiss, M., and I. Levin, 1994: Global increase of SF_6 observed in the atmosphere. *Geophys. Res. Lett.*, **21**, 569-572.

Marland, G., and R. M. Rotty, 1984: Carbon dioxide emissions from fossil fuels: A procedure for estimation and results for 1950–1982. *Tellus B*, **36**, 232-261.

Mitchell, B. R., 1983: *International Historical Statistics: The Americas and Australasia 1750-1988*. Gale Research Company, Detroit, United States, 522-525.

Mitchell, B. R., 1992: *International Historical Statistics: Europe 1750-1988*. Stockton Press, New York, United States, 465-485.

Mitchell, B. R., 1993: *International Historical Statistics: The Americas 1750-1988*. Stockton Press, New York, United States, 405-414.

Mitchell, B. R., 1995: *International Historical Statistics: Africa, Asia and Oceania 1750-1988*. Stockton Press, New York, United States, 490-497.

Murray, J. W., R. T. Barber, M. R. Roman, M. P. Bacon, and R. A. Feely, 1994: Physical and biological controls on carbon cycling in the equatorial Pacific. *Science*, **266**, 58-65.

Post, W. M., W. R. Emanuel, P. J. Zinke, and A. G. Stangenberger, 1982: Soil carbon pools and world life zones. *Nature*, **298**, 156 - 159.

Prentice, I.C., and et al., 2001: *Climate Change 2001: The Scientific Basis. Contribution of Working Group I to the Third Assessment Report of the Intergovernmental Panel on Climate Change*. Cambridge, UK/New York: Cambridge Univ. Press., 239-287.

Ravishankara, A. R., S. Solomon, A. A. Turnipseed, and R. F. Warren, 1993: Atmospheric lifetimes of long-lived halogenated species. *Science*, **259**, 194-199.

Rigby, M., J. Mühle, B. R. Miller, R. G. Prinn, P. B. Krummel, L. P. Steele, and J. W. Elkins, 2010: History of atmospheric SF_6 from 1973 to 2008. *Atmos. Chem. Phys.*, **10**, 10305-10320.

Sabine, C. L., R. A. Feely, N. Gruber, R. M. Key, K. Lee, J. L. Bullister, and A. F. Rios, 2004: The oceanic sink for anthropogenic CO_2. *science*, **305**, 367-371.

Schuur, E. A., J. Bockheim, J. G. Canadell, E. Euskirchen, C. B. Field, S. V. Goryachkin, and S. A. Zimov, 2008: Vulnerability of permafrost carbon to climate change: Implications for the global carbon cycle. *BioScience*, **58**, 701-714.

Severlnghaus, J. P., 1995: thesis, Columbia Univ.

United Nations, 2010: *2008 Energy Statistics Yearbook*. United Nations Department for Economic and Social Information and Policy Analysis, Statistics Division, New York.

Zeng, N., A. Mariotti, and P. Wetzel, 2005: Terrestrial mechanisms of interannual CO_2 variability. *Global Biogeochem. Cycles*, **19**.

Chapter 3

Meteorologically defined limits to reduction in the variability of outputs from a coupled wind farm system in the Central US

[Huang, J., X. Lu, and M. B. McElroy, M. B., 2014: Meteorologically defined limits to reduction in the variability of outputs from a coupled wind farm system in the Central US. *Renewable Energy*, **62**, 331-340.]

Abstract

Studies suggest that onshore wind resources in the contiguous US could readily accommodate present and anticipated future US demand for electricity. The problem with the output from a single wind farm located in any particular region is that it is variable on time scales ranging from minutes to days posing difficulties for incorporating relevant outputs into an integrated power system. The high frequency (shorter than once per day) variability of contributions from individual wind farms is determined mainly by locally generated small scale boundary layer. The low frequency variability (longer than once per day) is associated with the passage of transient waves in the atmosphere with a characteristic time scale of several days. Using 5 years of assimilated wind data, we show that the high frequency variability of wind-generated power can be significantly reduced by coupling outputs from 5-10 wind farms distributed uniformly over a ten state region of the Central US in this study. More than 95% of

the remaining variability of the coupled system is concentrated at time scales longer than a day, allowing operators to take advantage of multi-day weather forecasts in scheduling projected contributions from wind.

3.1 Introduction

Some 13,131 MW of wind generating capacity were added to the US electrical system in 2012, an increase of 93% compared with the same period in 2011. Total installed capacity for wind power in the U.S. amounted to 60,007 MW by the end of 2012, equal to approximately 6% of total U.S. power generating capacity. Lu et al. (2009) argued that an onshore network of GE 2.5 MW turbines installed in the contiguous U.S. could supply as much as 16 times total current U.S. demand for electricity. A study by the U.S. Department of Energy concluded that wind could account economically for 20% of total U.S. demand for electricity by 2030 (Lindenberg 2009), while Short et al. (2003) argued that as much as 25% of demand could be met feasibly by 2050.

The current electrical system requires an essentially instantaneous balance of supply and demand dictated largely by the latter. Opportunities for storage of electricity when supply exceeds demand are limited, while options to modulate demand are also minimal. Base load demand is accommodated in the present system mainly by a combination of contributions from nuclear and coal with an additional contribution in some regions of the country from hydro. Gas-fired systems provide the fast response required to adjust to short and intermediate-term fluctuations in demand. The challenge posed by the need to incorporate a significant source from wind relates to the intrinsic variability of this source. Production of electricity from an individual

wind farm can vary over a wide range on time scales as brief as minutes or as extensive as days or even longer (Masters 2004).

A number of authors have pointed to the advantages that could be realized by combining outputs from a series of spatially separated wind farms (Kahn 1979; Simonsen and Stevens 2004; Czisch and Ernst 2001; Oswald 2008; Holttinen et al. 2005; Katzenstein et al. 2010; Kempton et al. 2010; Archer and Jacobson 2007; Hart and Jacobson 2011; Fertig et al. 2012). Katzenstein et al. (2010) reported a frequency dependent analysis of the smoothing in output that could be obtained by coupling up to 20 spatially separated wind farms in Texas. Linking up as few as 4 of these farms resulted in a reduction of 87% in the variance of hourly output as compared to that associated with a single installation. Adding the remaining 16 facilities resulted in only a minimal reduction in the overall variance (8%). Kempton et al. (2010), using 5 years of wind data from 11 meteorological stations distributed over 2500 km of the US East Coast, concluded that when outputs from an array of wind farms distributed along the coast were coupled, the output from the interconnected system was much more stable than that from any individual location. The correlation between individual station outputs decreased exponentially on a scale of 430 km as determined by properties of the related synoptic weather systems. Archer and Jacobson (2007) considered the benefits of connecting wind farms from up to 19 sites in the mid west characterized by annually averaged wind speeds in excess of 6.9 m s^{-1} (class 3 or greater) at 80 m. They concluded that on average 30%, as much as 47%, of the connected output could be deployed as reliable base-load power. Hart and Jacobson (2011) found that combining complementary renewable resources, such as wind, solar and hydro, can help mitigate the variability problems associated with any one of these options. Fertig et al. (2012) reported that interconnecting wind plants on a large scale would reduce the most extreme hour-to-hour

changes in energy output and increase the percentage of reliable power. Previous studies exploring the issue of interconnections focused on the statistical analysis of wind data and did not explicitly address the physical factors responsible for the observed variation of surface winds.

This study addresses the issue of interconnection with specific attention to the physical factors that determine the temporal variability of winds in the near surface region of the atmosphere. Surface winds are influenced by the passage of transient waves and by boundary layer turbulence triggered by these waves (Holton and Hakim 2012; Wallace and Hobbs 2006; James 1995). An understanding of these physical factors can help interpret the findings of the previous studies. We consider specifically how transient waves influence instantaneous power output. We show that there is a limit to the extent that the intrinsic variability of power output can be reduced, and quantify how this reduction in variability responds to different levels of wind farm coupling.

3.2 Materials and methods

This study was based on meteorological data from the Modern Era Retrospective-analysis for Research and Applications (MERRA) compilation covering the period Dec 2002 to Nov 2007. Boundary layer winds and geopotential heights included in this compilation were obtained on the basis of retrospective analysis of global meteorological data using Version 5.2.0 of the GEOS-5 DAS. Geopotential heights are available on a 3-hour basis with a resolution of 5/4 ^{o} latitude by 5/4 ^{o} longitude, while boundary layer winds are calculated hourly at a resolution of 1/2 ^{o} latitude by 2/3 ^{o} longitude. Data on surface roughness are also included in the dataset. The MERRA assimilation was adopted in the present analysis to take advantage of the relatively high spatial and temporal resolution available with this product.

In calculating the potential electricity generated from wind, we chose to use power curves and technical parameters for the GE 2.5 MW turbines (rated wind speed 12.0 m/s, cut-in wind speed 3.5 m/s, and cut-out speed 25.0 m/s). The power curve of the wind turbine, provided by the manufacturer, available at http://www.ge-energy.com and displayed in Figure 3.1, defines the variation of power output as a function of wind speed. The usefulness of adopting the GE 2.5 MW power curve in analyzing wind power has been tested and justified elsewhere (Lu et al. 2011).

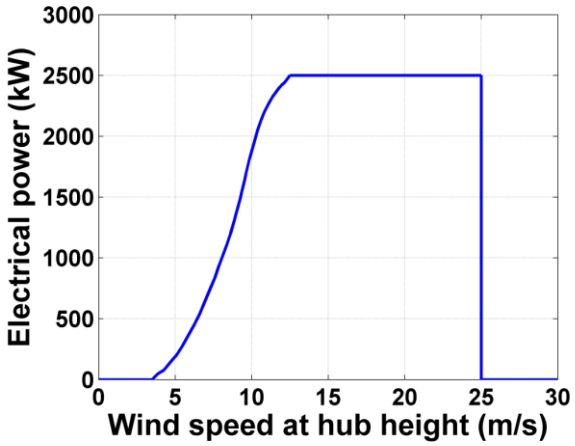

Figure 3.1 GE 2.5 MW wind turbine power curve.

Boundary layer wind data are available on an hourly basis for altitudes of 2 m, 10 m, and 50 m. We chose to extrapolate the results from 50 m to estimate the wind speed at 100 m as appropriate for the hub height of the GE 2.5 MW turbines. The extrapolation was implemented using the logarithmic relationship appropriate for a neutral stability condition assuming a surface roughness of Z_0:

$$V_{100} = V_{50} \times \frac{ln(Z/Z_0)}{ln(Z_{50}/Z_0)} \tag{3.1}$$

where V_{100} and V_{50} indicate hourly values for the wind speed at 100 m and 50 m respectively, Z

and Z_{50} define the elevation of the turbine hub (100 m) and the reference 50 m altitude, and Z_0 defines the surface roughness length, values for which are taken from the MERRA tabulation.

The power yield at any given time is expressed as a fraction of the rated power potential of the installed turbines. This quantity, the instantaneous capacity factor (CF), is given by

$$CF = \frac{P_{real}}{P_{rated}} \tag{3.2}$$

where P_{real} denotes the power actually realized, and P_{rated} refers to the power that could have been realized had conditions permitted the turbine to operate at its name plate capacity. The instantaneous capacity factors presented here are calculated as functions of time on an hourly basis.

The earlier analyses (Archer and Jacobson 2007, Fertig et al. 2012) are extended to explore the advantages that could be realized by coupling an array of wind farms over the wind-rich Central Plains region of the US. For present purposes we identify the region of interest as the combined states of Montana, Wyoming, North Dakota, South Dakota, Minnesota, Wisconsin, Iowa, Illinois, Missouri, Nebraska, Kansas, Oklahoma, and Texas. To illustrate the influence of transient waves and the benefit of interconnection, we select ten farms, one per state, distributed over the study region as indicated in Figure 3.2. Though these wind farms are located in three different electrical interconnections (Western Interconnection, Eastern Interconnection, and ECORT*)*, it is assumed in this study that all of the wind farms located within the Central Plains region could be coupled.

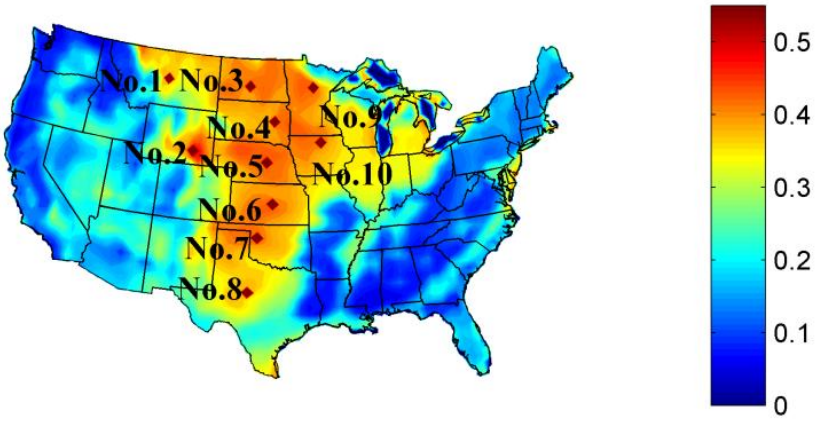

Figure 3.2 Color coded values for capacity factor (CF) as a function of position averaged over the 5 year period Dec 1 2002 to Nov 30 2007. Positions of individual locations considered in this chapter are indicated by the dots, one per state.

3.3 Examination of transient waves

The boundary layer wind, e.g. 100 m wind, as indicated earlier, is controlled by two factors: conditions in the free atmosphere which vary on a time scale of a few days with a spatial scale of about 1000 km, and conditions at the surface which are responsible for small scale and fast varying turbulence in the boundary layer (Holton and Hakim 2012; Wallace and Hobbs 2006). Figure 3.3a shows the variation of the vertical profile of the flux of kinetic energy per square meter, $1/2\ \rho \bullet V^3$ (ρ represents the density of air at different layers of the atmosphere, and V denotes the wind speed) in the free atmosphere between 870 hPa (approximately 1.5 km above sea level) to 500 hPa (approximately 5.5 km above sea level) above a grid cell near the City of Chicago (42 ^{o}N, 88.7 ^{o}W) between Dec 1 2004 and Feb 28 2005. Figure 3.3b presents the variation of CF that would be realized for a wind farm located in the vicinity of Chicago (42 ^{o}N, 88.7 ^{o}W) over the same period. While strong winds in the free atmosphere generally lead to strong winds near the surface, and consequently high instantaneous values of CF, conditions at

the surface, as indicated, introduce random turbulent fluctuations that contribute significantly to the high frequency variability of the boundary layer wind.

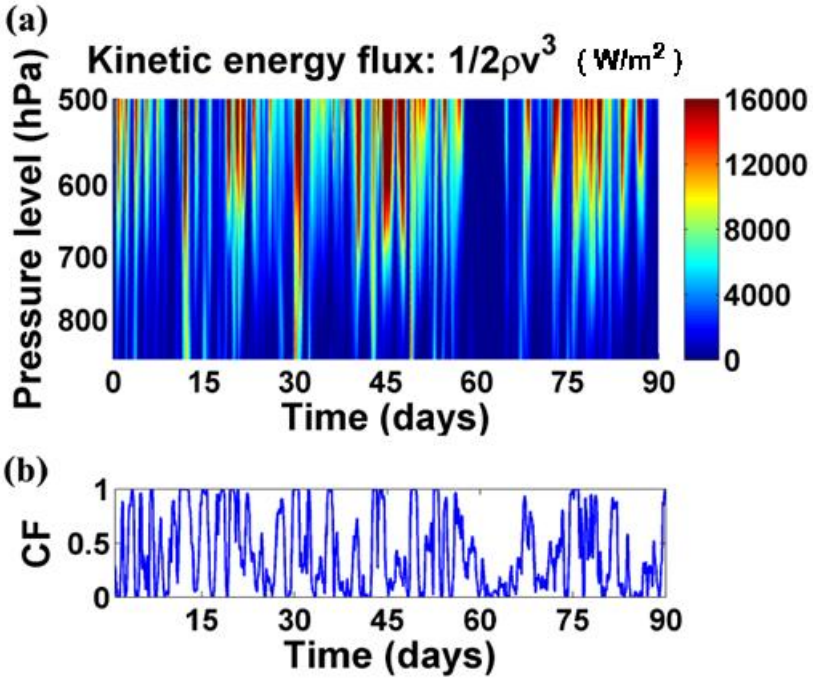

Figure 3.3 (a) Variation of the vertical profile of the kinetic energy flux per square meter in the free atmosphere between 870 hPa to 500 hPa above the a grid cell near the City of Chicago (42 ^{o}N, 88.7 ^{o}W) between period Dec 1 2004 to Feb 28 2005. (b) Variation of CF for a wind farm located in the vicinity of Chicago (42 ^{o}N, 88.7 ^{o}W) over the period Dec 1 2004 to Feb 28 2005.

The evolution of the transient waves, defined as the deviation from the seasonal mean of the geopotential height at 500 hPa is illustrated in the Figure 3.4a. Evolution of the corresponding values of CF, starting at 3:00 AM, Dec 30, 2004 is presented in Figure 3.4b. In these two snapshots separated by 15 hours, as the high pressure system (the red-colored wave pattern) moves east, the pattern of the instantaneous CF progresses in the same direction. The passage of the transient waves is responsible for the low frequency variability of the boundary layer wind (Holton and Hakim 2012; Wallace and Hobbs 2006; James 1995) and for the

corresponding variation in CF. The spatial scales of the transient waves at 500 hPa and patterns of the instantaneous CF are comparable in size to that of the continental US.

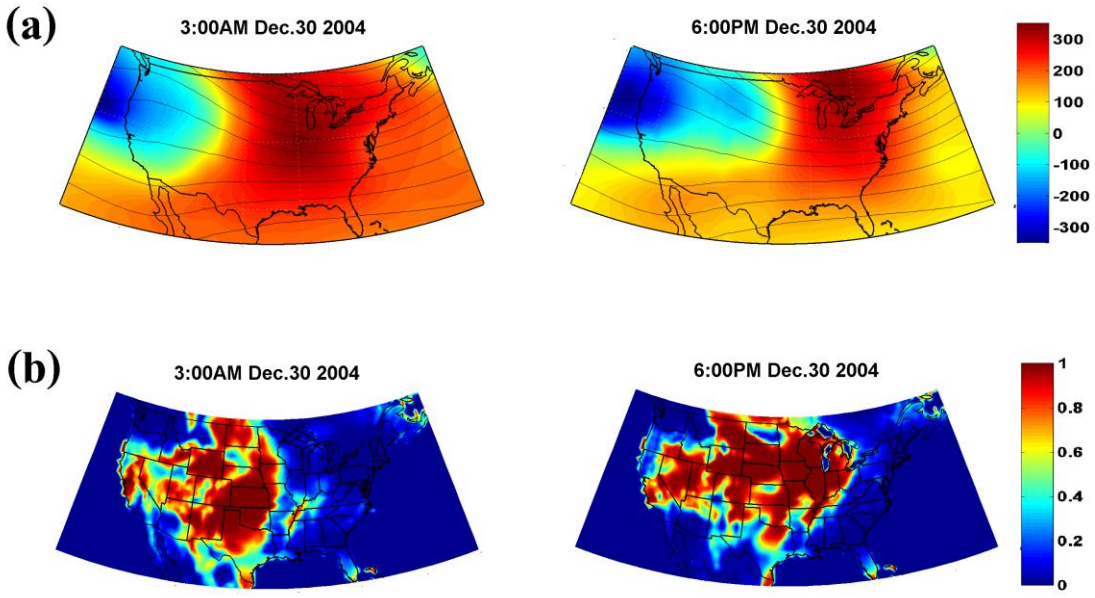

Figure 3.4 (a) Snapshot of the departure of geopotential heights from the mean for two specific times. The contours indicate the seasonal mean of geopotential heights at 500 hPa. The color defines the deviation from the seasonal mean of the geopotential height. (b) summarizes the corresponding values for CF.

3.4 Physical nature of the transient waves

The physical nature of the transient waves can be elaborated using a simple model accounting for the changing patterns of the geopotential height and the wind speed at 500 hPa together with the variation of the wind at 100 m, as discussed for example by Holton and Hakim (2012) and Wallace et al. (2006). For mid latitude transient waves:

$$\overrightarrow{V_g} = \frac{1}{f} \cdot \vec{k} \times \nabla(g \cdot z) \quad (3.3)$$

where $\overrightarrow{V_g}$ is the wind velocity in the free atmosphere (e.g. at the 500 hPa level), f is the Coriolis parameter, z is the geopotential height (e.g. at the 500 hPa level), and $\vec{k}$ is the unit vector directed upward. Variations of wind velocities in the free atmosphere respond primarily to fluctuations in geopotential height. The wind velocity in the boundary layer (e.g. 100 m) is determined by $\overrightarrow{V_g}$ in the free atmosphere as modified by random small scale turbulence generated in response to surface roughness. The dynamical sequence is as follows: transient waves z determine $\overrightarrow{V_g}$; $\overrightarrow{V_g}$ sets the surface wind; the surface wind in turn determines CF.

3.5 Spatial Influence of Transient Waves.

The relative coherence of meteorological conditions over the Central Plains region, specifically in winter when the transient waves are most intense, can be illustrated by considering spatial patterns in the cross-correlation of key meteorological parameters such as the geopotential height of the 500 hPa surface, a representative diagnostic of conditions in the free atmosphere. We choose as reference for this purpose the temporal variation of the mean value of the geopotential height at 500 hPa from 30 ^{o}N to 45 ^{o}N latitude along a longitude of 98.125 ^{o}W straddling the region of interest. Geopotential heights are evaluated throughout the region every 3 hours for the 5 winters considered here (Dec 1 2002 - Nov 30 2007) with a spatial resolution of 5/4 ^{o} latitude by 5/4 ^{o} longitude. The cross-correlation between the time series of the 500 hPa height and the reference height is calculated at each grid point as a function of time lag. The data are used then to calculate the time shift required to maximize the correlation between the two records. The magnitude of the cross-correlation computed on the basis of the time shift is illustrated in Figure 3.5a. Values derived for time shifts defining maximum cross correlation as a

function of location are indicated, with a temporal resolution of 3 hours, by the contours in the figure. The figure clearly illustrates the coherence of the meteorological conditions influencing weather over an extended region of the central US in winter. The arrow indicates the average direction of propagation for the transient waves responsible for the observed variability. The time required for the waves to transit the region is approximately 1.5 days reflecting an average propagation speed of about 30 km/hour.

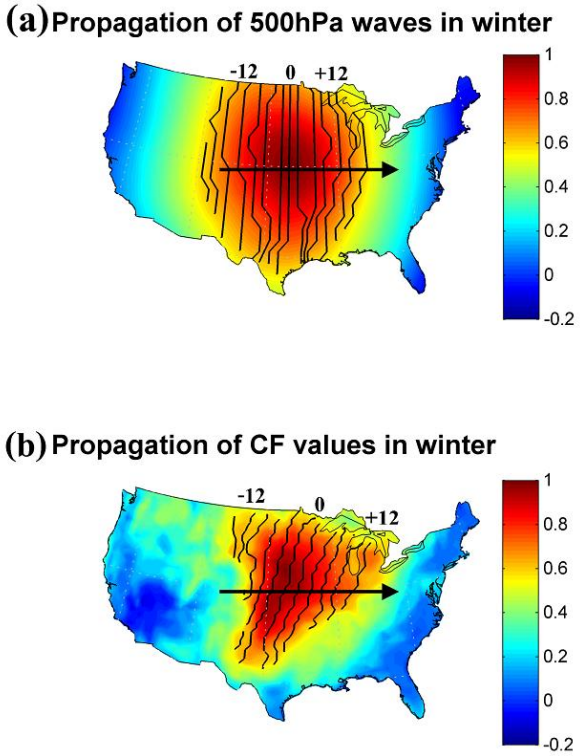

Figure 3.5 (a) Wave propagation at 500 hPa in winter. The contours indicate the time the waves take to propagate. The interval between two contour lines is 3 hours. The color defines the magnitude of the associated cross-correlation. The arrow points to the direction of propagation of the transient waves. The numbers indicate the lag time in units of hours relative to the reference. (b) Similar to 3a but for CF at 100 m.

A similar approach may be used to evaluate the variation of conditions at 100 m, the hub height for the GE 2.5 MW turbines considered here. We choose in this case to calculate the variation of the CF for GE 2.5 MW turbines distributed over the entire region of interest. The reference longitude is taken to be 98 ^{o}W, roughly the same as for the analysis summarized in Figure 3.5a. Lags corresponding to the maximum cross-correlation for CF are indicated by the contours. The difference in the overall pattern observed in Figure 3.5b as compared to Figure 3.5a reflects the impact of the variability in surface roughness associated with mountainous regions to the west in combination with forested regions to the southeast.

Transient waves propagating from west to east dominate conditions in the free atmosphere, while surface features are influenced by fronts, the near surface component of the transient wave systems, traveling typically from northwest to southeast. This accounts for the slanted nature of the contours in Figure 3.5b. Results for two representative grid cells, one near Chicago (41.875 ^{o}N, 88.125 ^{o}W) and another near Sioux City, Iowa (43.125 ^{o}N, 98.125 ^{o}W), are presented in Figures 3.6 and 3.7.

Figure 3.5 indicates that the Central Plains region is under the influence of the large scale transient waves. Electricity generated by one wind farm located in the Central Plains region is not independent of the electricity output from another wind facility in the same region. The transient waves link all the wind farms in the region of interest here. Thus the effectiveness of interconnection in reducing the low frequency variability has a limit determined by the inherent variability of the transient waves.

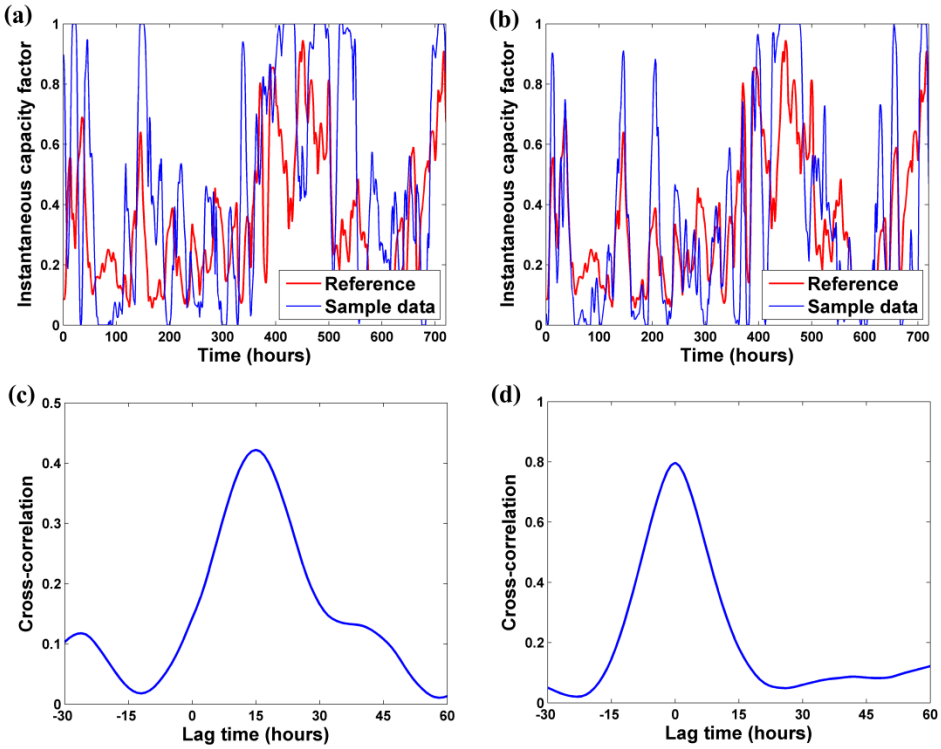

Figure 3.6 (a) Time series of the instantaneous capacity factor for the reference case in the manuscript and for a grid cell located near Chicago, starting Dec 1, 2002, covering 720 hours. (b) Similar to Figure 3.6a but for a grid cell located near Sioux City, Iowa. (c) Cross-correlation of the time series in Figure 3.6a as a function of lag time. Peak cross-correlation corresponds to a lag time of approximately 15 hours, indicating that the variation of CF for the reference case leads the variation at the selected location by about 15 hours. (d) Cross-correlation of the time series in Figure 3.6b as a function of lag time. Peak cross-correlation corresponds to a lag time of approximately 0 hours, indicating that the variation of CF for the reference case does not lead or lag the variation at the selected location which is situated on the reference longitude.

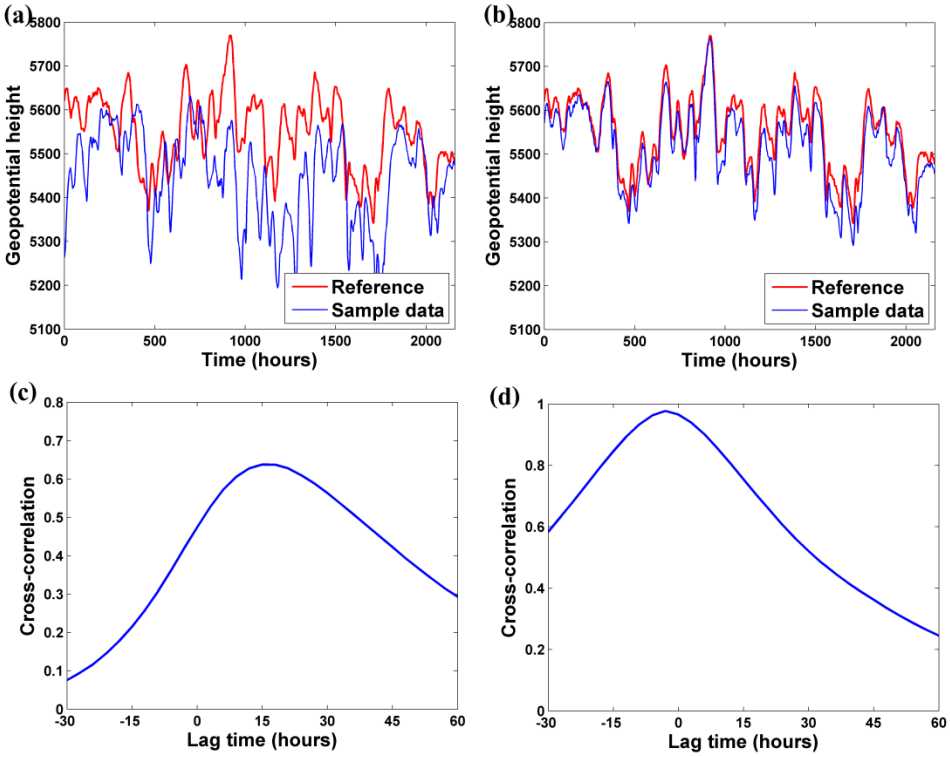

Figure 3.7 (a) Time series of the instantaneous geopotential height for the reference case in the manuscript and for a grid cell located near Chicago, starting Dec 1, 2002, covering 2160 hours. (b) Similar to Figure 3.7a but for the grid cell located near Sioux City, Iowa. (c) Cross-correlation of the time series in Figure 3.7a as a function of lag time. Peak cross-correlation corresponds to a lag time of approximately 15 hours, indicating that the variation of geopotential height for the reference case leads the variation at the selected location by about 15 hours. (d) Cross-correlation of the time series in Figure 3.7b as a function of lag time. Peak cross-correlation corresponds to a lag time of approximately 0 hours, indicating that the variation of geopotential height for the reference case does not lead or lag the variation at the selected location.

3.6 Creating a Portfolio of Wind Farms.

The spatial scale of boundary layer turbulence is relatively small, compared to the spatial scale associated with the transient waves. It is relatively easier therefore to compensate through wind farm interconnection for the variation of wind energy attributable to this small scale turbulence. The more challenging task is to reduce the variation of wind energy associated with the transient waves. The transient waves normally propagate from west to east. If their spatial scale and speeds were determined and fixed, coupling wind farms in the west-to-east direction would offer an optimal strategy. However, the waves behave stochastically in their movement and spatial scale (Holton and Hakim 2012; Wallace and Hobbs 2006; James 1995), especially in summer.

The region of interest for this study covers approximately $(1250)^2$ km^2. We consider a portfolio of N wind farms, with installed capacities adjusted to ensure equal (annual) production of electricity from each, distributed uniformly over this region. The average separation between individual wind farms is given then by $1250/N^{1/2}$ km. For any particular value of N, we consider 100 randomly selected options for location of the N individual farms. We assume that the power output from the N farms can be coupled. The expectation is that the variability in output from individual farms can be offset to some extent by out of phase variability at others.

In integrating wind energy into electrical grids, larger wind power swings pose challenges in matching supply with demand. The effective use of intermittent sources hinges on the stability of their power outputs. In this paper, we use estimates of relative standard deviation (RSD) to measure the stability of wind, with small RSD indicating stability, and vice versa. The RSD computed for the CF of the coupled system is presented as a function of season for a range

of values of N in Figure 3.8. Each point in the figure reflects a specific choice of siting for the individual wind farms (100 possibilities for each value of N). Fits to the average values of the standard deviations computed for different values of N are indicated by the continuous curves in the figure. RSD's for low values of N are large approaching 100% in some cases. Mean values of RSD decrease rapidly as a function of increasing N, approaching a relatively constant value for N greater than about 10. As N increases, the high frequency variability associated with random boundary layer turbulence can be effectively reduced, and the wide geographic distribution of the wind farms serves to capture the intrinsic variability associated with the propagation of the transient waves through the region.

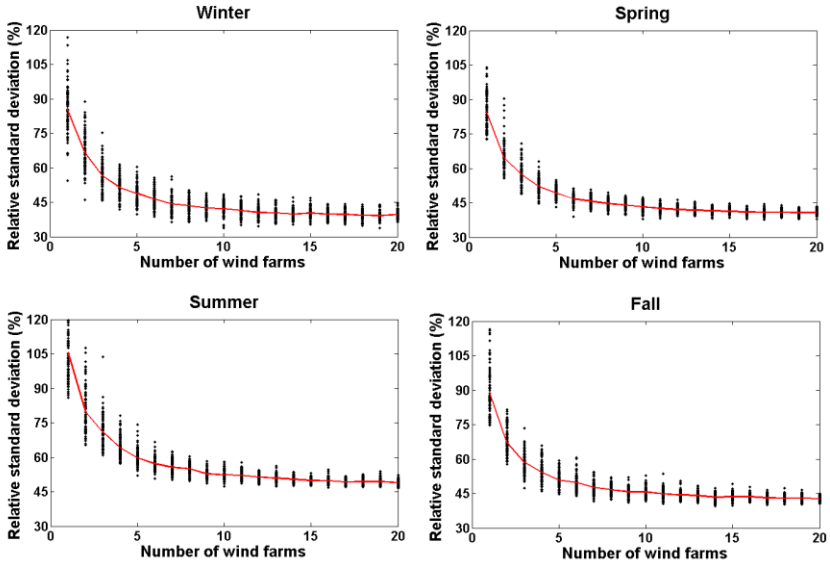

Figure 3.8 Relative standard deviation (RSD) for CF (%) for all four seasons as a function of the assumed number of wind farms (N). Individual data points reflect 100 possible location options for each value of N.

The temporal variability of the power output from the region of interest considered here can be minimized by combining outputs from approximately 5-10 spatially distributed wind farms. The decrease in the RSD of the coupled system as a function of N as indicated in Figure 3.8 reflects this condition. There is a limit however to the decrease in system variance that can be realized by coupling multiple wind farms. This absolute limit, approximately 45% for each season for the region considered here, is determined by the intrinsic variability of the transient waves.

3.7 Benefit of Interconnection

To directly illustrate the benefit that could be realized by combining wind farms, we consider ten farms, one per state, distributed over the study region as indicated in Figure 3.2 with installed capacities adjusted to ensure equal (annual) production of electricity from each of these installations. The temporal variation of the capacity factor for one of these installations, No. 5 located in Nebraska, is compared in Figure 3.9 with the output that could be realized by coupling all ten farms. Figure 3.9 summarizes results derived for all four seasons over the interval Dec 1 2004 to Nov 30 2005. The output from individual stations varies between zero and full power over times as brief as a few hours. In contrast, the output from the combined system is less variable. Peak values of CF for the composite system are typically lower than those for individual farms, and the combined system avoids the zero power condition encountered frequently for individual stations. Though not completely eliminating the variability problem, the coupled system mitigates the associated management pressure on operation of the grid. Values for the RSD of CF as a function of season are summarized for individual wind farms and for the combined system in Figure 3.10.

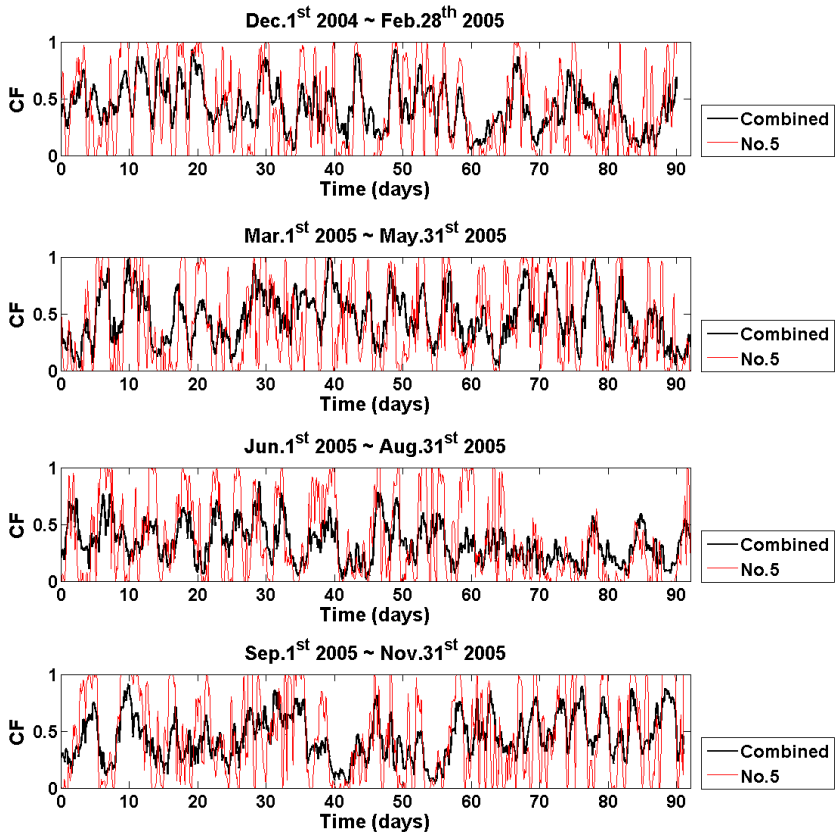

Figure 3.9 Variation of CF series for wind farm No.5 and for the combined system over the period Dec 1 2004 to Nov 30 2005.

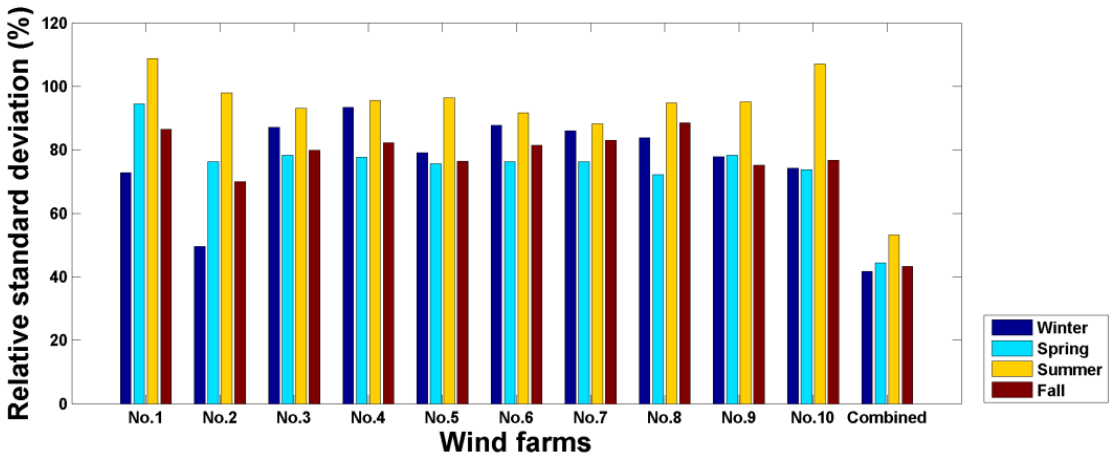

Figure 3.10 RSD of CF for all the ten wind farms and the combined system.

Outputs from the combined system and for wind farm No.5 are presented in the form of probability distributions for CF in Figure 3.11. The results summarized here cover the entire 5-year period Dec 1 2002 - Nov 30 2007. The variability of the output from a single farm is evidenced by the almost uniform distribution of CF values in Figure 3.11a (including peaks at zero and one). In contrast, the probability distribution for the combined system displays a distinct peak at 0.35 with a broad tail extending to high values of CF, with a low probability for CF values less about 0.1. The results in Figure 3.11 can be presented equivalently in terms of what is referred to as a duration curve (Holttinen and Hirvonen 2005; Archer and Jacobson 2007), the fraction of the time for which the wind farm can achieve an output exceeding a particular value of CF as a function of CF. Duration curves for wind farm No.5 and for the combined system are presented in Figure 3.12. The RSD of CF is approximately 100% for individual wind farms - greater in summer, less in winter. The RSD for the combined system is much less, approximately 45% independent of season. The pattern observed for the on-shore system investigated here is similar to that reported earlier for the off-shore Atlantic system considered by Kempton et al. (2010).

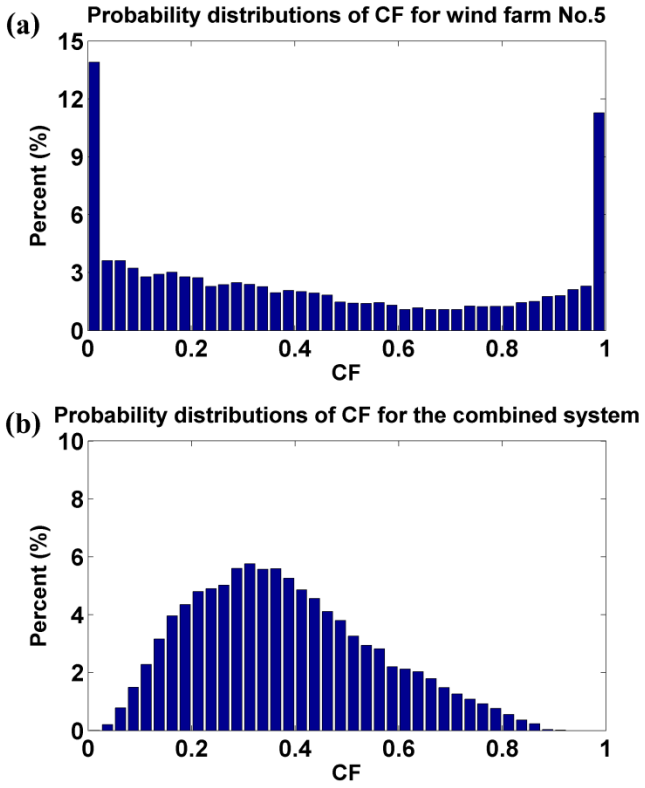

Figure 3.11 (a) Probability distributions of CF for wind farm No.5. (b) Probability distributions of CF for the combined system.

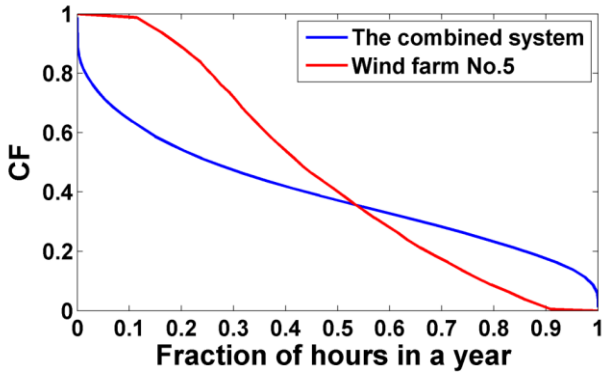

Figure 3.12 Duration curves for wind farm No.5 and the combined system. Each point on the x axis represents the fraction of hours in a year for which the capacity factor of wind farm No.5, or the combined system, is greater than or equal to the corresponding capacity factor indicated on the y axis. The duration curve can be derived by integrating the probability distributions of CF from CF=1 to CF=0.

Results for individual seasons are presented in Figure 3.13. The seasonal dispersion of values for the integrated system is significantly less for all four seasons than the dispersion observed for a particular location. For the combined wind system in summer, the peak of probability distribution shifts toward lower values of CF, reflecting a weaker general circulation and a reduced role for the propagation of transient waves in summer time.

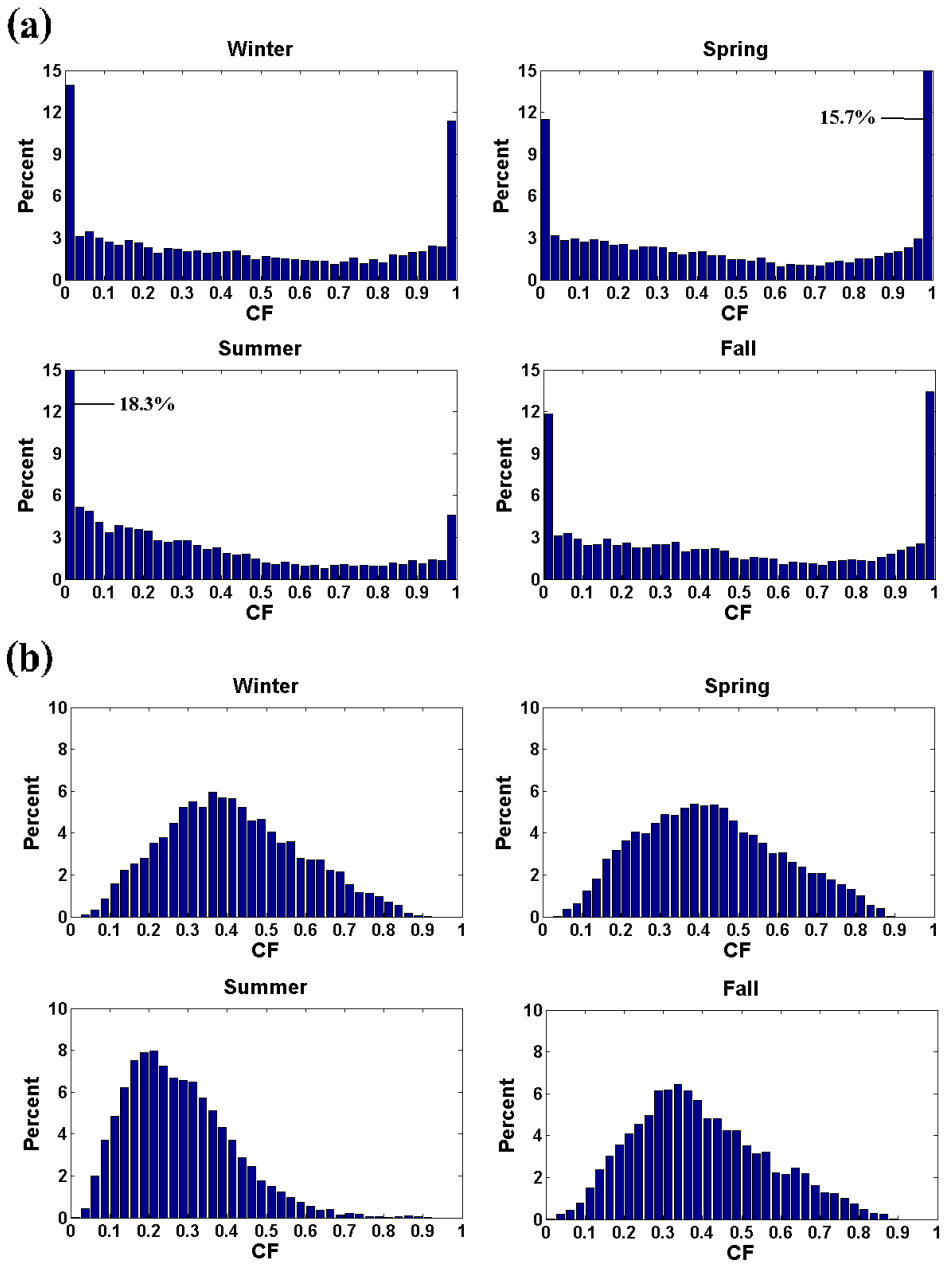

Figure 3.13 (a) CF histogram for wind farm No. 5 as a function of season. (b) CF histogram for the combined wind system as a function of season.

The frequency spectrum for the variation in the power output of the combined system is presented for all four seasons in Figure 3.14. The variability is concentrated primarily on time scales greater than a day. The importance of the diurnal frequency is evident in the figure,

particularly for summer. Results are displayed in terms of cumulative variance in Figure 3.15, emphasizing again the importance of the variability at low frequency (longer time scales) for the combined system in contrast to the more extensive range of frequencies associated with the output from a single facility. More than 90% of the variance of the combined system is concentrated at frequencies less than 0.5 day^{-1}, periods longer than 2 days.

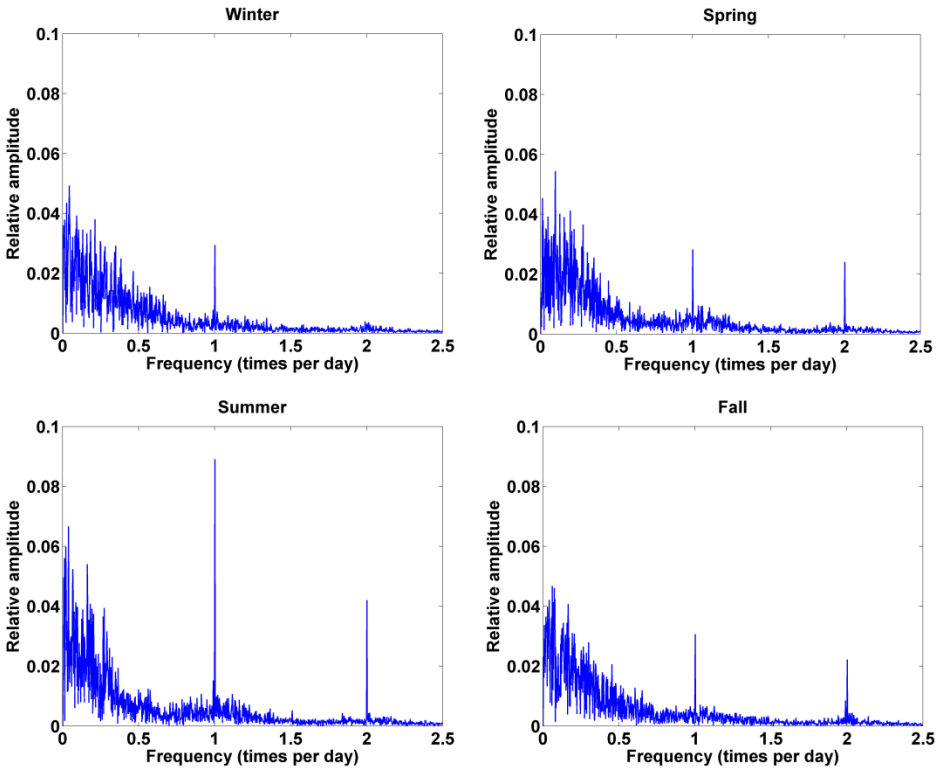

Figure 3.14 Relative amplitude spectrum of wind power (normalized to 1) for the four seasons for the integrated system. For a specific frequency, the square of the amplitude represents its contribution to the total variability.

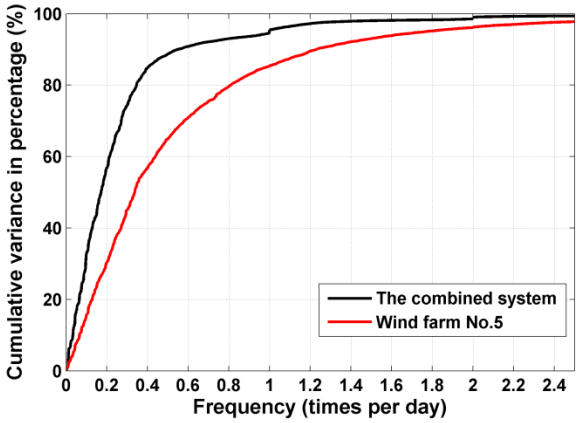

Figure 3.15 Cumulative variance of annual power output as a function of frequency for the combined system and wind farm No.5.

As indicated earlier, high frequency variability is associated with small scale turbulence in the boundary layer: the smaller the scale of the turbulence, the shorter its lifetime (Wallace and Hobbs 2006). The high frequency variability evident for a single station can be compensated effectively by comparable though uncorrelated high frequency variability at other stations. Effective elimination of the high frequency variability would allow for easier scheduling of power output from the integrated system, taking advantage of the availability and increased reliability of multi-day forecasts for regional wind conditions.

3.8 One-point correlation analysis

Many studies addressing the opportunities and challenges of interconnection have sought to define empirically the correlation in wind output between different sites (Lindenberg 2009, Simonsen and Steven 2004, Katzenstein et al. 2010, Giebel 2000). A number of papers have reported that coupling wind farms in the east-to-west direction will be more efficient than coupling in the north-to-south direction, arguing that the correlation of energy outputs between

individual wind farms decreases faster as a function of distance in east-west direction (Lindenberg 2009, Simonsen and Steven 2004).

Transient waves propagate generally in the west-to-east direction. If the waves were regular and their movements were perfectly periodic, correlation of energy outputs from two wind farms should decrease slowly in the north-to-south direction. As indicated by Figure 3.5, the pattern of propagation of transient waves in winter falls closer to this ideal situation. However, transient waves in other seasons are more stochastic: there is no general function available to explain the correlation between separated wind farms in these cases.

Figure 3.16a and 3.16b summarize correlations between hourly values of CF computed over the entire region with results obtained for two specific locations (wind farms No. 1 and 8 located in the states of Montana and Texas). Results in Figure 3.16a cover winter conditions over the five year interval from Dec 1, 2002 to Nov 30, 2007. Corresponding results for the five summers are included in Figure 3.16b. The results indicate that local meteorological conditions differ from place to place and from season to season. Consider Wind Farm No.1 in winter. The prevailing wind in the free atmosphere is strong and from northwest to southeast in this case (Wallace and Hobbs 2006). The one-point correlation decreases slowly in the northwest to southeast direction. In the case of Wind Farm No.8, the prevailing wind in the free atmosphere is from southwest to northeast (Wallace and Hobbs 2006). As a consequence, the one-point correlation decreases slowly in the southwest-to-northeast direction in this case.

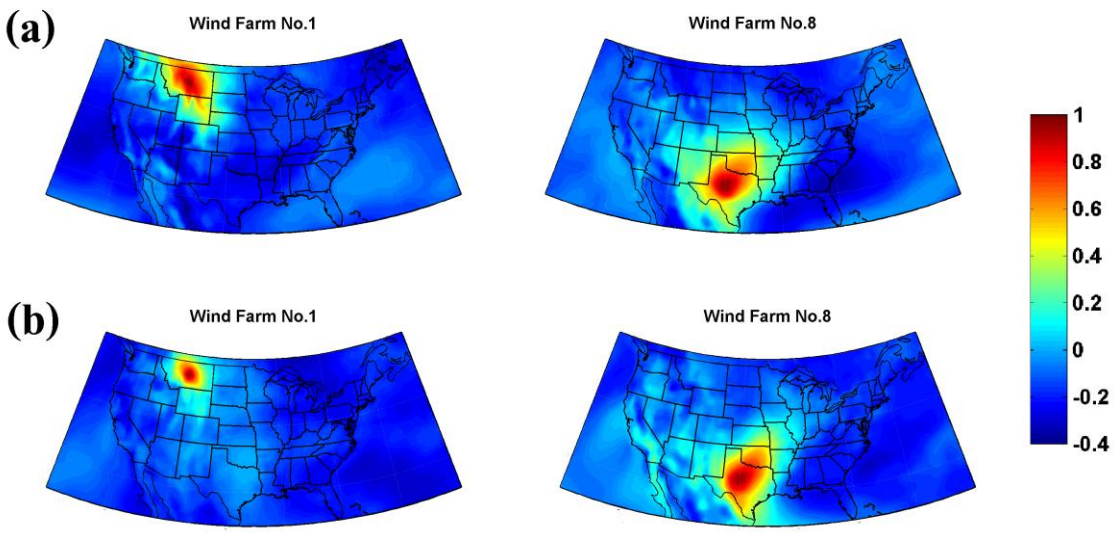

Figure 3.16 (a) One-point correlation of power output for two different wind farms in winter. (b) One-point correlation of power output for two different wind farms in summer.

3.9 Discussion

Fertig, et al. (2012) argued that fluctuations in wind power are not white noise, based on frequency-domain analysis. The high frequency variability of outputs from individual wind farms is determined, however, mainly by small scale boundary layer turbulence associated with local conditions; the low frequency variability is associated with the passage of transient waves with a characteristic time scale of several days. Fertig, et al. (2012) also concluded that the interconnection of wind plants within a single region would further reduce the ratio of fast- to slow-ramping generators. The physical explanation is associated with the impact of boundary layer turbulence: high frequency variance is determined by boundary layer turbulence, the spatial scales of which are small and the related variance can be smoothed by coupling generation systems within a single region. Coupling wind farms within a single region can reduce the high frequency variability of electricity output, and provide relatively slowly varying energy output.

Czisch, et. al (2001) pointed out that the correlation of energy outputs from two wind farms will increase if the high frequency variations of their energy outputs are filtered. The filtered energy output eliminates the signal introduced by boundary layer turbulence, while retaining the information imparted by transient waves. Because the spatial scale of the transient waves is large, the correlation calculated with the smoothed data should be enhanced.

Archer and Jacobson (2007) considered the advantages that could be realized by interconnecting wind farms over a region of 850 km by 850 km including parts of Colorado, Kansas, Oklahoma, New Mexico, and Texas. They found that an average of 33% wind power from interconnected farms could be exploited as reliable, baseload electric power. The continental US is located at mid-latitudes in a meteorological regime dominated by the influence of transient waves (Holton and Hakim 2012; Wallace and Hobbs 2006). In our study, the lag-correlation analysis indicates that the whole Central Plains region is under the influence of these transient waves. Electricity generated by one wind farm located in the Central Plains region is not independent of the power output from another wind facility in the same region. There is a limit therefore to the effectiveness of interconnection determined by the inherent variability of the transient waves.

Although this study focused on the meteorology of wind energy in the US, the method and findings can be applied to other regions. Oswald (2008) argued that while the aggregate output of a distributed wind system in the United Kingdom is smoother than the output of individual wind farms or individual regions, the power delivered by such an aggregate wind fleet is highly volatile. Surface winds in the UK are also determined by the interaction of transient waves with the local boundary layer turbulence. The UK is located downwind of the Atlantic Ocean. Transient waves there are more volatile and stronger. Since the spatial scale of the UK is

smaller than that associated with the transient waves, interconnection in this case is relatively ineffective in smoothing the variance contributed by those large scale waves.

Simonsen and Stevens's (2004) statistical analysis indicated a more rapid decrease in correlation over the east–west direction as compared to the north–south direction in the Central United States, a conclusion that is generally consistent with typical east–west direction for the passage of transient waves in that region. Based on wind data for Texas, Katzenstein, et. al (2010) also tried to establish a function explaining wind farm correlation. However, the behaviors of transient waves are relatively regular in winter, stochastic in summer. The one-point correlation analysis in this study underscores the fact that there is no general function available to define the correlation of two wind farms. Local meteorological conditions determine the correlation of individual farms and may differ from place to place and from season to season. In the case of Texas (Wind Farm No. 8) in winter, Figure 3.16 indicates a more rapid decrease in correlation in the northwest-southeast direction. In the case of Montana (Wind Farm No. 1) in winter, Figure 3.12 implies that the correlation decreases most rapidly in the northeast-southwest direction.

This study explored the strategy for an optimal deployment of a coupled system: 5~10 wind farms distributed uniformly over the Central Plains region of the US. The high frequency variability of a coupled system can be effectively eliminated. As indicated though, the low frequency variability is determined by passage of the transient waves' characteristic of meteorological conditions in this region. Interconnection alone cannot completely eliminate the challenges associated with the variability of wind-generation power, which is limited fundamentally by properties of the large scale transient waves. Effective elimination of the high frequency variability, however, would allow for easier scheduling of power output from the

integrated system, taking advantage of the increased availability and reliability of multi-day forecasting for regional wind conditions.

The temporal and spatial resolutions of the data have an impact on the variability analysis. In the real situation, the energy output from a wind farm will fluctuate at much higher frequencies than those shown by our hourly wind data, but this only reinforces the points made in the chapter. The boundary layer wind is influenced by the transient waves and the boundary layer conditions. The latter factor generates random small scale and short term turbulences. Coupling wind farms will be effective in cutting down high frequency noise attributable to this random turbulence, but ineffective in reducing the inherent variability of the transient waves. Since we use hourly data with a spatial resolution of 1/2 ^{o} latitude by 2/3 ^{o} longitude here, in which fluctuations at time scales shorter than an hour and spatial scales smaller than the resolution are ignored, the high frequency noise is underestimated in our analysis. The effectiveness of interconnection should be even more conspicuous than what we estimate in this article, in the sense that high frequency variability should be eliminated to an even greater extent.

Acknowledgement

The work described here was supported by the National Science Foundation under grant ATM-1019134 to Harvard University. Junling Huang was also supported by the Harvard Graduate Consortium on Energy and Environment.

References

Archer, C. L., and M. Z. Jacobson, 2007: Supplying Baseload Power and Reducing Transmission Requirements by Interconnecting Wind Farms. *J. Appl. Meteorol. Clim.,* **46**, 1701–1717.

Blair, N., Heimiller, D., and Singh, V., 2003: *Modeling the long-term market penetration of wind in the United States*. National Renewable Energy Laboratory.

Czisch, G., and Ernst, B., 2001: *High wind power penetration by the systematic use of smoothing effects within huge catchment areas shown in a European example.* Windpower 2001.

Fertig, E., J. Apt, P. Jaramillo, and W. Katzenstein, 2012: The effect of long-distance interconnection on wind power variability. *Environ. Res. Lett.,* **7**, 034017.

Giebel, G., 2000: On the benefits of distributed generation of wind energy in Europe. Ph.D. Dissertation, Carl von Ossietzky University of Oldenburg, 2000, 104 pp. Available at: http://www.drgiebel.de/GGiebel_DistributedWindEnergyInEurope.pdf.

Hart, E. K., and M. Z. Jacobson, 2011: A Monte Carlo approach to generator portfolio planning and carbon emissions assessments of systems with large penetrations of variable renewables. *Renewable Energy*, **36**, 2278-2286.

Holton, J. R., and G. J. Hakim, 2012: *An introduction to dynamic meteorology*. Academic press. pp 256-276.

Holttinen, H., and R. Hirvonen, 2005: *Power system requirements for wind power*. Wind Power in Power Systems, T. Ackermann, Ed., John Wiley and Sons. pp143–167.

James, I. N., 1995: *Introduction to circulating atmospheres*. Cambridge University Press. pp 112-207.

Kahn, E., 1979: The reliability of distributed wind generators. *Electr. Pow. Syst. Res.*, **2**, 1–14.

Katzenstein, W., E. Fertig and J. Apt, 2010: The variability of interconnected wind plants. *Energy Policy*, **38**, 4400–4410.

Kempton, W., F. M. Pimenta, D. E. Veron, and B. A. Colle, 2010: Electric power from offshore wind via synoptic-scale interconnection. *Proc. Natl. Acad. Sci.*, **107**, 7240–7245.

Lindenberg, S. (Ed.)., 2009: 20% Wind Energy by 2030: Increasing Wind Energy's Contribution to U.S. Electricity Supply. United States Department of Energy: Washington, DC, 2008. Available at: http://www.nrel.gov/docs/fy08osti/41869.pdf.

Lu, X., M. B. McElroy, and J. Kiviluoma, 2009: Global potential for wind-generated electricity. *Proc. Natl. Acad. Sci.*, **106**, 10933-10938.

Lu, X., M. B. McElroy, and N. Sluzas, 2011: Costs for Integrating Wind into the Future ERCOT System with Related Costs for Savings in CO_2 Emissions. *Environ. Sci. Technol.*, **45**, 3160-3166.

Masters, G. M., 2004: *Renewable and Efficient Electric Power Systems*. A John Wiley & Sons, Inc.: Hoboken, NJ.

Oswald, J., M, Raine and H. Ashraf-Ball, 2008: Will British weather provide reliable electricity? *Energy Policy*, **36**, 3202–3215.

Simonsen, T. K., and Stevens, B. G., 2004: *Regional wind energy analysis for the Central United States*. Proc Global Wind Power, 16.

Wallace, J. M., and P. V. Hobbs, 2006: *Atmospheric science: an introductory survey*. Vol. 92. Academic press. pp 313-413

Chapter 4

A 32-year Perspective on the Origin of Wind Energy in a warming Climate

Abstract

The potential for generation of electricity from wind is determined ultimately by the balance between production and dissipation of kinetic energy in the atmosphere. Based on assimilated meteorological data for the period January 1979 to December 2010, the energetics of the atmosphere is investigated from both mechanical and thermodynamic perspectives. The atmosphere acts as a thermal engine, absorbing heat at higher temperatures, approximately $256K$, releasing heat at lower temperatures, approximately $253K$. The process produces work at a rate of $2.46\,W/m^2$ sustaining thus the circulation of the atmosphere, with a thermodynamic efficiency of 1.03 %. The mid-latitude eddies contribute $2.41\,W/m^2$ to global kinetic energy production, reflecting their dominant role in the overall energetics of the atmosphere. In comparison, the zonal mean meridional circulation is responsible for a much lower source of $0.05\,W/m^2$. The analysis indicates upward trends in both kinetic energy production and thermodynamic efficiency over the past 32 years, indicating that wind energy resources may be increasing in the current warming climate.

4.1 Introduction

Global installed wind capacity reached an unprecedented level of more than 237 GW at the end of 2011, of which approximately 40 GW were added in 2011, the highest level recorded to date. Some 98 countries and regions are identified worldwide as using wind power to generate electricity. Wind turbines installed worldwide by the end of 2011 were capable of providing 500 TWh of electricity per year, accounting for approximately 3 % of total global production of electricity. Asia accounted for the largest share of new installations (53.7 %), followed by Europe (21.9 %) and North America (20.5 %). Installations in Latin America, Australia/Oceania and Africa were relatively small by comparison, 2.9 %, 0.9 % and 0.2 % respectively. Based on current growth rates, the World Wind Energy Association estimates that global wind capacity could increase to as much as 500 GW by 2015, 1000 GW by 2020 (World Wind Energy Association 2012).

A number of studies have sought to assess the ultimate potential for wind-generated electricity assuming that the deployment of turbines should not influence the potential source (Landberg et al. 2003; Hoogwijk et al. 2004; Archer and Jacobson 2005; Lu et al. 2009; Tapiador 2009; de Castro et al. 2011; Zhou et al. 2012). Using data from surface meteorological stations, Archer and Jacobson (2005) concluded that 20 % of the global total wind power potential could account annually for as much as 123 PWh of electricity, equivalent to 7 times total current global consumption. They restricted their attention to power that could be generated using a network of 1.5 MW turbines tapping wind resources from regions with annually averaged wind speeds in excess of 6.9 m/s at an elevation of 80 m. Using assimilated meteorological data, Lu et al. (2009) argued that a network of land-based 2.5 MW turbines restricted to non-forested, ice-

free, non-urban areas operating at as little as 20 % of their rated capacity could supply more than 40 times current worldwide demand for electricity, more than 5 times total global use of energy in all forms. These studies, however, did not address the fundamental physical factors that determine the overall kinetic energy budget of the atmosphere. The potential wind resource issue involves a question of flow, rather than available stock (Gustavason 1979). The quantity of wind that can be extracted from the atmosphere to generate electricity depends ultimately on the rate at which kinetic energy is produced, not on the quantity of kinetic energy actually stored in the atmosphere.

Large scale deployment of wind farms can potentially influence the circulation of the atmosphere, as discussed in a number of studies (Keith et al. 2004; Wang and Prinn 2010, 2011; Lu and Fernando 2011; Walsh-Thomas et al. 2012; Fitch et al. 2012; Fitch et al. 2013; Fitch et al. 2013). Several groups have sought to address this issue. With a simple parameterization of turbine operations, Miller et al. (2011) performed numerical experiments and found that a maximum of $34\ TW$ of electricity could be generated. Marvel et al. (2012) extended Miller's work by parameterizing the turbines as sinks for momentum extending over a number of model layers. Based on a global physics model, Kate et al. (2012) concluded that wind turbines placed at the Earth's surface could extract kinetic energy at a rate of at least $400\ TW$, whereas high-altitude wind turbines could extract more than $1{,}800\ TW$. With a different global physics model and parameterization approach, Jacobson and Archer (2012) argued that as the number of wind turbines increased over large geographic regions, power extraction would first increase linearly, then converge to a saturation limit, with a saturation potential in excess of $250\ TW$ at 100 m globally, $380\ TW$ at 10 km. There is a notable discrepancy between these various limits. Kate's results suggest a significant expansion of the Hadley circulation as a consequence of kinetic

energy extraction. Adams and Keith (2011) addressed the same question using a mesoscale model. However, the energetics of the entire atmosphere is different from the energetics of the mesoscale region considered by Adams and Keith (2011). Answering the question of the ultimate limit of the atmosphere as a source of wind-generated electric power requires a detailed study of the underlying physics of the global atmosphere.

The circulation of the atmosphere is driven primarily by the spatial gradient in heat input. Diabatic heating occurs mainly in the warm tropics, with diabatic cooling dominating at relatively cold mid and high latitudes. The atmosphere acts as a fluid system transporting heat from hot to cold regions via the general circulation (Lorenz 1967). In this sense, following Carnot, the atmosphere acts as a thermal engine, converting heat to kinetic energy to sustain the general circulation against the force of friction. The standard approach to investigate the energetics of the atmosphere was introduced by Lorenz in 1955. This theory provides a means to quantify total kinetic energy production, addressing not only the globally integrated contributions from the meridional-mean circulation but also the contributions from eddies. A number of groups have investigated the energetics of the atmosphere based on the Lorenz Energy Cycle (Oort 1964; Oort and Yienger 1996; Li 2007; Marques et al. 2010; Kim and Kim 2013). Using Modern Era Retrospective-analysis for Research and Applications (MERRA) data, Kim and Kim (2013) concluded that kinetic energy is produced globally at a spatially average rate of about 2 W/m^2. However, the geographic distribution of kinetic energy production including the temporal variability have not as yet been quantified.

This study investigates the origin of wind energy in the atmosphere, with a specific focus on the spatial distribution of sources (C), historical long term variations and the thermodynamic efficiency (η) of the atmosphere viewed as a heat engine. From a mechanical perspective, kinetic

energy can be produced or destroyed only by real forces (Lorenz 1967). In the case of an air parcel in the atmosphere, the real forces are: gravity, the pressure gradient force, and friction. The first half of this paper focuses on the production of kinetic energy by these forces. The creation of wind energy in the atmosphere involves absorption of heat at high temperature and release at low temperature, following the operational principle of a thermal engine. The second half of the paper analyzes the thermodynamic processes within the atmosphere, quantifying the key thermodynamic variables including the net rate of heat absorption (Q_{in}), the efficiency for kinetic energy production (η_K) and the associated generation of entropy (S).

4.2 Data

The study is based on meteorological data from the MERRA compilation covering the period January 1979 to December 2010. Wind speeds, air temperatures and geopotential heights were obtained on the basis of retrospective analysis of global meteorological data using Version 5.2.0 of the GEOS-5 DAS. We use the standard 3-hourly output available for 42 pressure levels with a horizontal resolution of 1.25 ^{o} latitude × 1.25 ^{o} longitude (Rienecker et al. 2007). The global surface temperature anomalies referenced in this study are from the Goddard Institute for Space Studies (GISS) (Hansen et al. 2010).

4.3 Atmospheric kinetic energy

The kinetic energy corresponding to unit mass of the atmosphere is given by $(u^2 + v^2)/2$ where u and v are the eastward and northward components of wind velocity respectively (the small increment of kinetic energy associated with vertical motion can be ignored). The total and hemispheric atmospheric kinetic energy stocks may be obtained by integrating over the

appropriate spatial domains. Composite results for monthly mean values and for the long-term variation of global kinetic energy are shown in Figure 4.1. The inter-annual variation of the total kinetic energy stock shown in Figure 4.1a is associated with the changing phases of the El Niño - Southern Oscillation (ENSO) cycle. During the warm El Nino phase (notably years 1983, 1987, 1997 and 2010), elevated sea surface temperatures (SSTs) result in an increase in the kinetic energy stock; during the cold phase La Nina phase (notably years 1985, 1989, 1999 and 2008), colder SSTs contribute to a decrease. The global kinetic energy stock averaged approximately 1.50 MJ/m^2 over the past 32 years, 1.31 MJ/m^2 in the Northern Hemisphere with 1.70 MJ/m^2 in the Southern Hemisphere.

The spatial distributions of the annual mean, June - August, and December - February kinetic energy budget are shown in Figure 4.2. Clearly evident is the influence of the dominant storm tracks at mid-latitude, and the steady components of the subtropical and polar jet streams. There are two distinct peaks in the Northern Hemispheric kinetic energy stock east of Japan and east of the North American continent, with a more continuous belt of high kinetic energy located between 30 ^{o}S and 60 ^{o}S in the Southern Hemisphere. As discussed by Huang et al. (2014), the boundary layer wind, for example the wind at 100 m, is controlled by conditions in the free atmosphere, perturbed by fast varying turbulence in the boundary layer. Strong winds in the free atmosphere generally lead to strong winds near the surface, and consequently to high instantaneous values of the capacity factors for wind turbines. The spatial distributions in Figure 4.2 reflect the geographic distribution and seasonality of wind resources as reported in the earlier studies (Lu et al. 2009; Heide et al. 2010; Archer and Jacobson 2013).

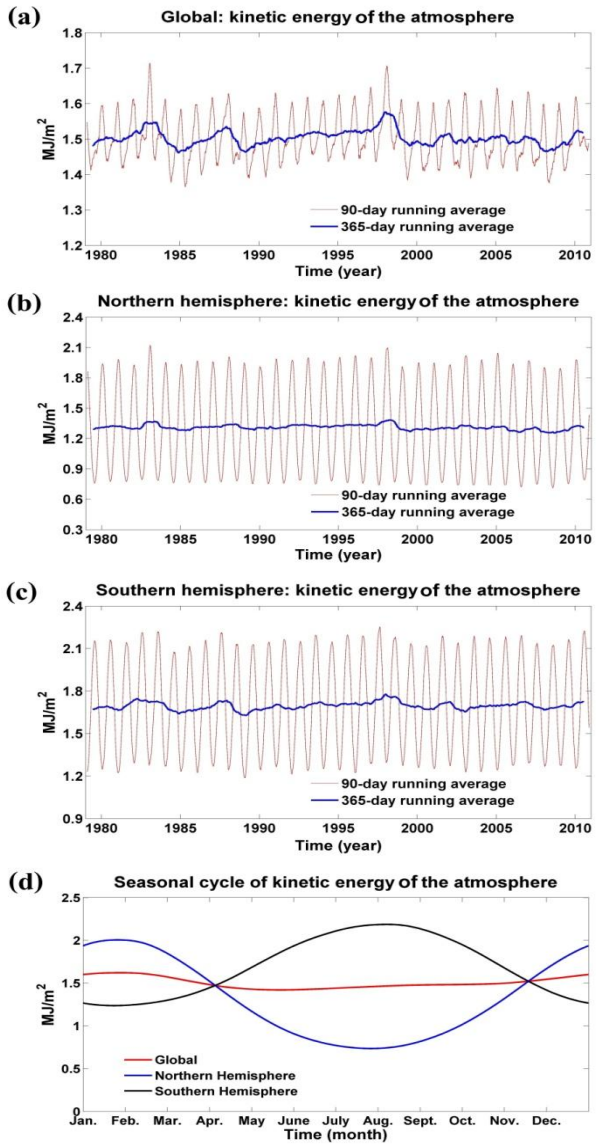

Figure 4.1 Kinetic energy of the atmosphere: (a) variation of the global kinetic energy from January 1979 to December 2010; (b) variation of the Northern Hemisphere kinetic energy from January 1979 to December 2010; (c) variation of the Southern Hemisphere kinetic energy from January 1979 to December 2010; (d) the composite seasonal cycle of the kinetic energy of the atmosphere averaged over the past 32 years.

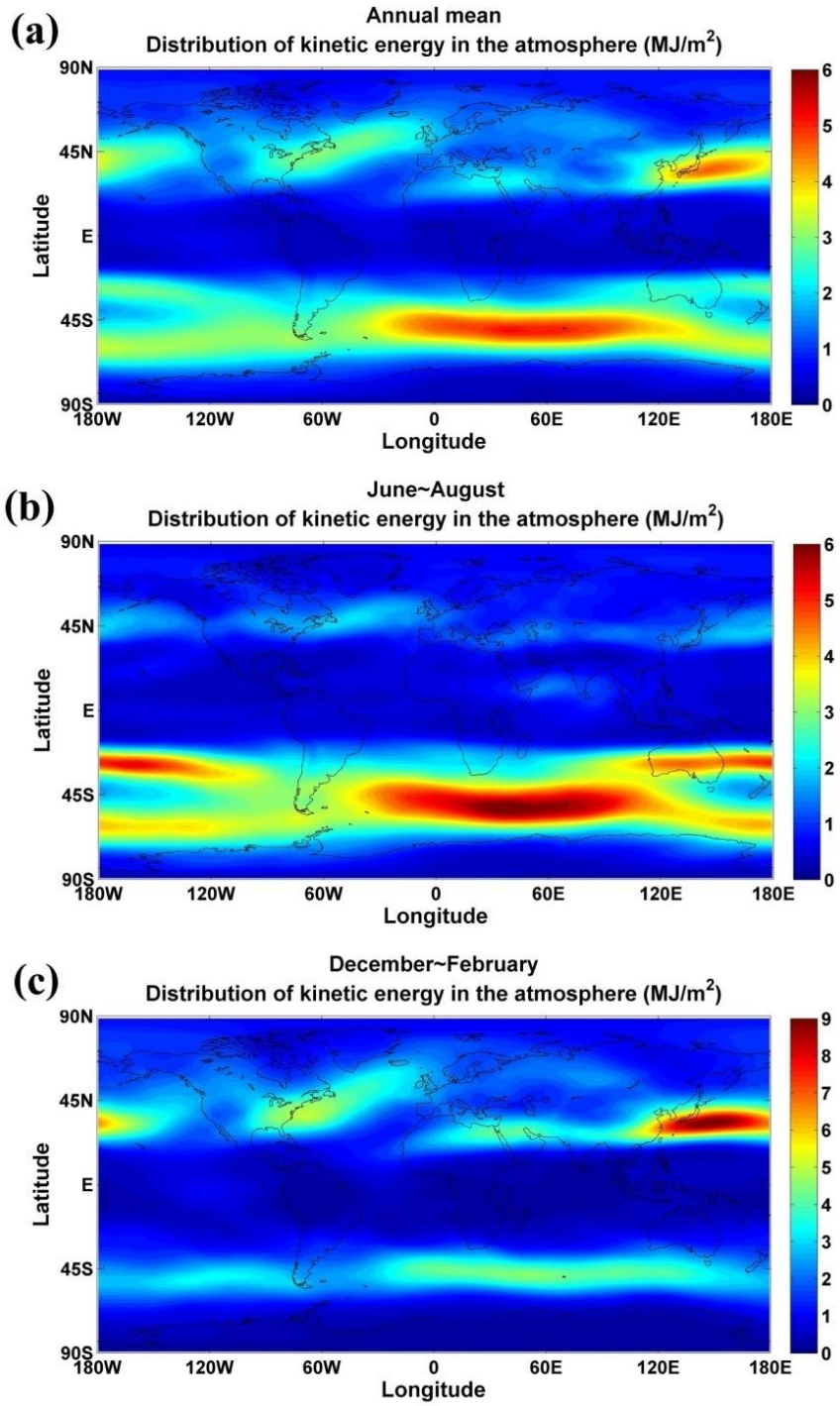

Figure 4.2 Spatial distribution of the kinetic energy of the atmosphere in MJ/m^2: (a) annual mean, calculated based the past 32 years' data; (b) June ~ August, calculated based the past 32 years' data; (c) December ~ February, based on the past 32 years' data.

4.4 Calculation of the kinetic energy production rate

For an air parcel of unit mass, production of kinetic energy may be written as:

$$\frac{dK}{dt} = -gw - \frac{1}{\rho}\vec{v} \cdot \nabla p + \vec{v} \cdot \vec{F} \tag{4.1}$$

where K is the kinetic energy corresponding to unit mass, g is the gravitational acceleration, w is the vertical velocity, $\vec{v}$ is the velocity, ρ is the air density, p is the pressure and $\vec{F}$ is the frictional force.

In calculating the kinetic energy production rate, it is convenient to consider the rate for production of kinetic energy in a fixed unit of volume. Re-organizing equation (4.1), we have:

$$\frac{\partial \rho K}{\partial t} = -\nabla \cdot (K\rho\vec{v}) - \vec{v} \cdot \nabla p + \rho\vec{v} \cdot \vec{F} - g\rho w \tag{4.2}$$

The left hand side of this equation denotes the rate per unit volume for production of kinetic energy. The right hand side defines contributions to this production rate associated with the convergence of the kinetic energy flux ($-\nabla \cdot (K\rho\vec{v})$), and the work carried out or consumed by the pressure gradient force ($-\vec{v} \cdot \nabla p$), friction ($\rho\vec{v} \cdot \vec{F}$) and gravity ($-g\rho w$). The data employed in the present analysis have a temporal resolution of 3 hour. Averaging over this 3 hour interval, equation (4.2) may be written as

$$\frac{\partial \widetilde{\rho K}}{\partial t} = -\nabla \cdot \widetilde{(K\rho\vec{v})} - \widetilde{\vec{v} \cdot \nabla p} + \widetilde{\rho\vec{v} \cdot \vec{F}} - g\widetilde{\rho w} \tag{4.3}$$

where the symbol " $\widetilde{\ }$ " denotes the appropriate three hour average.

The atmosphere is in quasi-hydrostatic balance: gravity is balanced approximately by the vertical pressure gradient force (Peixoto and Oort 1992). In this case, equation (4.3) may be recast in the simpler form:

$$\frac{\partial \widetilde{\rho K}}{\partial t} = -\nabla \cdot \left(\widetilde{K\rho\vec{v}}\right) - \widetilde{\overrightarrow{v_h} \cdot \nabla_h p} + \widetilde{\rho\vec{v} \cdot \vec{F}} \tag{4.4}$$

where $\overrightarrow{v_h}$ is the horizontal component of $\vec{v}$, and $\nabla_h p$ is the horizontal gradient of the pressure force.

Given the limitations imposed by the temporal and spatial resolution of the data, the kinetic energy associated with small scale turbulent motions must be treated as a component of the internal thermal energy (Lorenz, 1967). Equation (4.4) can be rewritten as:

$$\frac{\partial \widetilde{\rho K}}{\partial t} = -\nabla \cdot \left(\widetilde{K}\tilde{\rho}\tilde{\vec{v}}\right) - \widetilde{\overrightarrow{v_h}} \cdot \widetilde{\nabla_h p} - \nabla \cdot \left(\widetilde{K\rho\vec{v}} - \widetilde{K}\tilde{\rho}\tilde{\vec{v}}\right) - \widetilde{\overrightarrow{v_h}' \cdot \nabla_h p'} + \widetilde{\rho\vec{v} \cdot \vec{F}} \tag{4.5}$$

where " $'$ " denotes the transient component of any variable with a timescale for variation of less than 3 hours.

Part of the convergence of kinetic energy and kinetic energy production associated with the small scale turbulence is absorbed in the dissipation term reflecting the temporal and spatial resolution of the data: $D = \nabla \cdot \left(\widetilde{K\rho\vec{v}} - \widetilde{K}\tilde{\rho}\tilde{\vec{v}}\right) - \widetilde{\rho\vec{v} \cdot \vec{F}} + \widetilde{\overrightarrow{v_h}' \cdot \nabla_h p'}$. Production of kinetic energy resulting from the horizontal pressure-gradient force is estimated as $C = -\widetilde{v_h} \cdot \widetilde{\nabla_h p}$. Thus, the production of kinetic energy term C as explored in this study is restricted to include only contributions from meteorological processes with timescales longer than 3 hours and with spatial scales greater than 1.25 ^{o} latitude by 1.25 ^{o} longitude.

4.5 The distribution of the production of kinetic energy

Figure 4.3 illustrates the distribution of kinetic energy production averaged over the past 32 years in units of $10^{-3}\ W/kg$. The tropical and subtropical region from 30 ^{o}S to 30 ^{o}N, dominated by the thermally direct Hadley circulation, is responsible for a net source of kinetic

energy as indicated in Figure 4.3a. The most prominent sources are located in the mid-latitude oceanic regions below the $800\ hPa$ pressure level, notably in the Southern Hemisphere, as depicted in Figure 4.3c. The production of kinetic energy in these regions is associated with the intense development of eddies that stir the atmosphere over the ocean, carrying cold air equatorward and warm air poleward, resulting consequently in cross-isobaric flow. The topographic forcing of the Tibetan plateau has a noticeable impact on the production of kinetic energy in the upper region of the atmosphere from $0\ hPa \sim 600\ hPa$, as indicated in Figure 4.3b.

The global and hemispheric rates for production of kinetic energy are obtained by integrating the production term, C , over the entire atmosphere or over each hemisphere separately. The global kinetic energy production rate averaged over the past 3 decades is estimated at $2.46\ W/m^2$, with a upward trend since the late 1990s (Figure 4.4a). The average rate for production in the Northern Hemisphere is $2.44\ W/m^2$, $2.49\ W/m^2$ for the Southern Hemisphere. Hemispheric production rates indicate strong seasonality (Figure 4.4c), reaching maximum power output during local winter, with minima in local summer.

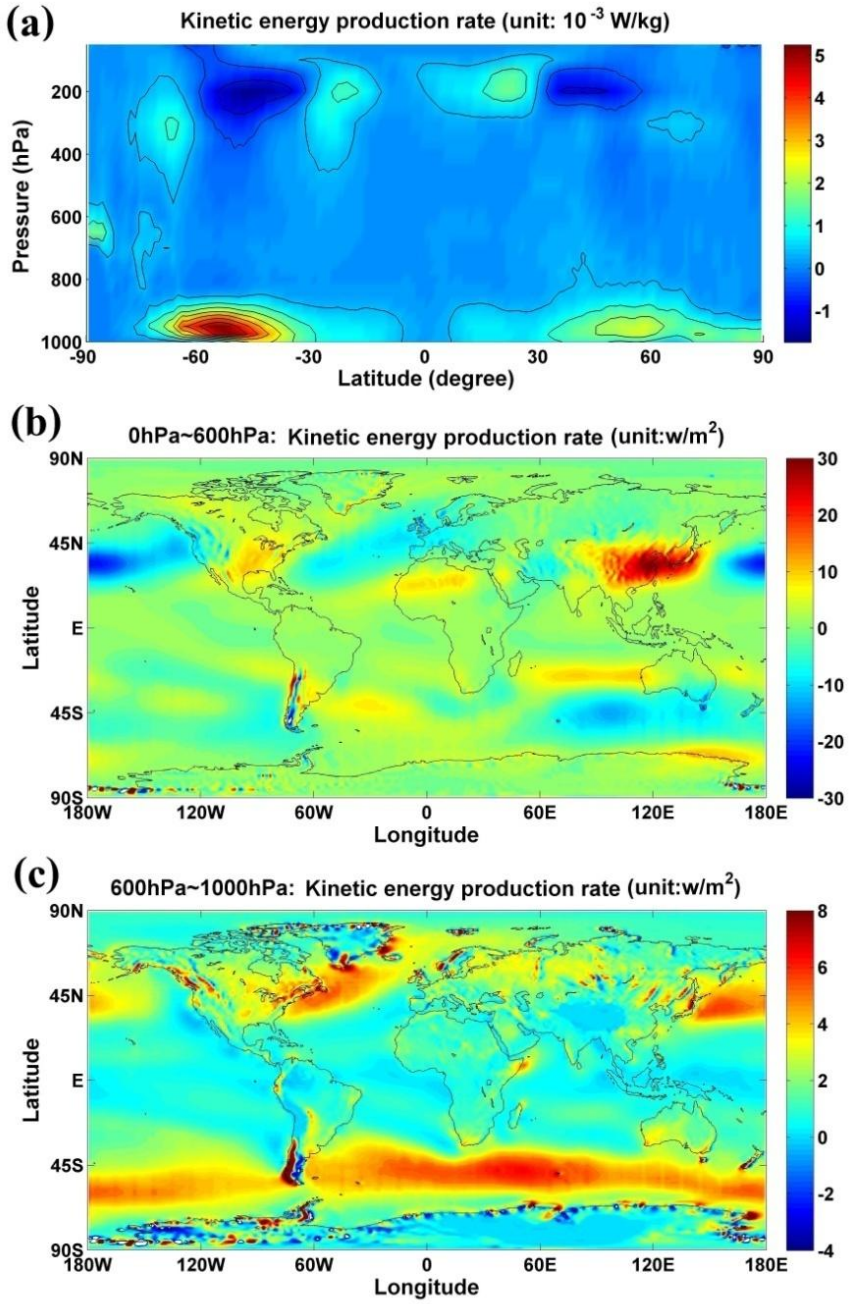

Figure 4.3 The distribution of kinetic energy production: (a) the vertical profile of kinetic energy production rate; (b) the source and sink of kinetic energy in the layer between $0\ hPa \sim 600\ hPa$; (c) the source and sink of kinetic energy in the layer between $600\ hPa \sim 1000\ hPa$.

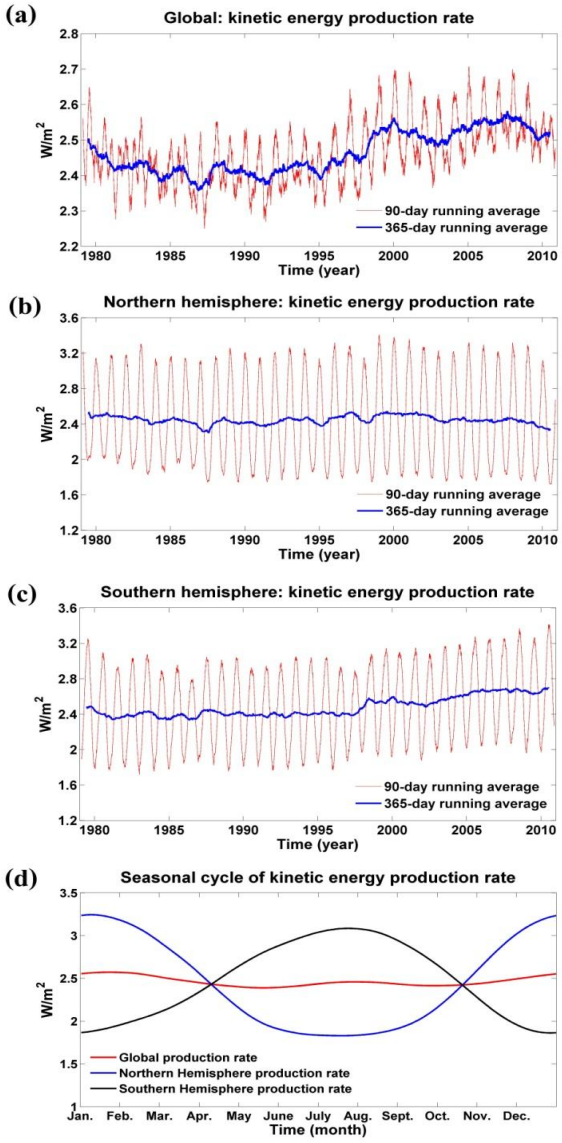

Figure 4.4 Kinetic energy production, C: (a) variation of the global kinetic energy production rate, C, from January 1979 to December 2010; (b) variation of the Northern Hemisphere kinetic energy production trend, C, from January 1979 to December 2010; (c) variation of the Southern Hemisphere kinetic energy production trend, C, from January 1979 to December 2010; (d) the composite seasonal cycle of the kinetic energy production rate, C, based on the past 32 years' data.

4.6 Meridional and Eddies contributions

The general circulation of the atmosphere can be split into two components: the zonal mean meridional circulation and the eddies. Accordingly, the production of kinetic energy due to cross-isobaric flow can be partitioned into a zonal contribution and a contribution from eddies:

$$-\widetilde{v_h} \cdot \widetilde{\nabla_h p} = -[\widetilde{v_h}] \cdot \left[\widetilde{\nabla_h p}\right] - [\widetilde{v_h}^* \cdot \widetilde{\nabla_h p}^*] \tag{4.5}$$

where the bracket **[ ]** defines the zonal mean operator, * represents the departure from the zonal mean, $C_Z = -[\widetilde{v_h}] \cdot \left[\widetilde{\nabla_h p}\right]$ is the contribution from the meridional circulation and $C_E = -[\widetilde{v_h}^* \cdot \widetilde{\nabla_h p}^*]$ represents the contribution from eddies (Lorenz 1967).

The meridional term C_Z reflects the fact that kinetic energy in the zonal mean flow can be generated by horizontal cross isobaric flow down the north-south pressure gradient. It is dominated by three systems: the Hadley system in the tropics, the Ferrel system at mid-latitudes and the Polar system at high-latitudes (Huang and McElroy 2014). The Hadley circulation in the tropics is identified with lifting of warm moist air in the equatorial region with descent of colder drier air in the subtropics corresponding to a thermally driven direct circulation, with consequent net production of kinetic energy. The Ferrel cells at mid-latitudes represent statistical residues that result from zonal averaging of large northward and southward flows associated with the quasi-stationary atmospheric waves. The Ferrel cells are identified with rising of relatively cold air at high latitudes, and sinking of relatively warm air at lower mid-latitudes, defining a thermally indirect circulation with consequent consumption of kinetic energy. The polar cells are weak, reflecting residual direct circulations. The temperature contrast at mid-latitudes is particularly strong. The Ferrel system is efficient consequently in consuming kinetic energy, effectively cancelling production from the combination of the Hadley and Polar systems. The

value of C_Z averaged over the past 32 years is $0.05\,W/m^2$. The long-term variation and the seasonal cycles of C_Z are plotted in Figure 4.5.

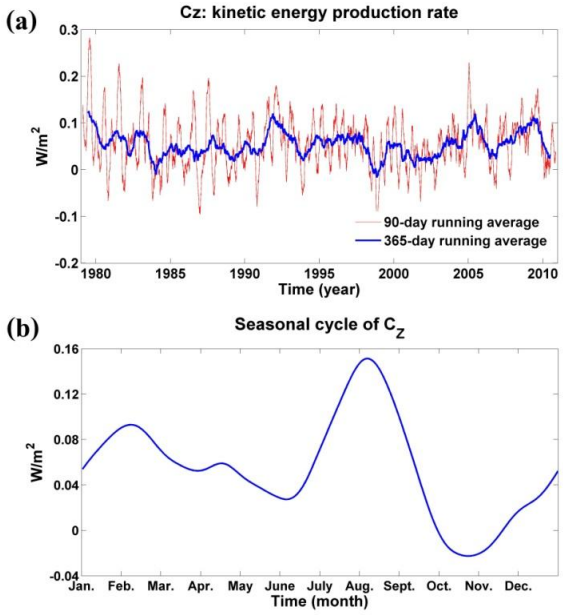

Figure 4.5 Meridional circulation's contribution to kinetic energy production: (a) variation of the global $\boldsymbol{C_Z}$ kinetic energy production from January 1979 to December 2010; (b) the composite seasonal cycle based on the past 32 years' data.

The eddies are associated with rapidly developing and decaying weather disturbances at mid-latitudes, which progress generally to the east with the prevailing flow and are responsible for much of the variability of wind and weather especially in winter. The eddy term C_E generates kinetic energy when, along a latitude circle, the wind anomalies are negatively correlated with anomalies in the pressure gradient. The temporal variation of the global and hemispheric integrals of C_E are presented in Figure 4.6a ~ c, with an upward trend in the integral for the southern hemisphere. Over the past 32 years, the average value of the southern hemispheric C_E is $2.53\,W/m^2$, greater than the value of $2.29\,W/m^2$ associated with the eddy component in the

northern hemisphere. The hemispheric integral of C_E reaches a maximum in local winter, with a minimum in local summer, as reflected in Figure 4.6d. Compared to C_Z, with the Ferrel system cancelling the Hadley system, C_E is the dominant term in the calculation of $C = C_E + C_Z$, emphasizing the dominant role of the eddies in maintaining the circulation of the atmosphere.

4.7 Dissipation

Motions of the atmosphere against friction convert kinetic to internal thermal energy. This process is thermally irreversible, resulting in an increase in entropy. Approximately half of the frictional dissipation takes place within the lowest kilometer of the atmosphere, a result of turbulent motions generated mechanically by the flow over the underlying surface. The other half takes place higher in the atmosphere where small-scale disturbances are generated as a result of convection or shear instability of the vertical wind (Kung 1966). In the long run, the total kinetic energy in the atmosphere (KE) is determined by a balance between production (C) and dissipation by friction (D). The dissipation term may be defined:

$$D = C - \frac{dKE}{dt} \tag{4.6}$$

The long-term variation and seasonal cycle of D are plotted in Figure 4.7. Maximum dissipation occurs in February, corresponding to the peak in Northern Hemisphere kinetic energy reflecting the importance of surface roughness associated with Northern Hemisphere continental areas in dissipating kinetic energy. The fate of kinetic energy in the atmosphere from a mechanical perspective is summarized in Figure 4.8. The lifetime of kinetic energy, τ, calculated as KE/D, is 6.9 days.

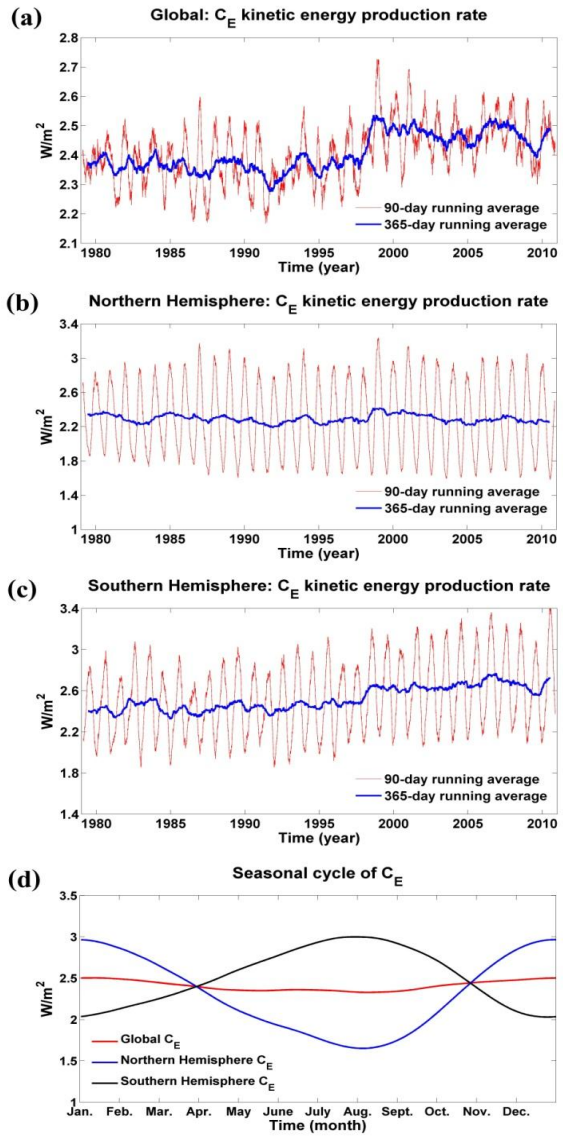

Figure 4.6 Eddies' contribution to kinetic energy production: (a) variation of the global C_E kinetic energy production from January 1979 to December 2010; (b) variation of the Northern Hemisphere C_E kinetic energy production from January 1979 to December 2010; (c) variation of the Southern Hemisphere C_E kinetic energy production from January 1979 to December 2010; (d) the composite seasonal cycle of C_E, based on the past 32 years' data.

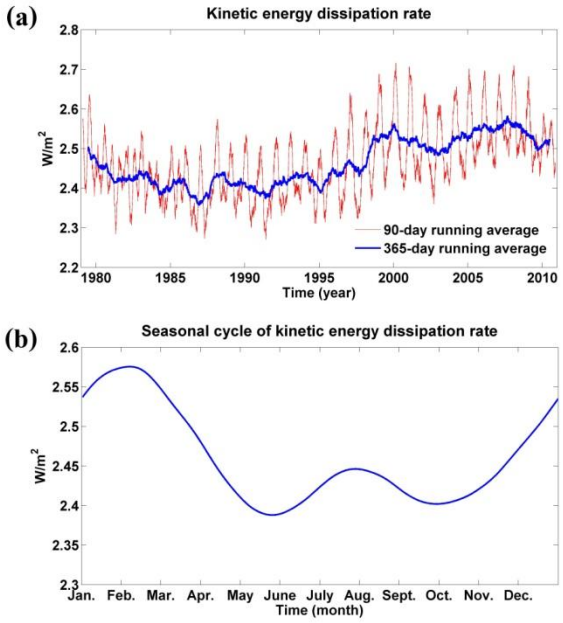

Figure 4.7 Kinetic energy dissipation rate, D: (a) variation of kinetic energy dissipation rate from January 1979 to December 2010; (b) the composite seasonal cycle based on the past 32 years.

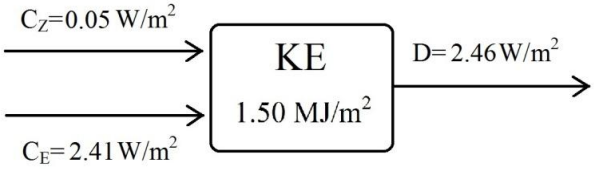

Figure 4.8 Mechanical perspective on the budget of atmospheric kinetic energy.

4.8 The thermodynamics of atmospheric motions

According to the first law of thermodynamics:

$$C_p\left[\frac{\partial}{\partial t}T + \vec{v}\cdot\nabla T + \omega\left(\frac{\partial T}{\partial p} - \kappa\frac{T}{P}\right)\right] = Q \tag{4.7}$$

where C_P is the specific heat of the air, T is temperature, ω is the vertical component of wind velocity, p is air pressure and Q defines the rate per unit mass for diabatic heating.

Diabatic heating includes contributions from radiative heating and cooling, release of latent heat associated with phase transitions, heating by conduction of sensible heat, and heating by frictional dissipation:

$$Q = -\frac{1}{\rho}\{\nabla\cdot F_{rad} + \rho L(e-c) + \nabla\cdot J_H + \tau : \nabla\vec{v}\} \tag{4.8}$$

where ρ is the density of air, L is the latent heat of condensation per unit mass, c and e are the rates of condensation and evaporation per unit mass, F_{rad} is the net radiative flux, J_H is the sensible heat flux due to conduction, τ is the wind tress tensor, and $\vec{v}$ is the wind velocity.

The annual mean spatial distribution of diabatic heating Q based on equation (4.7) is displayed in Figure 4.9. The results presented here are consistent with earlier studies (Hagos et al. 2010; Ling and Zhang 2013). An important fraction of the incoming sunlight reaches the surface which is heated accordingly. This heat finds its way back into the atmosphere as a result of turbulent transport through the atmospheric boundary layer. Most of the solar energy absorbed by the ocean is used to evaporate water. Water vapor in the atmosphere acts as a reservoir for storage of heat that can be released later. As the air ascends, it cools. When it becomes saturated, water vapor condenses with consequent release of latent heat. Heating is dominated in the

tropical atmosphere by release of latent heat. Separate bands of relatively deep heating are observed at mid-latitudes where active weather systems result in enhanced precipitation and release of latent heat. The focus in this study is on how atmospheric motion is maintained by diabatic heating. Condensation and evaporation of water are treated accordingly as external to the system composed of dry air (Johnson 1997). Regions of diabatic cooling, dominated by long wave radiation to space, occupy much of the middle and upper troposphere. The calculation of Q involves the relatively uncertain value of the vertical velocity ω; energy is not perfectly conserved in the assimilated meteorological data. Significant uncertainty is introduced consequently in computed values of Q. The rate of change of entropy, s, per unit mass is given by $\frac{ds}{dt} = Q/T$. The spatial distribution of entropy generation is similar to the spatial pattern of Q, as illustrated in Figure 4.10.

The diabatic heating term Q can be written as $Q = Q_h + Q_f$, where Q_h accounts for radiative heating (solar and infrared), latent heating and heating due to conduction:

$$Q_h = -\frac{1}{\rho}\{\nabla \cdot F_{rad} + \rho L(e - c) + \nabla \cdot J_H\} \tag{4.9}$$

The second component, Q_f, is associated with frictional dissipation:

$$Q_f = -\frac{1}{\rho} \cdot \tau : \nabla \vec{v} \tag{4.10}$$

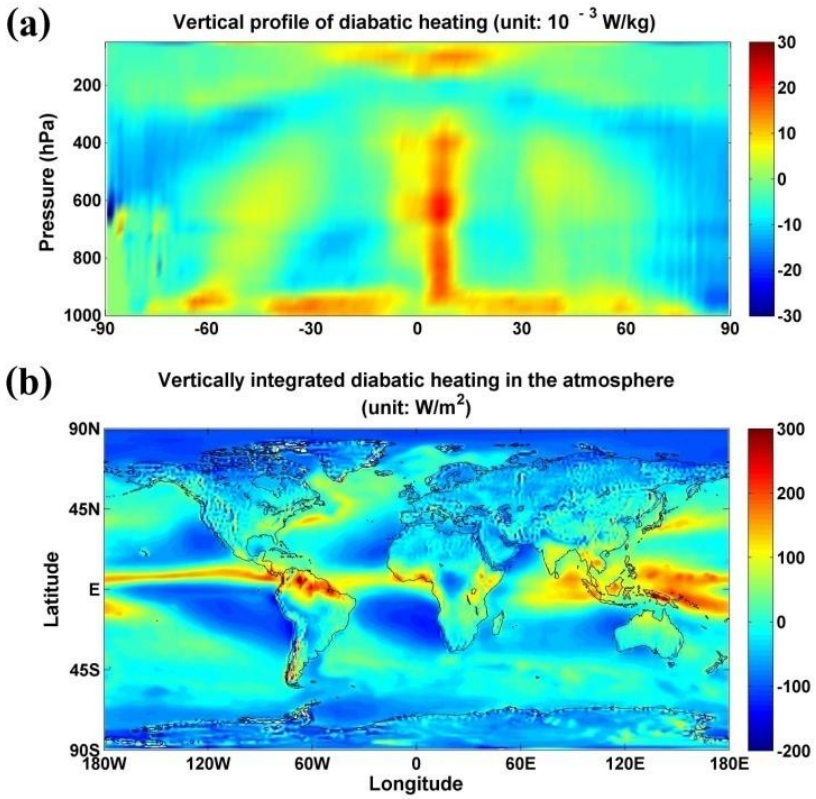

Figure 4.9 Distribution of diabatic heating: (a) vertical profile; (b) vertically integrated results.

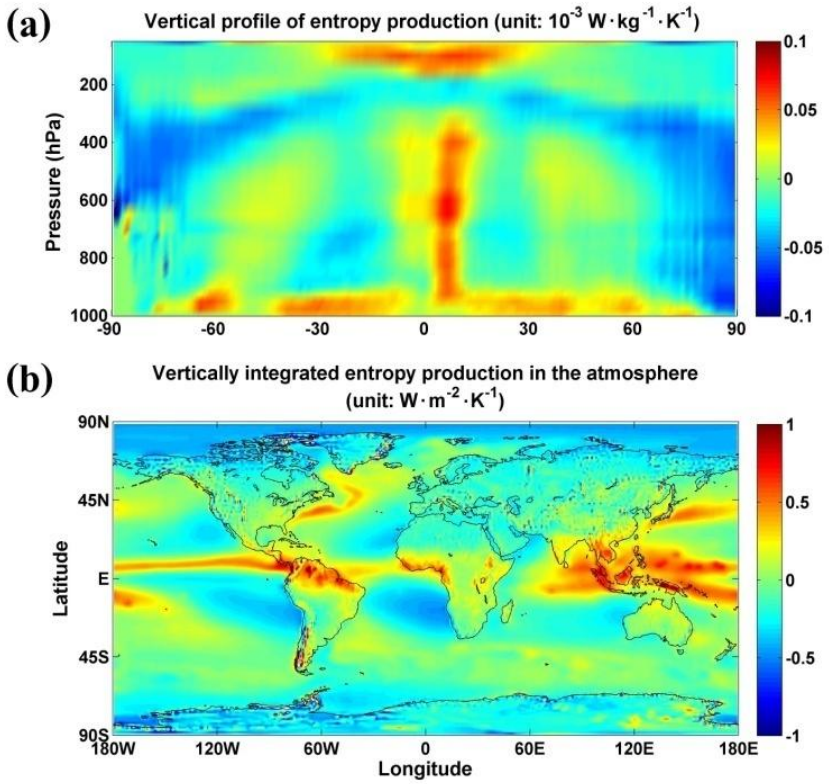

Figure 4.10 Distribution of entropy production: (a) vertical profile; (b) vertically integrated results.

By separating Q_h from Q, we may consider Q_h as the external heating responsible, from a thermodynamic perspective, for the motion of the dry air. In the long run, the globally integrated values for Q_f must be balanced by global production of kinetic energy, equal therefore to 2.46 W/m^2. Consequently, we may rewrite the generation of entropy as:

$$\frac{ds}{dt} = \frac{ds_h}{dt} + \frac{ds_f}{dt} \tag{4.11}$$

where $\frac{ds_h}{dt} = Q_h/T$, $\frac{ds_f}{dt} = Q_f/T$ and T is the temperature of the environment in the region where heat is either absorbed or released (Peixoto and Oort 1991, 1992).

In the long run, the entropy S of the entire atmosphere is required to remain constant. Thus, with the long term mean indicated by " $\bar{}$ ":

$$\int_{global} \overline{\rho \frac{(ds_h + ds_f)}{dt}} dV = 0 \tag{4.12}$$

or

$$\int_{global} \overline{\rho(\frac{Q_h + Q_f}{T})} dV = 0 \tag{4.13}$$

Since Q_f and T are always positive, the integral $\int_{global} \overline{\rho(\frac{Q_f}{T})} dV$ is greater than zero, which implies that $\int_{global} \rho(\frac{Q_h}{T}) dV < 0$. It follows that the Q_h and T fields must be positively correlated. In other words, the general circulation can be maintained against the disordering impact of friction only if the heating occurs in warmer regions of the atmosphere with cooling in colder regions. Figure 4.11 summarizes the creation and dissipation of kinetic energy in the atmosphere from a thermodynamic perspective.

The global heat source Q_{in} in Figure 4.11 represents the heat that the atmosphere absorbs in the higher temperature (T_{hot}) environment in order to do mechanical work. It is defined as:

$$Q_{in} = \int_{Q_h > 0} \rho Q_h dV \tag{4.14}$$

The global heat sink Q_{out} in Figure 4.11 represents the heat that the atmosphere releases into the lower temperature (T_{cold}) environment and is defined by:

$$Q_{out} = \int_{Q_h < 0} \rho Q_h dV \tag{4.15}$$

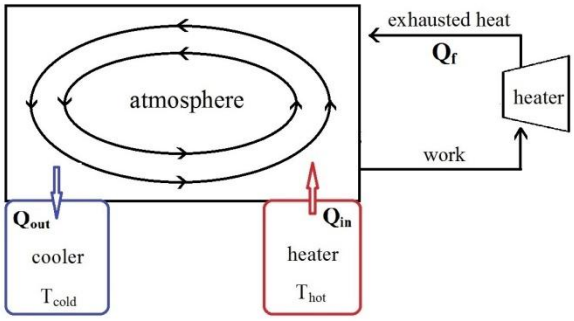

Figure 4.11 Schematic depiction of the atmosphere as a thermal engine.

The mechanical work produced by the atmosphere is dissipated by friction and converted to heat that is released back into the atmosphere. This process is thermally equivalent to using the mechanical work to turn on a heater and return the exhausted heat back to the atmosphere, as depicted in Figure 4.11. However, it is difficult to distinguish between Q_h and Q_f, and the absolute value of the global integral of Q_f is negligible compared to the global integral for Q_{in} and Q_{out}. Thus, the global heat source Q_{in} can be approximated as:

$$Q_{in} \approx \int_{Q>0} \rho Q dV \tag{4.16}$$

with Q_{out} approximated as:

$$Q_{out} \approx \int_{Q<0} \rho Q dV \tag{4.17}$$

The global heat source approximated by $\int_{Q>0} \rho Q dV$ must be balanced in the long run by $\int_{Q<0} \rho Q dV$. The uncertainty in the computation is unavoidable: a 3 W/m^2 value has been added to the global heat sink term $\int_{Q<0} \rho Q dV$ in order to conserve energy. The computed historical variation and seasonality are shown in Figure 4.12. The value for the global heat source

$\int_{Q>0} \rho Q dV$ averaged over the past three decades is estimated at $244\ W/m^2$, with the average kinetic energy production rate over the same period calculated as $1.61\ W/m^2$. It follows that the average efficiency for kinetic energy production (η_K) is equal to 1.03%.

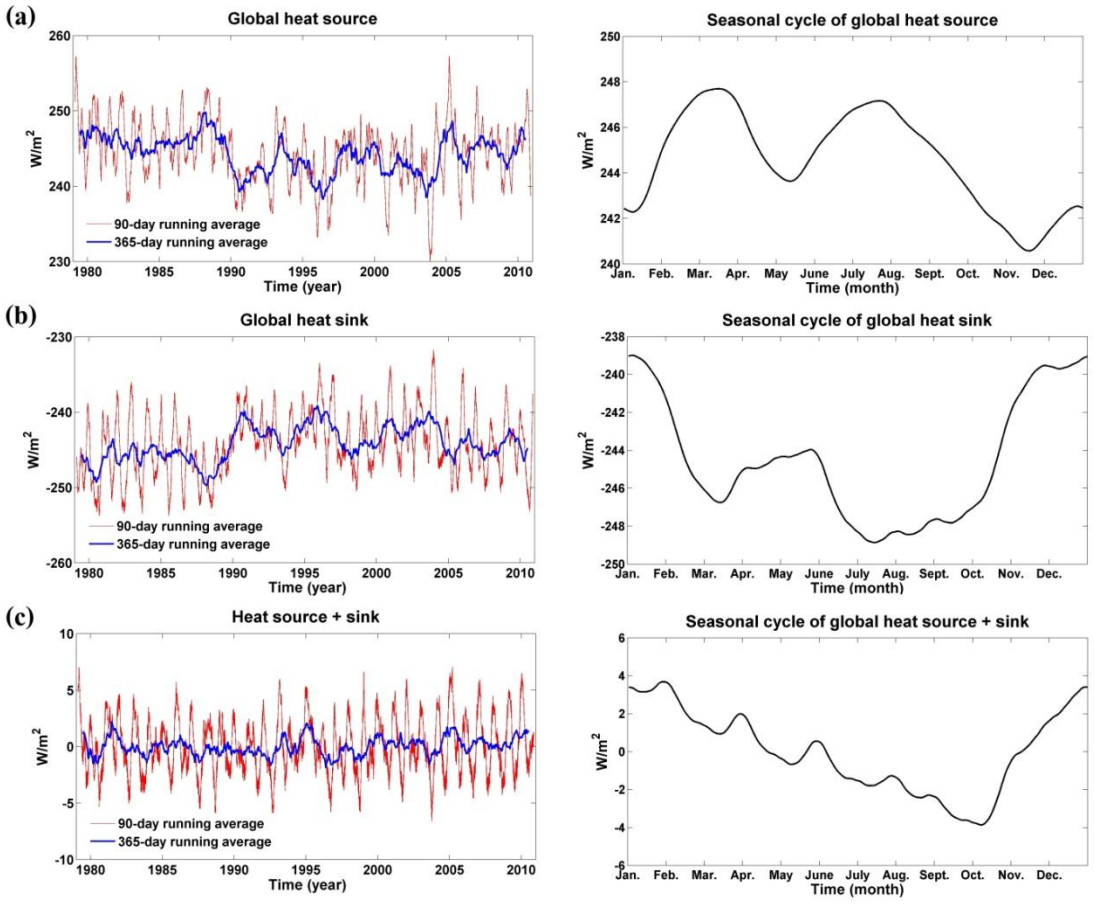

Figure 4.12 Global integral of diabatic heating, Q_{in}, and cooling, Q_{out}: (a) the long term variation (left) and seasonality (right) of the global heat source; (b) the long term variation (left) and seasonality (right) of the global heat sink; (c) the long term variation (left) and seasonality (right) of the sum of the source and sink from January 1979 to December 2010.

According to the first law of thermodynamics, a thermal engine can convert thermal heat into mechanical energy. In the case of the atmosphere, the mechanical energy includes potential energy and kinetic energy. In the energy cycle theory, Lorenz investigated the flow of energy between the kinetic energy component and the sum of internal thermal and potential energies. Here, in order to analyze the thermodynamic efficiency, the potential energy must be studied separately. The historical variation and its seasonality are plotted in Figure 4.13. Potential and internal thermal energy are not independent. Under the hydrostatic equilibrium condition, they are proportional with a ratio of approximately 2.5 (Peixoto and Oort 1992). Thus the total potential energy of the atmosphere has increased in response to recent global warming. The correlation between the potential energy of the atmosphere (365-day running average) and the GISS annual mean surface temperature trend exceeds 0.70 over the past 32 years. The historical variation and seasonality of potential energy production (P) are plotted in Figure 4.14.

Several groups have sought to estimate the thermodynamic efficiency of the atmosphere. They defined the efficiency as the ratio of the rate at which wind energy is dissipated to the total absorbed flux of solar radiation (Lorenz 1967; Gustavson 1979; Gordon and Zarmi 1989). The ultimate source of wind energy is the sun, but the conversion of this radiant energy into the kinetic energy of moving air is a complex process involving many interacting energy transfer paths. In this study, we isolated the atmospheric component from the earth system as a whole and investigated how diabatic heating in the atmosphere maintains the general circulation. Following the heat engine concept, we defined the thermodynamic efficiency, η, as the ratio between the production of mechanical energy, $C + P$, and the global integral of diabatic heating, $\int_{Q>0} \rho Q dV$. The long-term historical variation of η shows an upward trend since 1985 (Figure 4.15a). The

seasonal cycle of η is plotted in Figure 4.15b, with a peak of 1.08% in January and a minimum of 1% in September.

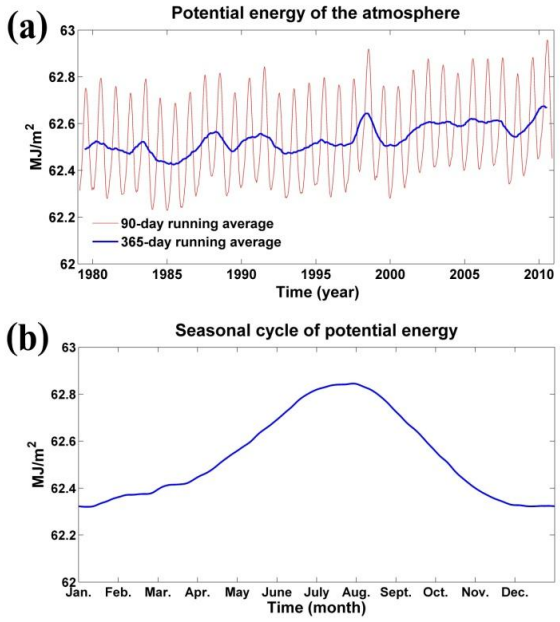

Figure 4.13 Potential energy of the atmosphere: (a) variation of the global potential energy of the atmosphere from January 1979 to December 2010; (b) the composite seasonal cycle based on the past 32 years' data.

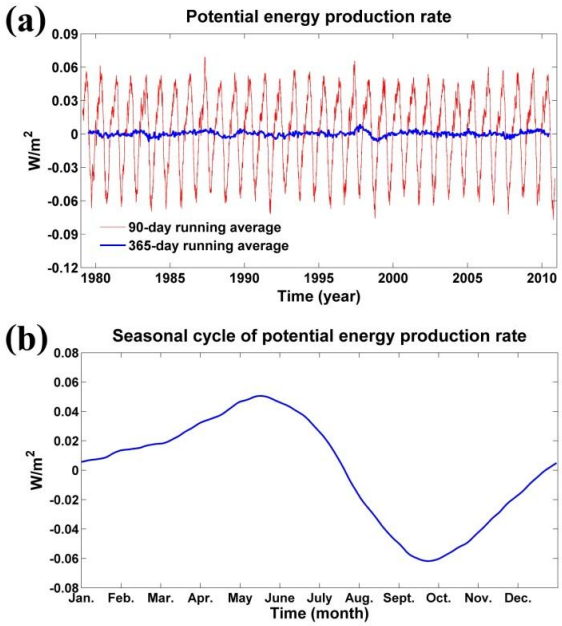

Figure 4.14 Potential energy production rate: (a) variation of the potential energy production rate from January 1979 to December 2010; (b) the composite seasonal cycle based on past 32-years data.

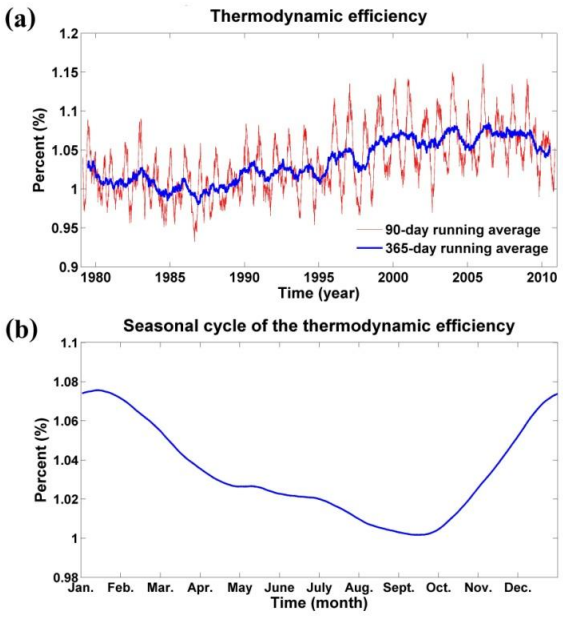

Figure 4.15 Thermodynamic efficiency, η: (a) variation of the thermodynamic efficiency from January 1979 to December 2010; (b) the composite seasonal cycle for the thermodynamic efficiency based on past 32-years data.

The effective temperature $\langle T_{hot} \rangle$ at which heat is absorbed can be calculated as:

$$\langle T_{hot} \rangle = \frac{1}{\Delta S} \int_{t_1}^{t_2} \int_{Q_h>0} T \frac{dS}{dt} dV dt \tag{4.18}$$

or approximated as:

$$\langle T_{hot} \rangle \approx \frac{1}{\Delta S} \int_{t_1}^{t_2} \int_{Q>0} T \frac{dS}{dt} dV dt \tag{4.19}$$

where $\Delta S = \int_{t_1}^{t_2} \int_{Q_h>0} \frac{dS}{dt} dV dt,$ with t_1 and t_2 representing the starting and ending times for the integration. The effective temperature $\langle T_{cold} \rangle$ at which heat is released can be approximated as $(1-\eta) \cdot \langle T_{hot} \rangle$. The schematic illustration of the atmosphere as a Carnot engine is summarized in Figure 4.16, with all values included here representing averages for the past 32 years.

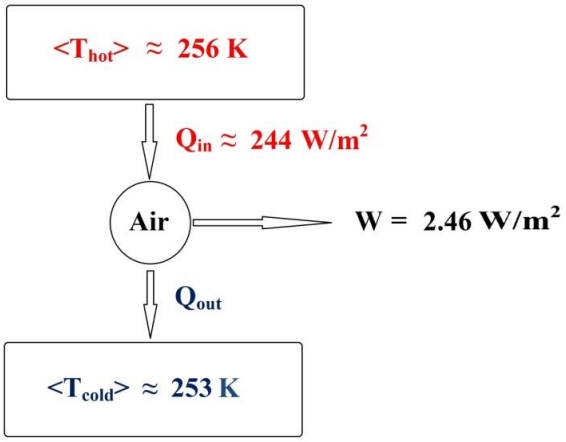

Figure 4.16 Illustration of the atmosphere as a Carnot engine. Work, W, is dissipated ultimately by friction.

The variation of $\Delta\langle T_{hot}\rangle$ is defined as:

$$\Delta\langle T_{hot}\rangle = \frac{1}{\Delta S}\int_{t_1}^{t_2}\int_{Q_h>0} T\frac{dS}{dt}dVdt - 256K$$

(4.20) or

$$\Delta\langle T_{hot}\rangle = \langle T_{hot}\rangle - 256K \tag{4.21}$$

and $\Delta\langle T_{cold}\rangle$ is given by:

$$\Delta\langle T_{cold}\rangle = \langle T_{hot}\rangle \cdot (1-\eta) - 253.5K \tag{4.22}$$

The historical variation of $\Delta\langle T_{hot}\rangle$ and $\Delta\langle T_{cold}\rangle$ is shown in Figure 4.17. The calculation of the values displayed here involves integrations over 1 year intervals (namely, $t_2 - t_1 = 1\ year$). Thus the seasonal variations have been removed. The correlation between $\Delta\langle T_{hot}\rangle$ and GISS's $\Delta T_{surface}$ is 0.89 over the past 32 years. Linear regression analysis indicates that $T_{surface}$ increased at a rate of 0.17 $K/decade$ while $\Delta\langle T_{hot}\rangle$ and $\Delta\langle T_{cold}\rangle$ increased at higher rates of 0.45 $K/decade$ and 0.38 $K/decade$ respectively, consistent with increasing efficiency.

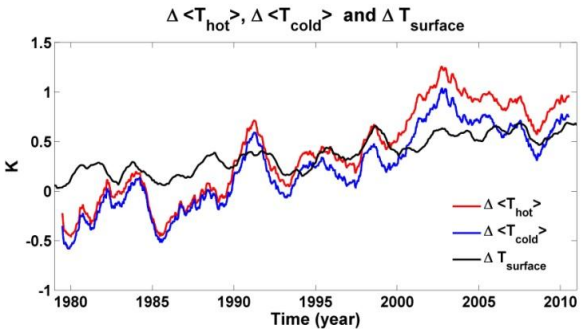

Figure 4.17 Variation of $\Delta\langle T_{hot}\rangle$, $\Delta\langle T_{cold}\rangle$ and $\Delta T_{surface}$ over the past 32 years.

4.9 Discussion and Summary

The total kinetic energy stock of the atmosphere displays significant inter-annual variability, as indicated in Figure 4.1, with the changing phases of the ENSO cycle playing an important role. This inter-annual variation reflects the fact that the wind energy potential for a particular location can fluctuate on a long-term basis, under the influences of long-term atmospheric oscillations which can alter the circulation of the atmosphere including the distribution of kinetic energy. Modern wind turbines are designed to work with an anticipated lifespan of 20 years. Predictions of wind power for the next 20 years, or at least limits on its possible variation, will be an important consideration for prospective investors in wind power. Measurements of wind speed at turbine hub heights are limited. The selecting of sites for wind farms are made usually on basis of a few years of data. Future studies should allow for the potential variation of wind resources associated with atmospheric phenomena as represented for example by ENSO, anticipating further the possibility of potential long-term changes in climate.

Production of kinetic energy was investigated in this study taking advantage of the high temporal resolution of the MERRA dataset. In calculating the kinetic energy production rate, C was defined as $-\widetilde{\mathrm{v_h}} \cdot \widetilde{\nabla_\mathrm{h}\mathrm{p}}$, where $\widetilde{\mathrm{v_h}}$ and $\tilde{\mathrm{p}}$ represent 3-hour mean values. Thus values for C are

functions of the time-average-operator " $\tilde{}$ ". Figure 4.18 displays values for the global integral of C calculated as a function of the time averaging applied to v_h and p. The global integral of C decreases from the previously reported value of $2.46\ W/m^2$ to $1.74\ W/m^2$, if the analysis is constructed using daily average values of v_h and p. It decreases to $0.51\ W/m^2$ using weekly averaging. The kinetic energy production rate curve in Figure 4.18 flattens at approximately $0.6\ W/m^2$ for averaging intervals of 5-days or longer, indicating that large-scale motions with time scales of days in the atmosphere contribute only a small fraction ($\approx 25\ \%$) of the total source of kinetic energy. Since small scale variability with time scales less than 3 hours cannot be distinguished in the dataset used here, the production of kinetic energy in the atmosphere quantified here and in other studies (e.g.: Oort 1964; Oort and Yienger 1996; Li et al. 2007; Marques et al. 2010; Kim and Kim 2013) must be considered as lower limits to the actual source as a result of restrictions imposed by the choice of time averaging.

The atmosphere generates kinetic energy as a thermal engine. Key thermodynamic properties were quantified including the heat absorption rate, Q_{in}, the effective temperature at which heat is absorbed, $\langle T_{hot} \rangle$, and the effective temperature at which heat is released, $\langle T_{cold} \rangle$. The quantifications of diabatic heating and effective temperatures involve parameters such as the vertical velocity of the air with large uncertainties. Absolute values of these thermodynamic properties are subject to large uncertainties as well. However, in the historical variation of $\langle T_{hot} \rangle$ and $\langle T_{cold} \rangle$, the values of $\langle T_{hot} \rangle$ and $\langle T_{cold} \rangle$ for any particular year were quantified in the same fashion. It is unlikely that the upward trends of $\langle T_{hot} \rangle$ and $\langle T_{cold} \rangle$ can be attributed mainly to the uncertainties in the calculations. A number of studies argued that the warming climate over the past decades has influenced the wind resource potential (e.g. Breslow and Sailor 2002; Pryor et al. 2005; Sailor et al. 2008; Bloom et al. 2008; Pryor and Barthelmie 2010; Mideksa and

Kallbekken 2010; Pereira et al. 2010; Wan et al. 2010). The upward trends in $\langle T_{cold} \rangle$ and $\langle T_{hot} \rangle$ obtained here confirms the fact that the thermodynamic conditions of the atmosphere have undergone a significant change over the past 32 years.

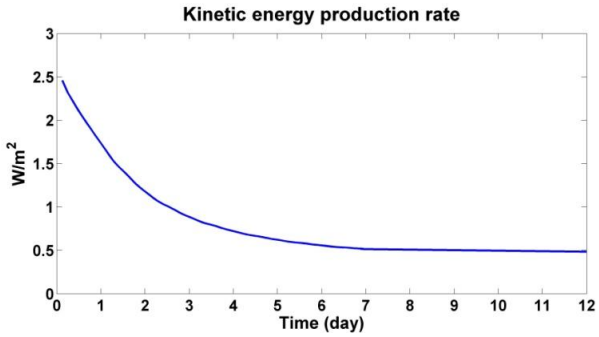

Figure 4.18 Dependence of calculated values for global kinetic energy production rate as a function of the time-resolution employed in averaging input data. The x-axis denotes the temporal period for which the values of v_h and p have been averaged. The y-axis denotes the corresponding global integral of the kinetic energy production rate, C. The highest value of C corresponds to results obtained here using the most highly temporally resolved 3-hour values for v_h and p.

This study employed a number of different approaches to investigate the thermodynamic properties and processes of the atmospheric thermal engine. The origin of the kinetic energy of wind was analyzed retrospectively based on the MERRA data. A key question is whether the conclusions reached in the study may be conditioned by the use of this specific data base. Other datasets including NCEP-1, NCEP-2, ERA-40 and JRA-25 should be employed in the future to compare with the results from this study. With respect to the ultimate global potential for future wind generated electricity, large scale deployment of wind farms can increase positive entropy production by introducing friction and by introducing dissipative turbulence in the boundary

layer, in addition to its role in extracting the kinetic energy harvested to produce electricity. To realistically simulate this thermodynamic process will be challenging, with the background of a changing climate further complicating the analysis. Addressing the ultimate physical limit to wind potential question will require a new generation of studies focusing on the physics of the changing atmospheric environment.

Acknowledgements

The work described here was supported by the National Science Foundation. Junling Huang was also supported by the Harvard Graduate Consortium on Energy and Environment. We acknowledge helpful and constructive comments from Michael J. Aziz, Zhiming Kuang and Xi Lu.

References

Adams, A. S., and D. W. Keith, 2013: Are global wind power resource estimates overstated? *Environ. Res. Lett.*, **8**, 015021.

Archer, C.L., and M. Z. Jacobson, 2005: Evaluation of global wind power. *J. Geophys. Res.*, **110**, D12110.

Archer, C. L., and M. Z. Jacobson, 2013: Geographical and seasonal variability of the global "practical" wind resources. *Applied Geography*, **45**, 119-130.

Bloom, A., V. Kotroni, and K. Lagouvardos, 2008: Climate change impact of wind energy availability in the Eastern Mediterranean using the regional climate model PRECIS. *Natural Hazards and Earth System Science*, **8**, 1249-1257.

Breslow, P. B., and D. J. Sailor, 2002: Vulnerability of wind power resources to climate change in the continental United States. *Renewable Energy*, **27**, 585-598.

de Castro, C., M. Mediavilla, L. J. Miguel, and F. Frechoso, 2011: Global wind power potential: Physical and technological limits. *Energy Policy*, **39**, 6677-6682.

Fitch, A. C., J. B. Olson, J. K. Lundquist, J. Dudhia, A. K. Gupta, J. Michalakes, and I. Barstad, 2012: Local and mesoscale impacts of wind farms as parameterized in a mesoscale NWP model. *Mon. Wea. Rev.*, **140**, 3017-3038.

Fitch, A. C., J. K. Lundquist, and J. B. Olson, 2013: Mesoscale Influences of Wind Farms throughout a Diurnal Cycle. *Mon. Wea. Rev.*, **141**,7.

Fitch, A. C., B. O. Joseph, and K. L. Julie, 2013: Parameterization of Wind Farms in Climate Models. *J. Climate,* **26**, 17.

Gordon, J. M., and Y. Zarmi, 1989: Wind energy as a solar-driven heat engine: a thermodynamic approach. *Am. J. Phys.*, **57**, 11.

Gustavson, M. R., 1979: Limits to wind power utilization. *Science*, **204**, 13-17.

Hagos, S., et al., 2010: Estimates of tropical diabatic heating profiles: Commonalities and uncertainties. *J. Climate*, **23**, 542-558.

Hansen, J., R. Ruedy, M. Sato, and K. Lo, 2010: Global surface temperature change. *Rev. Geophys.*, **48**, RG4004.

Heide, D., L. Von Bremen, M. Greiner, C. Hoffmann, M. Speckmann, and S. Bofinger, 2010: Seasonal optimal mix of wind and solar power in a future, highly renewable Europe. *Renewable Energy*, **35**, 2483-2489.

Hoogwijk, M., B. de Vries, and W. Turkenburg, 2004: Assessment of the global and regional geographical, technical and economic potential of onshore wind energy. *Energy Economics*, **26**, 889-919.

Huang, J., X. Lu, and M. B. McElroy, 2014: Meteorologically defined limits to reduction in the variability of outputs from a coupled wind farm system in the Central US. *Renewable Energy*, **62**, 331-340.

Huang, J., and M. B. McElroy, 2014: Contributions of the Hadley and Ferrel Circulations to the Energetics of the Atmosphere over the past 32-years. *J. Climate*, **27**, 2656–2666.

Jacobson, M. Z., and C. L. Archer, 2012: Saturation wind power potential and its implications for wind energy. *Proc. Natl. Acad. Sci.*, **109**, 15679-15684.

Jiang, Y., Y. Luo, Z. Zhao, and S. Tao, 2010: Changes in wind speed over China during 1956 - 2004. *Theoretical and Applied Climatology*, **99**, 421-430.

Johnson, D. R., 1997: "General coldness of climate models" and the second law: implications for modeling the Earth system. *J. Climate*, **10**, 2826-2846.

Keith, D. W., J. F. DeCarolis, D. C. Denkenberger, D. H. Lenschow, S. L. Malyshev, S. Pacala, and P. J. Rasch, 2004: The influence of large-scale wind power on global climate. *Proc. Natl. Acad. Sci.*, **101**, 16115-16120.

Kim, Y. H., and M. K. Kim, 2013: Examination of the global Lorenz energy cycle using MERRA and NCEP-reanalysis 2. *Climate Dynamics*, 1-15.

Kung, E. C., 1966: Large-scale balance of kinetic energy in the atmosphere. *Mon. Wea. Rev.*, **94**, 627-640.

Landberg, L., et al., 2003: Wind resource estimation -- an overview. *Wind Energy*, **6**, 261-271.

Li, L., A. P. Ingersoll, X. Jiang, D. Feldman, and Y. L. Yung, 2007: Lorenz energy cycle of the global atmosphere based on reanalysis datasets. *Geophys. Res. Lett.*, **16**, L16813.

Ling, J., and C. Zhang, 2013: Diabatic heating profiles in recent global reanalyses. *J. Climate*, **26**, 3307-3325.

Lorenz, E. N., 1955: Available potential energy and the maintenance of the general circulation. *Tellus*, **7**, 157-167.

Lorenz, E.N., 1967: *The natural and theory of the general circulation of the atmosphere*. World Meteorological Organization, 161pp.

Lu, H., and F. Porté-Agel, 2011: Large-eddy simulation of a very large wind farm in a stable atmospheric boundary layer. *Phys. Fluids*, **23**, 065101.

Lu, X., M. B. McElroy, and J. Kiviluoma, 2009: Global potential for wind-generated electricity. *Proc. Natl. Acad. Sci.*, **106**, 10933-10938.

Marques, C. A. F., A. Rocha, and J. Corte-Real, 2010: Comparative energetics of ERA-40, JRA-25 and NCEP-R2 reanalysis, in the wave number domain. *Dynamics of Atmospheres and Oceans*, **50**, 375-399.

Marvel, K., B. Kravitz, and K. Caldeira, 2012: Geophysical limits to global wind power. *Nat. Clim. Change*, **3**, 118-121.

Mideksa, T. K., and S. Kallbekken, 2010: The impact of climate change on the electricity market: A review. *Energy Policy*, **38**, 3579-3585.

Miller, L. M., F. Gans, and A. Kleidon, 2011: Estimating maximum global land surface wind power extractability and associated climatic consequences. *Earth System Dynamics*, **2**, 1-12.

Oort, A. H., 1964: On estimates of the atmospheric energy cycle. *Mon. Wea. Rev.*, **92**, 483-493.

Oort, A.H., and J. J. Yienger, 1996: Observed interannual variability in the Hadley Circulation and its connection to ENSO, *J. Climate*, **9**, 2751–2767.

Peixoto, J. P., and A. H. Oort, 1992: *Physics of climate*. American institute of physics, 520pp.

Peixoto, J. P., A. H. Oort, M. De Almeida, and A. Tomé: 1991: Entropy budget of the atmosphere. *J. Geophys. Res.: Atmos.*, **96**, 10981-10988.

Pereira de Lucena, A. F., A. S. Szklo, R. Schaeffer, and R. M. Dutra, 2010: The vulnerability of wind power to climate change in Brazil. *Renewable Energy*, **35**, 904-912.

Porté-Agel, F., Y. T. Wu, H. Lu, and R. J. Conzemius, 2011: Large-eddy simulation of atmospheric boundary layer flow through wind turbines and wind farms. *Journal of Wind Engineering and Industrial Aerodynamics*, **99**, 154-168.

Pryor, S. C., J. T. Schoof, and R. J. Barthelmie, 2005: Climate change impacts on wind speeds and wind energy density in northern Europe: empirical downscaling of multiple AOGCMs. *Climate Research*, **29**, 183.

Pryor, S. C., and R. J. Barthelmie, 2010: Climate change impacts on wind energy: A review. *Renewable Sustainable Energy Rev.*, **14**, 430-437.

Rienecker, M., et al., 2007: The GEOS-5 data assimilation system—Documentation of versions 5.0.1 and 5.1.0. NASA GSFC, Tech. Rep. Series on Global Modeling and Data Assimilation, NASA/TM-2007-104606, Vol. 27.

Roy, S. B., and J. J. Traiteur, 2010: Impacts of wind farms on surface air temperatures. *Proc. Natl. Acad. Sci.*, **107**, 17899-17904.

Sailor, D. J., M. Smith, and M. Hart, 2008: Climate change implications for wind power resources in the Northwest United States. *Renewable Energy*, **33**, 2393-2406.

Tapiador, F. J., 2009: Assessment of renewable energy potential through satellite data and numerical models. *Energy Environ. Sci.*, **2**, 1142-1161.

The World Wind Energy Association 2011 report. May 2012, Bonn, Germany.

Walsh-Thomas, J. M., G. Cervone, P. Agouris and G. Manca, 2012: Further evidence of impacts of large-scale wind farms on land surface temperature. *Renewable Sustainable Energy Rev.*, **16**, 6432-6437.

Wan, H., X. L. Wang, and V. R. Swail, 2010: Homogenization and trend analysis of Canadian near-surface wind speeds. *J. Climate*, **23**, 1209-1225.

Wang, C., and R. G. Prinn, 2010: Potential climatic impacts and reliability of very large-scale wind farms. *Atmos. Chem. Phys.*, **10**, 2053-2061.

Wang, C., and R. G. Prinn, 2011: Potential climatic impacts and reliability of large-scale offshore wind farms. *Environ. Res. Lett.*, **6**, 025101.

Zhou, Y., P. Luckow, S. J. Smith, and L. Clarke, 2012: Evaluation of global onshore wind energy potential and generation costs. *Environ. Sci. Technol.*, **46**, 7857-7864.

Chapter 5

Contributions of the Hadley and Ferrel Circulations to the Energetics of the Atmosphere over the past 32-years

[Huang, J., and M. B. McElroy, 2014: Contributions of the Hadley and Ferrel Circulations to the Energetics of the Atmosphere over the past 32-years. *J. Climate*, **27**, 2656–2666.]

Abstract

The Hadley system provides an example of a thermally direct circulation, the Ferrel system in contrast an example of a thermally indirect circulation. In this study, the authors develop an approach to investigate the key thermodynamic properties of the Hadley and Ferrel systems, quantifying them using assimilated meteorological data covering the period January 1979 to December 2010. This analysis offers a fresh perspective on the conversion of energy in the atmosphere from diabatic heating to the production of atmospheric kinetic energy. The results indicate that the thermodynamic efficiency of the Hadley system, considered as a heat engine, has been relatively constant over the 32 year period covered by the analysis, averaging 2.6 %. Over the same interval, the power generated by the Hadley regime has risen at an average rate of about 0.54 TW per year, reflecting an increase in energy input to the system consistent with the observed trend in the tropical sea surface temperatures. The Ferrel system acts as a heat pump with a coefficient of performance of 12.1, consuming kinetic energy at an approximate rate of 275 TW, exceeding the power production rate of the Hadley system by 77 TW.

5.1 Introduction

The Lorenz Energy Cycle (Lorenz 1955) provides an instructive approach to a quantitative investigation of the energetics of the atmosphere. The uneven spatial distribution of diabatic heating in the atmosphere results in an increase in available potential energy which is converted consequently to kinetic energy maintaining the circulation of the atmosphere against friction. Grounded on this theory, creation of kinetic energy at the expense of available potential energy can be decomposed into a contribution from the meridional overturning circulation, denoted as C_Z, and a contribution from eddies, denoted as C_E. Several groups (e.g., Krueger et al. 1965; Wiin-Nielsen 1967; Oort 1964; Oort and Peixoto 1974; Oort 1983; Li et al. 2007; Kim and Kim 2013) have sought to analyze the energetics of the atmosphere following this approach. Based on daily reports from the global radiosonde network for the 10-year period from 1963 to 1973, Oort (1983) estimated C_Z and C_E as -0.15W/m^2 and 2.0W/m^2 respectively, revealing the dominant role of C_E relative to C_Z, and concluded that the indirect Ferrel circulation consumes zonal mean kinetic energy at a rate slightly exceeding production by the Hadley circulation. The importance of C_E and C_Z in the conversion of available potential energy to kinetic energy is confirmed by recent studies based on assimilated datasets including NCEP-NCAR, NCEP-R2, ERA40 and MERRA. There are discrepancies, however, in the absolute value and the sign of C_Z (Li, et al. 2007, Kim and Kim 2013). C_Z refers to a composite of three meridional overturning components: the Hadley system in the tropics, the Ferrel system in the mid-latitudes and the Polar system at high latitudes regions. An in-depth understanding of C_Z requires an independent analysis of each component. The Lorenz Energy Cycle has limitations when it comes to defining the role of individual sources in the creation of kinetic energy: it is unable, for example, to isolate the contribution from the Hadley circulation.

The Hadley circulation is identified with rising of warm and moist air in the equatorial region with descent of colder air in the subtropics corresponding to a thermally driven direct circulation, with consequent net production of kinetic energy. Many studies (e.g., Mitas and Clement 2005, 2006; Frierson et al. 2007; Hu and Fu 2007; Lu et al. 2007; Previdi and Liepert 2007; Seidel and Randel 2007; Seidel et al. 2008; Johanson and Fu 2009; Stachnik and Schumacher 2011; Davis and Rosenlof 2012; Nguyen et al. 2013; Hu et al. 2013) have sought to analyze how the Hadley system has varied under the recent warming climate. Results from these investigations indicate expansion and intensification of the Hadley circulation over the past several decades. A related question is whether the Hadley system has became more energetic.

At mid-latitudes, the circulation of the atmosphere is dominated by wave-like flows. The Ferrel cells represent statistical residues that result after zonal averaging of large northward and southward flows associated with the quasi-stationary atmospheric waves. The Ferrel cells are identified with rising motion of relatively cold air at high latitudes, sinking of relatively warm air at the lower mid-latitudes, defining a thermally indirect circulation with consequent consumption of kinetic energy (Peixoto and Oort 1992).

Grotjahn (2003) pointed out that the Carnot Cycle concept can be used to estimate the generation of kinetic energy that results from the thermodynamic changes an air parcel undergoes while completing an atmospheric circuit. He estimated the power of one of the Hadley cells by plotting the thermodynamic properties of air parcels on a temperature - pressure diagram. In this study, we extend his approach, investigating the key thermodynamic properties of the Hadley and Ferrel circulations using assimilated meteorological data from the Modern Era Retrospective-analysis for Research and Applications (MERRA). The analysis allow us to differentiate individual contributions of the Hadley and Ferrel systems to the C_Z process. As will

be shown, the study indicates an upward trend in the power generated by the Hadley system over the past three decades, consistent with view that this system is strengthening.

5.2 Data and Methodology

This investigation is based on meteorological data from the MERRA compilation covering the period January 1979 to December 2010. Wind speeds, air temperature and geopotential heights were obtained on the basis of retrospective analysis of global meteorological data using Version 5.2.0 of the GEOS-5 DAS. We use the standard monthly output available for 42 pressure levels with a horizontal resolution of 1.25 ^{o} latitude × 1.25 ^{o} longitude (Rienecker et al. 2007). The tropical sea surface temperature and ENSO index is from Goddard Institute for Space Studies (Hansen et al. 1999; Hansen et al. 2010).

Stream functions defining the zonal mean circulation were computed using the continuity equation for mass expressed in zonally averaged form:

$$\frac{\partial[\bar{v}]cos\Phi}{Rcos\Phi\partial\Phi} + \frac{\partial[\bar{\omega}]}{\partial P} = 0 \tag{5.1}$$

where $\left[\bar{}\right]$ defines the time and zonal average operator, v the meridional wind speed in units of m·s^{-1}, ω the vertical wind speed in units of Pa·s^{-1}, Φ latitude and P pressure in Pa.

The mass stream function φ is given then by:

$$[\bar{v}] = g\frac{\partial\varphi}{2\pi Rcos\Phi\partial P} \tag{5.2}$$

$$[\bar{\omega}] = -g\frac{\partial\varphi}{2\pi R^2 cos\Phi\partial\Phi} \tag{5.3}$$

We calculated φ using $[\bar{v}]$, while $[\bar{\omega}]$ was computed on the basis of the assimilated meteorological data through horizontal integration of equation (5.2) combined with vertical integration of equation (5.3) beginning at the top of the atmosphere where we assumed $\varphi = 0$.

5.3 Thermodynamic properties of the Hadley system

a. Illustration of a direct thermal circulation

Values for January 2009 mass stream functions (10^9 kg·s^{-1}), computed on the basis of the zonal average of monthly assimilated meteorological data, are presented in Figure 5.1a. Positive values are indicated by warm (red) colors with negative values denoted by cold (blue) colors. The bold black contour illustrates the direction of motion (white arrows) corresponding to the direct thermal circulation of the Hadley regime. Maximum heating in January 2009 occurs south of the equator. The air is less dense as a consequence, rising due to buoyancy, cooling in the process. Reaching the top of the convection cell, the air moves northward, cooling as it radiates more energy than it absorbs before sinking eventually in the northern sub-tropics (Marshall and Plumb 2008). The loop is completed as the air moves back across the equator at the surface.

As an example of how work is produced by completing travel around one loop of the cell, we selected the segment defined by the bold black contour in Figure 5.1a, corresponding to a constant mass stream function value of 70×10^9 kg·s^{-1}. The Pressure-Volume (P-V) diagram for transit of 1 kg of air around this loop is presented in Figure 5.1b. At a given pressure level, while the air parcel is experiencing ascending motion, its specific volume (illustrated by the blue line) is always greater than the specific volume (expressed by the red line) associated with the descending portion of the trajectory. The area inside the loop defines the net work performed by the air parcel as it completes travel along the indicated loop. The net work obtained by

completing one circuit of the loop is given by $\oint P\, dV_s$ where V_s defines the specific volume of the air parcel.

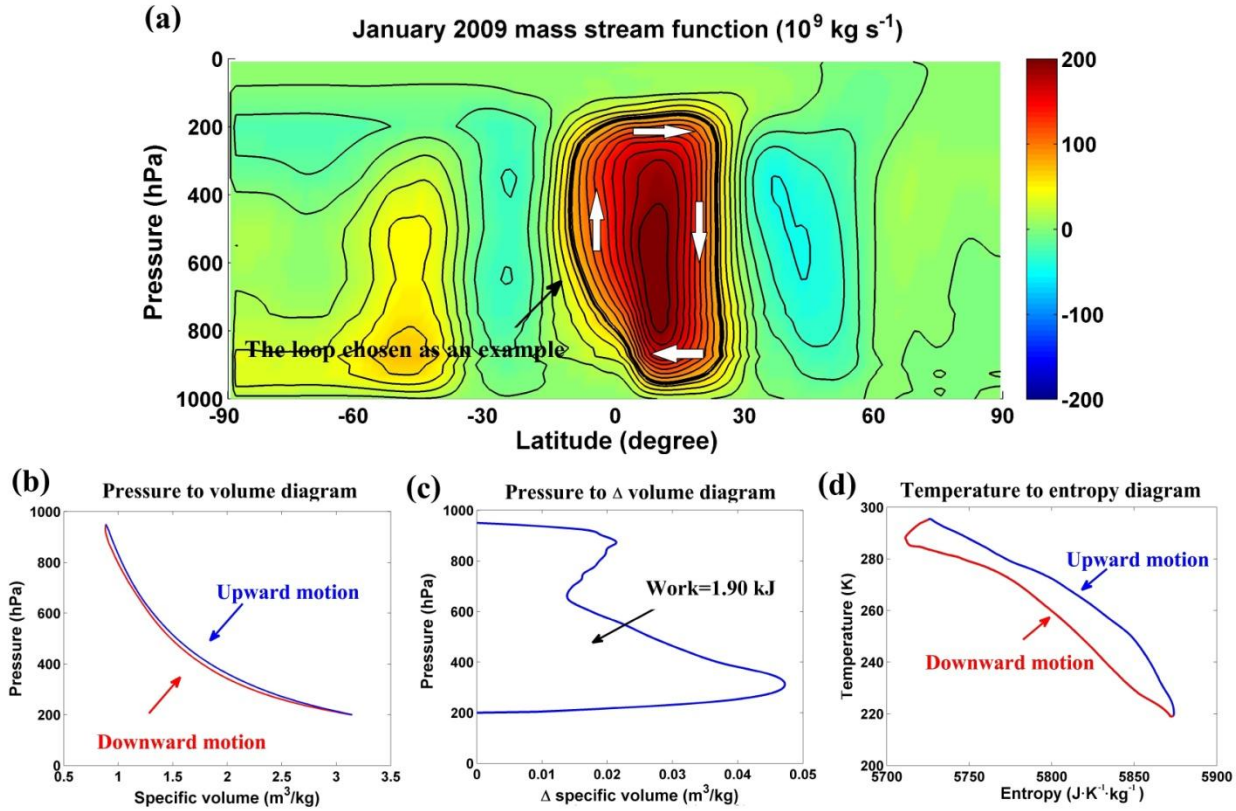

Figure 5.1 The average meridional circulation of the atmosphere in January 2009 with emphasis on the direct Hadley system. Colors in panel (a) specify mass stream function values in units of 10^9 kg s^{-1}. The bold black loop, with constant mass stream-function value of 70×10^9 kg·s^{-1}, is chosen as an example to illustrate the thermally driven direct circulation. White arrows point in the direction of air motion. Panel (b) displays the P-V diagram for an air parcel with mass stream-function value of 70×10^9 kg·s^{-1}. Panel (c) presents the P-ΔV diagram for an air parcel with mass stream-function value of 70×10^9 kg·s^{-1}. Panel (d) illustrates the T-S diagram for an air parcel with mass stream-function value of 70×10^9 kg·s^{-1}.

The net work performed by the air parcel in completing this loop is estimated at 1.90 kJ/kg. The corresponding Pressure-ΔVolume (P-ΔV) diagram is presented in Figure 5.1c in which the vertical axis indicates pressure, with the specific volume change identified on the horizontal axis (at a given pressure level, the specific volume associated the ascending motion minus the specific volume associated with descending motion). The positive sign of ΔV_s in Figure 5.1c implies positive net work. Figure 5.1d presents the temperature-entropy (T-S) diagram for this air parcel, illustrating the changes in temperature and specific entropy that develop over a thermodynamic cycle. The red portion of the temperature-entropy cycle is associated with the downward motion, and located quite close to the blue portion associated with the upward motion, indicating a small thermodynamic efficiency. The thermodynamic efficiency (η) of the loop is defined by:

$$\eta = \frac{\oint T dS}{\int_{absorbed\ heat} T dS} \tag{5.4}$$

where T is temperature, S is entropy and the integral $\int_{absorbed\ heat}$ in the denominator is restricted to portions of the cycle corresponding to net positive heating (namely $T \cdot dS > 0$). The entropy term can be computed as $S = c_p \ln \theta$, where c_p is the specific heat of dry air at constant pressure and θ is potential temperature.

According to the second law of thermodynamics, $dQ = TdS$, where dQ is the net heat contributed by various sources including radiative heating (solar and infrared) and release of latent heat. Thus, the denominator in equation (5.4) calculates the net heat absorbed by the air parcel at higher temperature in order to do mechanical work. Water vapor in the atmosphere acts as a means of storing heat which can be released later. As the air ascends, it may cool and become saturated; then water vapor condenses releasing latent heat. In the case of the tropical

atmosphere, the heat dQ is dominated by the release of latent heat (James, 1995). For the loop considered here, the thermodynamic efficiency is about 4.3 %. Only a small fraction of the heat supplied to the air parcel is converted to mechanical energy.

b. Power of the Hadley system

Consider two loops with constant stream function values, one inside the other (Figure 5.2). Assume that the total mass between loops 1 and 2 is represented by M, while the average time required to complete travel through the region sandwiched between loops 1 and 2 is expressed by t. The mass flux, denoted by F, between loops 1 and 2 is given by the difference between the mass stream function values for loops 1 and 2. The net work associated with travel through one complete loop is defined by $M \cdot \oint PdV_s$, while the time required to travel along the loop is given by $t = \frac{M}{F}$. Thus the power generated by motion of the air sandwiched between loops 1 and 2 is specified by $F \cdot \oint PdV_s$.

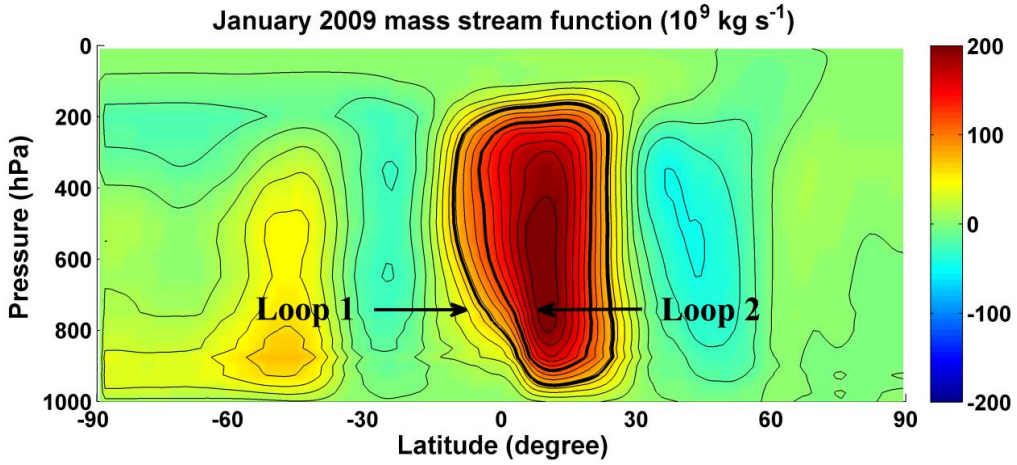

Figure 5.2 Schematic illustration of the method used in quantifying the power of Hadley cells.

For each Hadley cell, the associated power may be calculated according to:

$$Power = \int_{center\ of\ the\ cell}^{edge\ of\ the\ cell} \frac{\partial(Stream\ function\ value)}{\partial \Phi} \cdot \oint PdV \cdot d\Phi \quad (5.5)$$

Based on the assimilated meteorological data adopted here to define conditions over the past 32 years, we calculated the power of the Hadley cells in each hemisphere as well as their combination. The composite (32-year average) monthly results are presented in Figure 5.3a-c. The Hadley cell identified for the Northern Hemisphere refers to the entire cell originating in the Southern Hemisphere extending across the equator to the Northern Hemisphere during northern hemispheric winter. A similar definition applies to the Hadley cell in the Southern Hemisphere. The Hadley cell in the Northern Hemisphere, not surprisingly, reaches its peak power of 218 TW in January with a minimum of 0.5 TW in July. The counterpart in the Southern Hemisphere has a peak of 204 TW in August with a minimum of 32 TW in January. Considering the power associated with the combination of both Hadley cells, there are two peaks, 250 TW in January, 205 TW in August, and two minima, 164 TW in May, 164 TW in October. The annual mean power associated with the overall Hadley system amounts to 198 TW. Reflecting differences in land-sea contrast between the hemispheres, the Hadley cell in the Northern Hemisphere almost disappears during northern summer. Results for the power of the circulation obtained here are smaller than those reported earlier by Grotjahn (2003).

From Figure 5.3 alone, it is unclear which of the terms in Equation (5.5) dominates the annual cycle of Hadley cell power output. Oort and Rasmusson (1970) investigated the annual cycle of the Hadley circulation based on the value of the mass stream function and data for a 5-yr period obtained from a dense network of upper air stations. The seasonality of the Hadley system was explored further by Dima and Wallace (2003) using NCEP-NCAR data covering the period 1979-2001. Defining the seasonality as the principal component of the first EOF mode of

the mass stream function, Dima and Wallace concluded that the seasonal variation of the circulation is sinusoidal. The functional similarity between these results and the seasonal cycle in Figure 5.3 implies that large absolute values of the mass stream function are normally associated with large power output of the Hadley system and vice versa.

The long-term variation of the power contributed by both cells is plotted in Figure 5.3d, covering the period January 1979 to December 2010. The conspicuous intra-seasonal fluctuation in the black line reflects the strong seasonal variation of the Hadley circulation. The red line, computed using a 12-month running average, indicates the existence of an inter-annual variation combined with a longer-term intensification of the circulation. Linear regression of the annual mean average data indicates an increase of 0.54 TW per year in total power since 1979, as defined by the blue line. The associated R^2 for the regression analysis however is 0.31, indicating considerable uncertainty in the magnitude of the inferred trend.

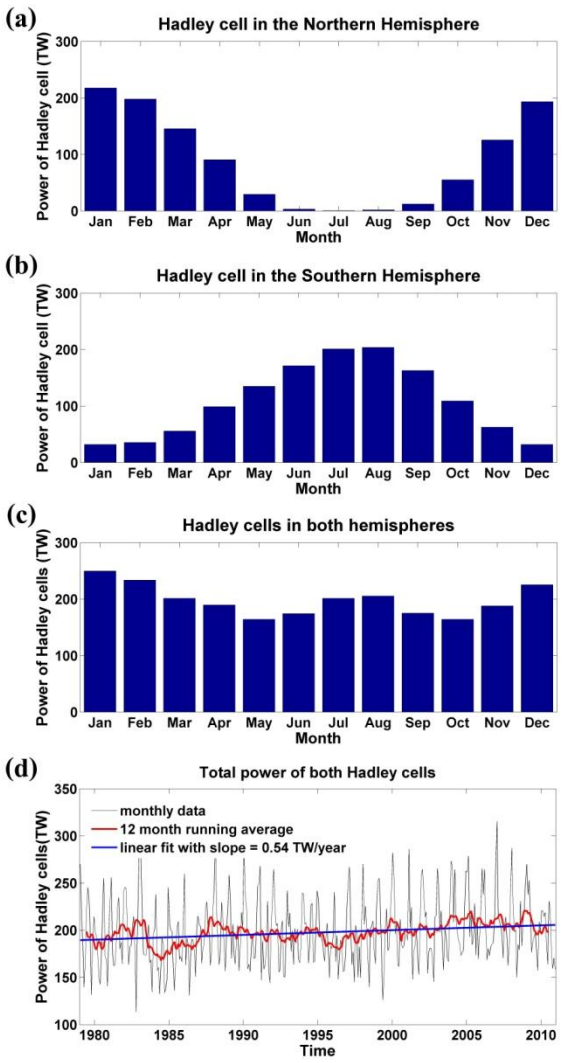

Figure 5.3 The power of the Hadley circulation: (a) The power of the Hadley cell in the Northern Hemisphere as a function of month; (b) The power of the Hadley cell in the Southern Hemisphere as a function of month; (c) The total power of both Hadley cells as a function of month; (d) The variation of the total power of both Hadley cells from January 1979 to December 2010.

c. Thermodynamic efficiency of the Hadley system

The thermodynamic efficiency for the Hadley cell in converting heat to work can be quantified in terms of the ratio of the power generated by the cell with respect to the corresponding rate for net positive absorption of heat. The rate for absorption of heat is given by:

$$absorption\ rate = \int_{center\ of\ the\ cell}^{edge\ of\ the\ cell} \frac{\partial(Stream\ function\ value)}{\partial \Phi} \cdot \int_{absorbed\ heat} T\ dS \cdot d\Phi \qquad (5.6)$$

Results for the thermodynamic efficiency of the Hadley cells in each hemisphere together with the overall efficiency of the entire circulation are displayed as a function of months in Figure 5.4a-c. The Hadley cell in the Northern Hemisphere reaches its highest efficiency of 3.3 % in December with a minimum of less than 0.3 % in July. The counterpart in the Southern Hemisphere has a maximum efficiency of 2.9 % in April with a minimum of 2.3 % in June. The overall efficiency of the entire Hadley system is relatively constant, approximately 2.6 % for each month, with a relatively small associated variation with season. The efficiency calculated for the entire Hadley system is weighted towards the stronger cell; thus the 0.3 % efficiency of the NH cell during July doesn't affect the overall efficiency of the Hadley system, given the fact that the SH cell is exceptionally strong during this month.

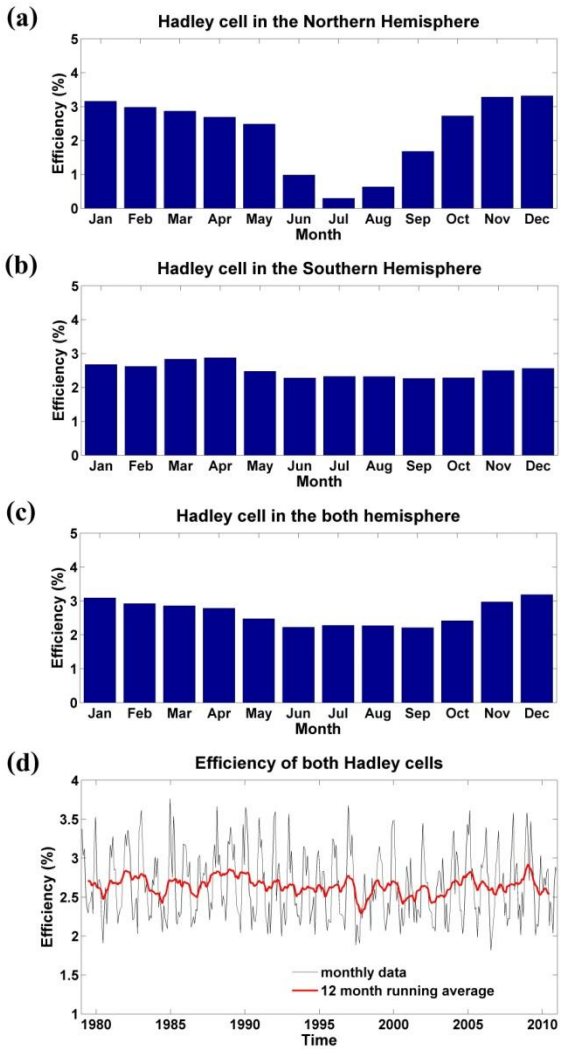

Figure 5.4 The efficiency of the Hadley circulation: (a) The efficiency of the Hadley cell in the Northern Hemisphere as a function of month; (b) The efficiency of the Hadley cell in the Southern Hemisphere as a function of month; (c) The overall efficiency of both Hadley cells as a function of month; (d) The variation of the overall efficiency of both Hadley cells from January 1979 to December 2010.

Although the stream function term dominates, the thermodynamic efficiency plays an important role as well. Reanalysis datasets typically indicate higher values for the overturning stream function value in the Southern Hemisphere as compared to the Northern Hemisphere (Nguyen 2012). However, the Hadley cell in the Northern Hemisphere has a slightly greater peak power with the associated efficiency of 3.2 % as compared with the peak power of the corresponding cell in the Southern Hemisphere with an efficiency of 2.3 %, reflecting the importance of thermodynamic efficiency in determining the generation of power.

The long-term trend for the overall efficiency of the entire Hadley circulation is plotted in Figure 5.4d for the period January 1979 to December 2010. The strong fluctuation in the black line reflects the seasonal variation of the circulation. The red line, computed using a 12-month running average, suggests that, at least on an annually averaged basis, the efficiency has varied little over the 30-year interval covered by the present analysis. Linear regression of the annual mean average over this period provides a regression slope of -0.0029% per year with $R^2 = 0.06$, indicating no statistically significant trend in thermodynamic efficiency.

Monthly values for the heat absorption rates for the Hadley cells in each hemisphere and for the entire Hadley circulation (an average over the entire record covered in this study) are presented in Figure 5.5a-c. The long-term variation of the rate at which the heat is absorbed in driving the entire Hadley circulation is plotted in Figure 5.5d for the period January 1979 to December 2010. The linear regression of the annual mean average data indicates an upward trend with an increase rate of 26.7 TW/yr with $R^2 = 0.55$, as shown by the blue line. The inter-annual variation of the heat absorption rate is associated with variation in tropical sea surface temperature between 23.6 ^{o}S ~ 23.6 ^{o}N (Figure 5.6b): high tropical sea surface temperatures (SSTs) corresponds to high heat absorption rate, and vice versa. The correlation between the 12

month running average of the heat absorption rate and the tropical sea surface temperature shown in Figure 5.6b exceeds 0.6, confirming their strong connection. The ENSO signal is evident also in the heat absorption rate: specifically the warm events in 1983, 1987 and 1997, in addition to the cold events in 1985, 1996 and 1999 (Figure 5.6c). The correlation between the heat absorption rate and the ENSO index shown in Figure 5.6c is less, 0.32, reflecting presumably the fact that the ENSO phenomenon is more localized in the Pacific region rather than distributed over the entire domain of tropical latitudes.

5.4 Thermodynamic properties of the Ferrel system

a. Illustration of an indirect thermal circulation

As with Section 5.3, we begin this section by highlighting one specific zonal mean cell. We choose a specific segment shown in Figure 5.7a, defined by the bold black contour, with a constant mass stream function value of -20×10^9 $kg\cdot s^{-1}$. The P-V diagram for transit of 1 kg around this loop is presented in Figure 5.7b. In contrast to the Hadley circulation, while the air parcel is experiencing ascending motion, its specific volume (illustrated by the blue line) is always smaller than the specific volume (expressed by the red line) associated with the descending portion of the trajectory. The net work consumed by the air parcel in completing this loop is estimated at 3.43 kJ/kg. The corresponding P-ΔV diagram is presented in Figure 5.7c. The T-S cycle in Figure 5.7d is much rounder than that in Figure 5.1d, reflecting the stronger temperature contrast at mid-latitudes, indicating the high efficiency of the Ferrel system in consumption of kinetic energy (Lorenz 1967).

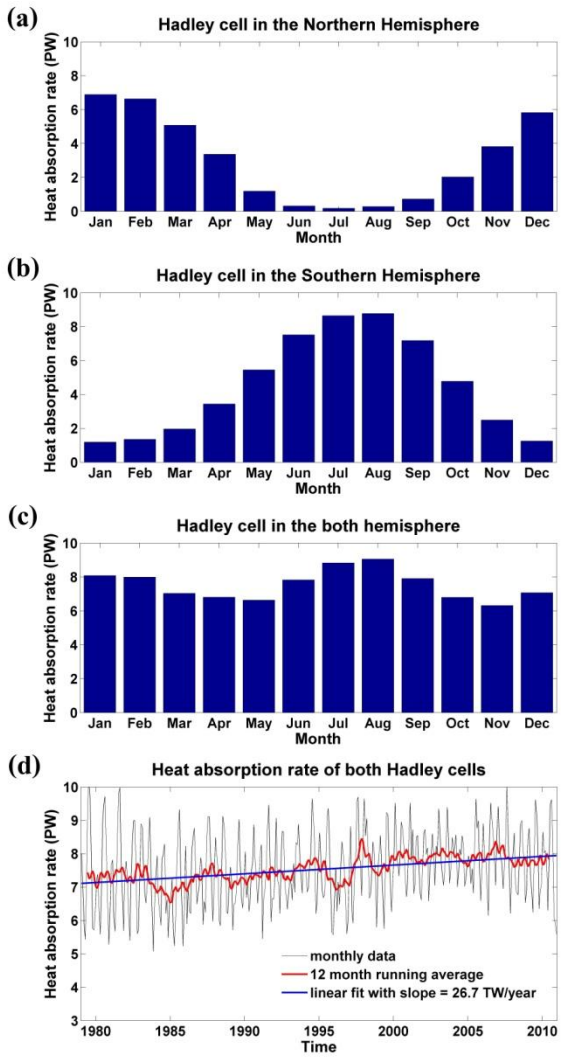

Figure 5.5 The heat absorption rate of the Hadley circulation: (a) The heat absorption rate of the Hadley cell in the Northern Hemisphere as a function of month; (b) The heat absorption rate of the Hadley cell in the Southern Hemisphere as a function of month; (c) The overall heat absorption rate for both Hadley cells as a function of month; (d) The variation of the total heat absorption rate for both Hadley cells from January 1979 to December 2010.

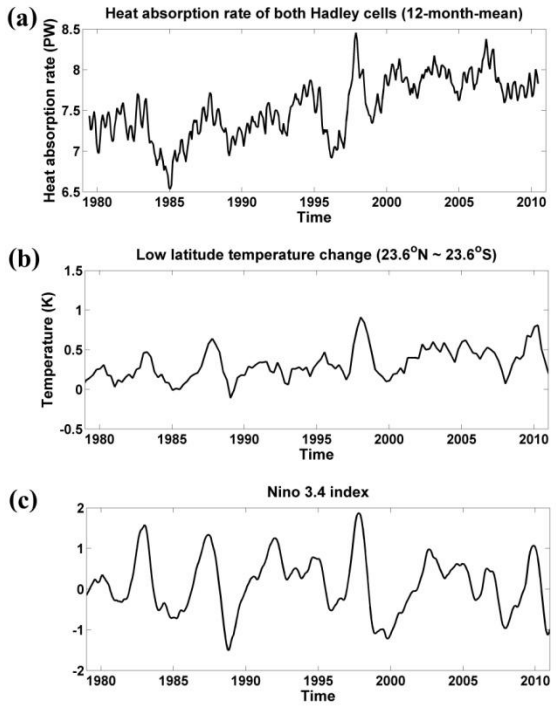

Figure 5.6 Variations of heat absorption rates of both Hadley cells, low latitude temperatures and the Enso index: (a) 12-month running average of the total heat absorption rate for both Hadley cells from January 1979 to December 2010; (b) Changes in mean tropical temperature (data available at: http://data.giss.nasa.gov/gistemp) over the period January 1979 to December 2010; (c) Nino 3.4 index (data available at: http://www.esrl.noaa.gov/psd/data/climateindices) over the period January 1979 to December 2010.

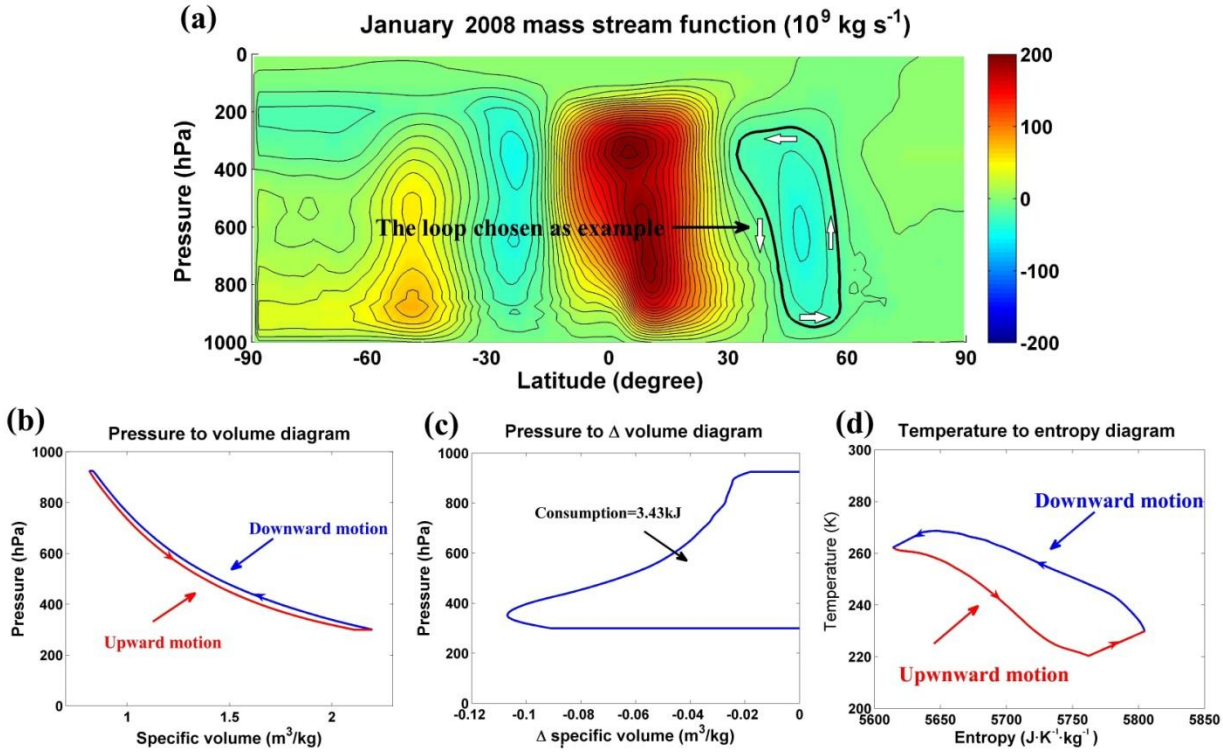

Figure 5.7 The average meridional overturning of the atmosphere in January 2008 with emphasis on the indirect Ferrel circulation. Colors in panel (a) specify mass stream function values in units of 10^9 kg·s^{-1}. The bold black loop, with constant mass stream-function value of -20×10^9 kg·s^{-1}, is chosen as an example to illustrate the thermally driven direct circulation. White arrows point in the direction of air motion. Panel (b) presents the P-V diagram for an air parcel with mass stream-function value of -20×10^9 kg·s^{-1}. Panel (c) displays the P-ΔV diagram for an air parcel with mass stream-function value of -20×10^9 kg·s^{-1}. Panel (d) illustrates the T-S diagram for an air parcel with mass stream-function value of -20×10^9 kg·s^{-1}.

The coefficient of performance (COP) of the loop is defined by:

$$\mathrm{COP} = \frac{\int_{absorbed\ heat} T dS}{\oint T dS} \tag{5.7}$$

where the integral in the denominator is restricted to portions of the cycle corresponding to net positive heating. For the loop considered here, the COP is approximately 13.2. A parcel of air executing such a path illustrates the function of a thermodynamic heat pump. The low latitude Hadley cells act to convert thermal heat to kinetic energy: while the middle latitude Ferrel cells have the opposite effect.

b. The power consumption rate of the Ferrel system

With the same approach used to evaluate the key thermodynamic properties of the Hadley circulation, we calculated the power consumption rate, the COP and heat absorption rate of the Ferrel cells in each hemisphere as well as their combination (Figures 5.8 - 5.10). The annual mean power consumption associated with the overall Ferrel system amounts to 275 TW, consistent with the conclusion reached by Oort (1983) that the Ferrel system consumes kinetic energy at a rate larger than the rate at which power is produced by the Hadley system. The overall COP of the entire Ferrel circulation is relatively constant, approximately 12.1 for each month, with a relatively small associated variation with season. If the Ferrel system were allowed to circulate in the opposite direction as a thermal engine, its efficiency would be 1 / (1+COP) = 7.6% , significantly greater than that of the Hadley system. The average rate at which heat is absorbed from the cold area by the entire Ferrel circulation over the past 32 years amounts to approximately 3.3 PW. Heat is released at the warmer area of the Ferrel system at a rate of (3.3 PW + 275 TW) = 3.6 PW.

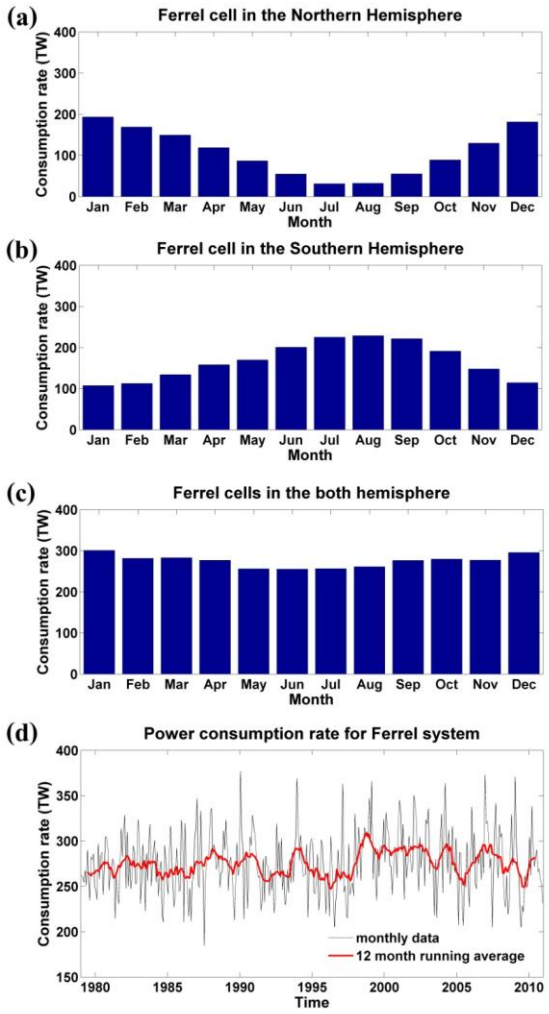

Figure 5.8 The power consumption rate of the Ferrel circulation: (a) The power consumption rate of the Ferrel cell in the Northern Hemisphere as a function of month; (b) The power consumption rate of the Ferrel cell in the Southern Hemisphere as a function of month; (c) The total power consumption rate of both Ferrel cells as a function of month; (d) The variation of the total power consumption rate of both Ferrel cells from January 1979 to December 2010.

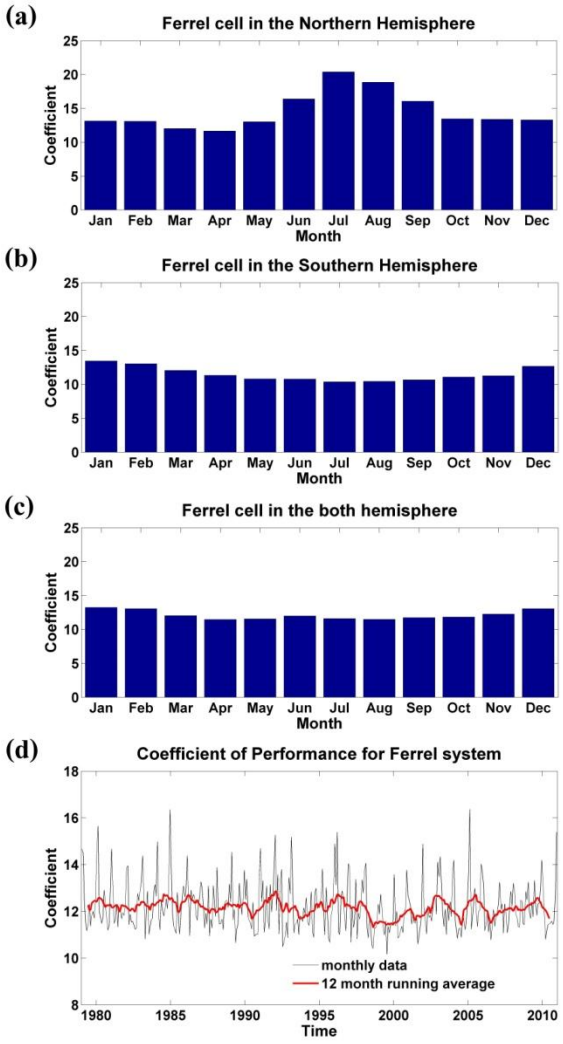

Figure 5.9 The COP of the Ferrel circulation: (a) The COP of the Ferrel cell in the Northern Hemisphere as a function of month; (b) The COP of the Ferrel cell in the Southern Hemisphere as a function of month; (c) The overall COP of both Ferrel cells as a function of month; (d) The variation of the overall COP of both Ferrel cells from January 1979 to December 2010.

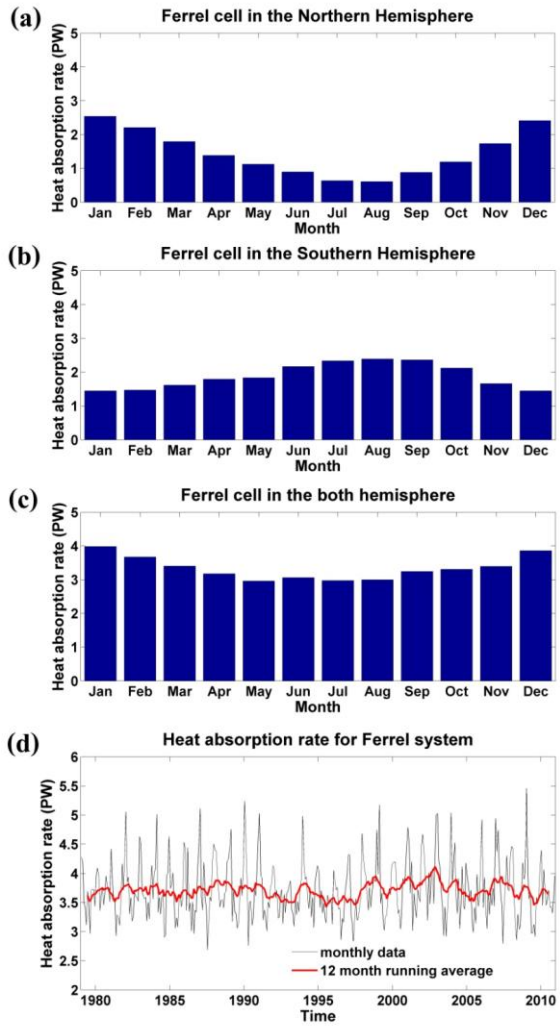

Figure 5.10 The heat absorption rate of the Ferrel circulation: (a) The heat absorption rate of the Ferrel cell in the Northern Hemisphere as a function of month; (b) The heat absorption rate of the Ferrel cell in the Southern Hemisphere as a function of month; (c) The overall heat absorption rate for both Ferrel cells as a function of month; (d) The variation of the total heat absorption rate of both Ferrel cells from January 1979 to December 2010.

5.5 Summary and Discussion

The Hadley, Ferrel and Polar circulations all contribute to the zonal mean kinetic energy budget of the atmosphere as illustrated by Figure 5.11. The present study indicates an upward trend of the power generated by the Hadley circulation over the past 32-year period. The analysis suggests that despite the apparent increase in the heat absorption rate, the thermodynamic efficiency of the Hadley circulation has remained relatively constant. Additional input of heat resulted however in a net increase in work performed and thus an increase in production of kinetic energy. The increase in the heat absorption rate over the period covered in this study amounted to 26.7 TW/year, or 0.1 W/ ($m^2 \cdot$ year) averaged over the equatorial region dominated by the Hadley circulation (30^oS to 30^oN). The positive trend in the heat absorption rate generally follows the positive trend in surface temperatures observed between 23.6 ^oS ~ 23.6 ^oN (Figure 5.6b).

Regarding the energetics of a Hadley cell, we conclude that, in addition to the absolute value of the mass stream function, the thermodynamic efficiency is an important factor in determining the power output. The thermodynamic efficiency is influenced by the profiles of temperature and pressure in the atmosphere. Observational analysis have shown that the Hadley circulation has undergone statistically significant poleward expansion in the past few decades (Hu and Fu, 2007). As the Hadley circulation expanded, the temperature and pressure profiles adjusted accordingly. The present results fail to indicate any statistically significant trend in the thermodynamic efficiency.

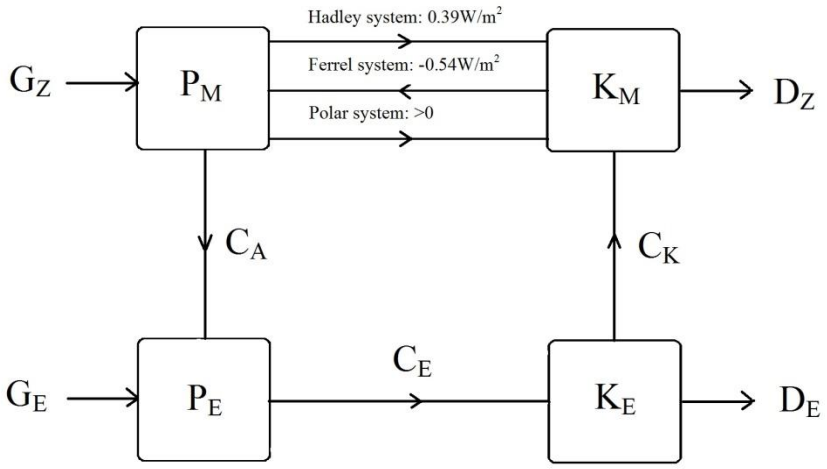

Figure 5.11 Lorenz Energy Cycle with decomposition of the kinetic energy source C_Z. P_M is the mean available potential energy; P_E the eddy available potential energy; K_M the mean kinetic energy; K_E the eddy kinetic energy; G_z the creation of P_M ; G_E the creation of P_E ; C_A the conversion from P_M to P_E ; C_E the conversion from P_E to K_E; C_K the conversion from K_E to K_M; D_z the dissipation of K_M and D_E the dissipation of K_E.

On the intensification of the Hadley circulation, both Mitas and Clement (2005) and Hu et al. (2005) found evidence for intensification of the Hadley circulation in the NCEP/NCAR reanalysis. Since large absolute values of the mass stream function are normally associated with large power output of the Hadley system, the upward trend in the power output of the Hadley system indicated here is in general agreement with the conclusions from previous studies. Mitas and Clement (2006) pointed out that the trend might reflect systematic observational errors. Hu, Zhou, and Liu (2011) argued that the increasing trend in the Hadley circulation strength in ERA-40 might be artificial as well. The MERRA data used in this study were processed in three separate streams. The data distribution adopted here used Stream 1 for 1st January 1979 to 31st December 1992, Stream 2 for 1st January 1993 to 31st December 2000, and Stream 3 for 1st January 2001 to the present. Despite differences in the NCEP/NCAR used in the earlier studies

and the MERRA data employed here, conclusions in both cases are in agreement with respect to the temporal intensification of the Hadley circulation.

The Ferrel circulation is an indirect meridional overturning circulation in mid-latitudes. The rounder shape of T-S cycle in Figure 5.7d as compared to Figure 5.1d confirms Lorenz's 1967 expectation that the stronger horizontal temperature contrast at mid-latitudes should enhance the power consumption ability of the Ferrel system. The analysis implies that there has been no statistically significant trend in the power consumption rate of the Ferrel circulation over the past 32-years.

The contribution of the Hadley and Ferrel circulations in combination have been responsible for net consumption of kinetic energy at an annually averaged rate of 77 TW or $0.15 W/m^2$ over the past 32 years (Figure 5.12). The Polar meridional cell is too weak to allow its contribution to be calculated following the procedure adopted here for the Hadley and Ferrel systems. The Polar circulation is direct, expected therefore to contribute a net source of kinetic energy. Its contribution is unlikely to significantly offset the net sink attributed here to the combination of the Hadley and Ferrel systems.

Kim and Kim (2013) analyzed the Lorenz Energy Cycle using standard daily output of MERRA dataset covering the period 1979 - 2008. Based on two different formulations, they estimated C_Z to be -0.06 or $-0.13 W/m^2$, which is in agreement with results obtained here.

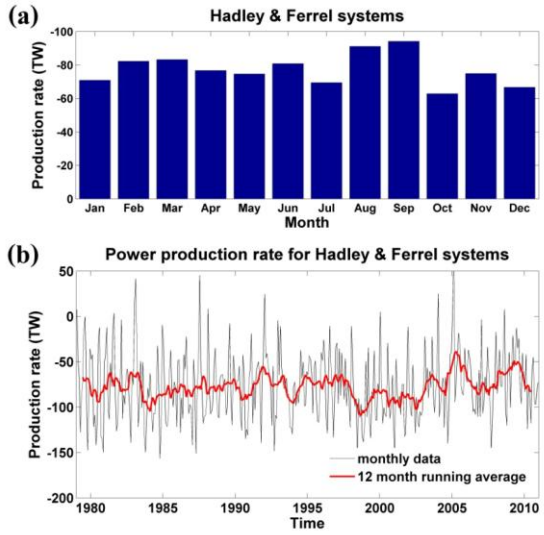

Figure 5.12 The power generated by the combination of Hadley and Ferrel circulations: (a) The power generated by the combination of Hadley and Ferrel circulations as a function of month; (b) The power generated by the combination of Hadley and Ferrel circulations from January 1979 to December 2010.

Peixoto and Oort (1983) pointed out that C_E is the dominant term in the creation of kinetic energy, and simplified the conversion from available potential energy to kinetic energy process as $P_E \rightarrow K_E$, and the zonal mean kinetic energy creation process as $K_E \rightarrow K_M$ (all symbols used here are defined in the caption to Figure 5.11). Thus they concluded that the energy cycle in the atmosphere proceeds from P_M to K_M through the scheme: $P_M \rightarrow P_E \rightarrow K_E \rightarrow K_M$. According to Kim and Kim (2013), C_K ($K_E \rightarrow K_M$ process) and C_E ($P_E \rightarrow K_E$ process) amount to 0.33 W/m^2 and 2.05 W/m^2 respectively, the absolute values of which are comparable to that of the power generated by the Hadley or Ferrel systems. This study provides a more comprehensive picture for P_M to K_M as summarized in Figure 5.11.

Acknowledgements

The work described here was supported by the National Science Foundation. Junling Huang was also supported by the Harvard Graduate Consortium on Energy and Environment. We acknowledge helpful and constructive comments from Brian F. Farrell, Zhiming Kuang, Michael J. Aziz, and Xi Lu. We are indebted also to two anonymous referees for helpful suggestions.

References

Davis, S. M., and K.H. Rosenlof, 2012: A multidiagnostic intercomparison of tropical-width time series using reanalyses and satellite observations. *J. Climate*, **25**, 1061-1078.

Dima, I. M., and J.M. Wallace, 2003: On the seasonality of the Hadley cell. *J. Atmos. Sci.*, **60**, 1522–1527.

Frierson, D. M. W., J. Lu, and G. Chen, 2007: Width of the Hadley cell in simple and comprehensive general circulation models. *Geophys. Res. Lett.*, **34**, L18804

Grotjahn, R., 2003: Energy Cycle. *Encyclopedia of Atmos. Sci.*, 829–841

Hansen, J., R. Ruedy, J. Glascoe, and M. Sato, 1999: GISS analysis of surface temperature change. *J. Geophys. Res.*, **104**, 30997-31022.

Hansen, J., R. Ruedy, M. Sato, and K. Lo, 2010: Global surface temperature change. *Rev. Geophys.*, **48**, RG4004

Hu, Y., K.K. Tung, and J. Liu, 2005: A closer comparison of early and late-winter atmospheric trends in the northern hemisphere. *J. Climate*, **18**, 3204-3216.

Hu, Y., and Q. Fu, 2007: Observed poleward expansion of the Hadley circulation since 1979, *Atmos. Chem. Phys.*, **7**, 5229–5236.

Hu, Y., C. Zhou, and J. Liu, 2011: Observational evidence for poleward expansion of the Hadley circulation. *Adv. Atmos. Sci.*, **28**, 33-44.

Hu, Y., L. Tao, and J. Liu, 2013: Poleward expansion of the Hadley circulation in CMIP5 simulations. *Adv. Atmos. Sci.*, **30**, 790-795.

James, I. N., 1995: *Introduction to circulating atmospheres*. Cambridge University Press, 74 pp.

Johanson, C. M., and Q. Fu, 2009: Hadley cell widening: Model simulations versus observations. *J. Climate*, **22**, 2713–2725.

Kim, Y. H., and M. K. Kim, 2013: Examination of the global lorenz energy cycle using MERRA and NCEP-reanalysis 2. *Climate Dynamics*, 1-15.

Krueger, A. F., J. S. Winston, and D. A. Haines, 1965: Computation of atmospheric energy and its transformation for the Northern Hemisphere for a recent five-year period. *Mon. Wea. Rev.*, **93**, 227– 238.

Li, L., A. P. Ingersoll, X. Jiang, D. Feldman, and Y. L. Yung, 2007: Lorenz energy cycle of the global atmosphere based on reanalysis datasets. *Geophys. Res. Lett.*, **34**, L16813.

Lorenz, E. N., 1955: Available potential energy and the maintenance of the general circulation. *Tellus*, **7**, 157-167.

----------, 1967: *The natural and theory of the general circulation of the atmosphere*. World Meteorological Organization, 109 pp.

Lu, J., G.A. Vecchi and T. Reichler, 2007: Expansion of the Hadley cell under global warming. *Geophys. Res. Lett.*, **34**, L06805.

Marshall, J., and R. A. Plumb, 2008: *Atmosphere, ocean, and climate dynamics: an introductory text*. Academic Press, 74 pp.

Mitas, C. M., and A. Clement, 2005: Has the Hadley cell been strengthening in recent decades? *Geophys. Res. Lett.*, **32**, L03809.

Mitas, C. M., and A. Clement, 2006: Recent behavior of the Hadley cell and tropical thermodynamics in climate models and reanalyses. *Geophys. Res. Lett.*, **33**, L01810.

Nguyen, H., A. Evans, C. Lucas, I. Smith, and B. Timbal, 2013: The Hadley Circulation in Reanalyses: Climatology, Variability, and Change. *J. Climate*, **26**, 3357-3376.

Oort, A. H., 1964: On estimates of the atmospheric energy cycle. *Mon. Wea. Rev.*, **92**, 483-493.

----------, 1983: Global atmospheric circulation statistics, 1958– 1973 (No. 14). NOAA, U.S. Gov. Print. Off., 180 - 226.

Oort, A. H., and E. M. Rasmusson, 1970: On the annual variation of the monthly mean meridional circulation. *Mon. Wea. Rev.*, **98**, 423-442.

Oort, A. H., and J. P. Peixóto, 1974: The annual cycle of the energetics of the atmosphere on a planetary scale. J. Geophys. Res., **79**, 2705-2719.

Peixoto, J. P., and A. H. Oort, 1992: *Physics of Climate*. AIP Press, 160 pp.

Previdi, M., and B. G. Liepert, 2007: Annular modes and Hadley cell expansion under global warming. *Geophys. Res. Lett.*, **34**, L22701.

Rienecker, M. et al., 2007: The GEOS-5 data assimilation system—Documentation of versions 5.0.1 and 5.1.0. NASA GSFC, Tech. Rep. Series on Global Modeling and Data Assimilation, NASA/TM-2007-104606, Vol. 27.

Seidel, D. J., and W. J. Randel, 2007: Recent widening of the tropical belt: Evidence from tropopause observations. *J. Geophys. Res.*, **112**, D20113.

Seidel, D. J., Q. Fu, W. J. Randel, and T. J. Reichler, 2008: Widening of the tropical belt in a changing climate. *Nature Geosci.*, **1**, 21–24.

Stachnik, J. P., and C. Schumacher, 2011: A comparison of the Hadley circulation in modern reanalyses. *J. Geophys. Res.*, **116**, D22102.

Wiin-Nielsen, A., 1967: On the annual variation and spectral distribution of atmospheric energy. *Tellus*, **19**, 540–559.

Chapter 6

Thermodynamic Instability of the global Atmosphere in the Context of recent Changes in global Climate

Abstract

The atmosphere is an example of non-equilibrium system. This study presents an approach to investigate the relationship among temperature, energy and entropy of the atmosphere, introducing two variables that serve to quantify the thermodynamic instability of the atmosphere. The maximum work, W_{max}, that the atmosphere can perform may be defined as the work developed through a thermally reversible and adiabatic process to thermodynamic equilibrium with global entropy conserved. The maximum entropy increase, $(\Delta S)_{max}$, may be defined as the increase in global entropy achieved through a thermally irreversible process to thermodynamic equilibrium without performing any work. W_{max} is identified as an approximately linear function of $(\Delta S)_{max}$. Large values of W_{max} or $(\Delta S)_{max}$ correspond to high thermodynamic instability. The seasonality and long-term historical variation of the W_{max} and $(\Delta S)_{max}$ were computed, indicating maximum instability in July, minimum instability in January with no statistically significant trend over the past 32 years. The magnitude of the seasonal cycles of W_{max} is roughly 4 times larger than that of the available potential energy introduced by Lorenz, indicating that the Lorenz Energy Cycle theory which emphasizes on the mechanical instability of the atmosphere may explain only a portion of the energetics of the atmosphere.

6.1 Introduction

Most phenomena occurring in the atmosphere are characterized by thermodynamic irreversibility and evolve in time with increases in entropy. The circulation is maintained by the instability of the atmospheric system, and this question have been studied from a variety of different perspectives. Lorenz (1955) established the Lorenz Energy Cycle (LEC) theory explaining the energetics of atmosphere mainly from a mechanical perspective with kinetic energy produced at the expense of available potential energy (APE), a measure of the instability of the atmosphere. A number of other groups sought to answer the question from a thermodynamic perspective focusing on the budget of atmospheric entropy (e.g. Wulf and Davis 1952; Dutton 1973; Paltridge 1975; Peixoto et al. 1991; Goody and Abdou 1996; Goody 2000; Paltridge 2001; Pauluis and Held 2002a, 200b; Ozawa 2003; Romps 2008; Lucarini et al. 2011; Bannon 2012; Huang and McElroy 2014).

Lorenz (1955) defines the APE as the difference in total static energy (internal thermal plus potential) between the current state of the dry air component of the atmosphere and that of an idealized reference state, defined as the state that minimizes the static energy of the dry air component of the atmosphere after a sequence of reversible isentropic and adiabatic transformations with air parcels conserving their potential temperature, θ. The reference state is characterized by horizontal stratification with absolute stability in pressure, potential temperature and height.

For an isentropic and adiabatic adjustment of the mass field, the surface of constant θ behaves as a material surface. Thus, the average pressure over an isentropic surface, $\tilde{p}(\theta)$, can be quantified based on the relation:

$$\tilde{p}(\theta) = \iint_{\sigma} p(x, y, \theta) \cdot dxdy \; / \; \iint_{\sigma} dxdy \tag{6.1}$$

where σ is the global area defined by a constant θ surface and $p(x, y, \theta)$ is air pressure in an (x, y, θ) coordinate system. When a constant θ surface intersects the earth's surface ($\theta \leq \theta_{surface}$), $p(\theta)$ is set equal to $p_{surface}$. During an isentropic and adiabatic rearrangement of mass, $\tilde{p}(\theta)$ is conserved, representing thus the pressure of the reference state. APE is defined as

$$APE = \int (\Phi + \mathrm{I}) \cdot \mathrm{dm} - \int (\Phi_{\mathrm{r}} + \mathrm{I}_{\mathrm{r}}) \cdot \mathrm{dm} \tag{6.2}$$

where Φ and Φ_{r} represent the potential energy and the corresponding reference state of the atmosphere respectively, and I and I_{r} denote the internal energy and the internal energy for the corresponding reference state (Peixoto and Oort, 1992). Besides providing an approach to quantify APE, Lorenz also established the LEC theory accounting for production and dissipation of APE as the mechanism responsible for maintaining the circulation of the atmosphere.

Figure 6.1 presents a schematic illustration of APE, computed based on assimilated meteorological data from the Modern Era Retrospective-analysis for Research and Applications (MERRA). The upper panels display the zonal-average potential temperature, θ, and the zonal-average temperature, T, for year 2008. The lower panels present the zonal-average potential temperature, θ, and the zonal-average temperature, T, for the associated reference state, computed based on equation (6.1). According to the LEC theory, the maximum production of kinetic energy corresponds to the expenditure of all of the APE when the structure of θ on the upper panel collapses to the structure depicted on the lower panel. The structure of θ in the

reference state (lower panels in Figure 6.1) defines the condition of absolute mechanical equilibrium, since the horizontal pressure force has been eliminated and since the vertical pressure force is balanced by gravity.

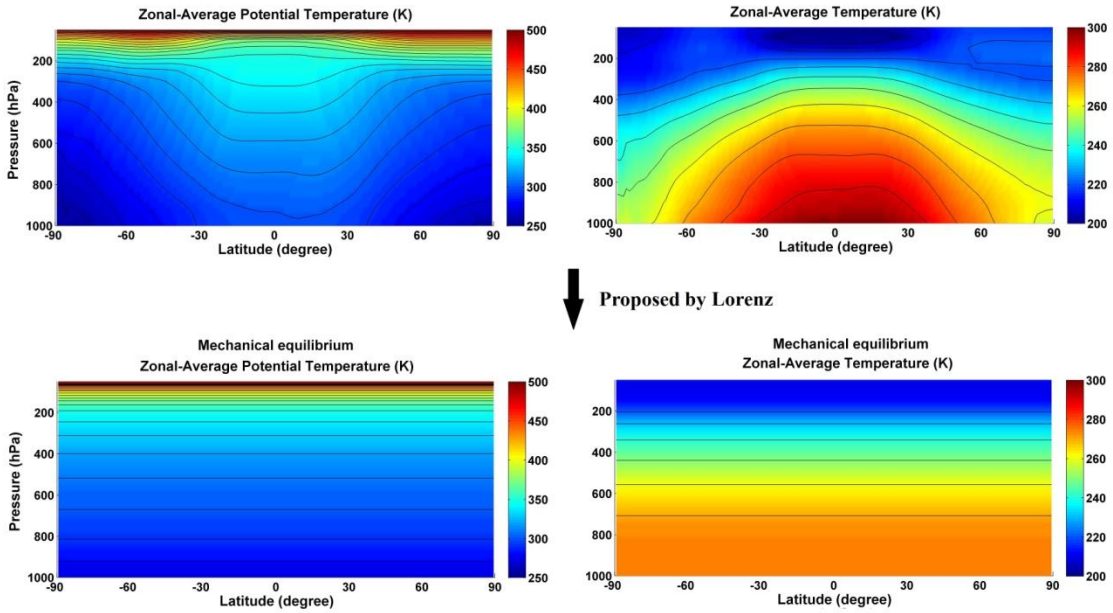

Figure 6.1 Schematic illustration of APE. The upper panels present zonal-average potential temperatures, θ, and zonal-average temperatures, T, for year 2008. The lower panels indicate zonal-average potential temperatures, θ, and zonal-average temperatures, T, for the associated reference state proposed by Lorenz again for year 2008.

A number of groups have investigated the APE of the atmosphere based on the LEC theory (e.g. Oort 1964; Oort and Yienger 1996; Li et al. 2007; Boer and Lambert 2008; Hernández-Deckers and Storch 2010; Marques et al. 2009; Becker, E., 2009; Marques et al. 2010; Marques et al. 2011; Kim and Kim 2013). For example, using MERRA data, Kim and Kim (2013) estimated the global averaged APE as 4.34 MJ/m^2 on an annual mean, 4.02 MJ/m^2 for the June ~ August (JJA) mean and 4.75 MJ/m^2 for the December ~ February (DJF) mean.

The reference state defined by Lorenz, although in mechanical equilibrium, is not in thermal equilibrium. The zonal-average temperature, T, for the associated reference state in Figure 6.1 indicates the existence of a vertical temperature gradient. The reference state has the potential to produce additional kinetic energy through a thermodynamically reversible process. According to the second law of thermodynamics, motions of the atmosphere should drive the system towards thermodynamic equilibrium. A thermodynamic equilibrium state requires both mechanical and thermal equilibrium. Figure 6.2 presents a schematic illustration of an approach to thermodynamic equilibrium. The lower panels in Figure 6.2 display the zonal-average potential temperature, θ, and zonal-average temperature, T, appropriate for a thermodynamic equilibrium state with the equilibrium temperature, T_{eq}, set equal to $249K$. When the atmosphere reaches thermodynamic equilibrium, it is completely divested of any potential to produce kinetic energy.

With respect to entropy, the atmosphere is an open system that exchanges energy and matter with its surroundings. According to Prigogine (1962) and De Groot and Mazur (2013), the total variation of the entropy of the atmosphere, dS^{atm}/dt, consists of two components: the transfer of entropy across the boundary, dS_e^{atm}/dt, and the entropy produced within the system, dS_i^{atm}/dt (Figure 6.3). Most of the phenomena operational in the atmosphere, such as the frictional dissipation of kinetic energy, are thermodynamically irreversible. Thus dS_i^{atm}/dt is always greater than zero. dS^{atm}/dt can be expressed as:

$$\frac{dS^{atm}}{dt} = \frac{dS_e^{atm}}{dt} + \frac{dS_i^{atm}}{dt} \qquad \frac{dS_i^{atm}}{dt} > 0 \tag{6.3}$$

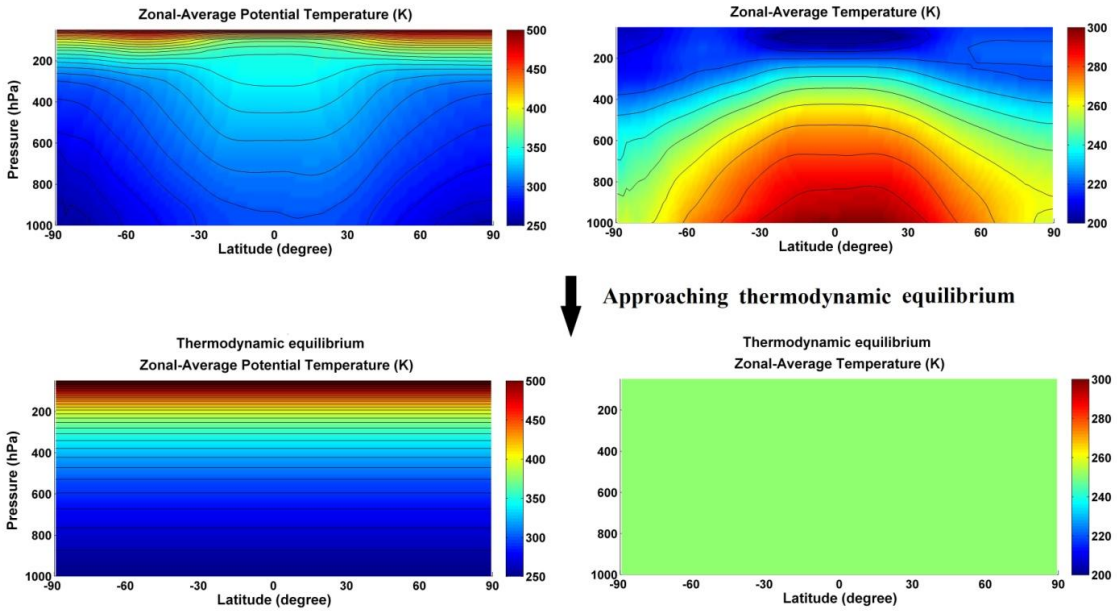

Figure 6.2 Schematic illustration of the approach to thermodynamic equilibrium. The upper panels display zonal-average potential temperatures, θ, and zonal-average temperatures, T, for year 2008. The lower panels indicate zonal-average potential temperatures, θ, and zonal-average temperatures, T, for the thermodynamic equilibrium state.

Peixoto et al. (1991) provided a comprehensive analysis of the contributions to dS_i^{atm}/dt and dS_e^{atm}/dt. A relevant question is: if, since time t_0 the atmosphere had become an isolated system with zero exchange of energy and matter exchange with its environment ($dS^{atm} = dS_i^{atm}$), how much greater would be the eventual increase in entropy, $\int_{t_0}^{\infty} \frac{dS^{atm}}{dt} \cdot dt$, when the atmosphere has reached thermodynamic equilibrium. Similar to APE, $\int_{t_0}^{\infty} \frac{dS^{atm}}{dt} \cdot dt$ also reflects the instability of the atmosphere, but from a thermodynamic perspective.

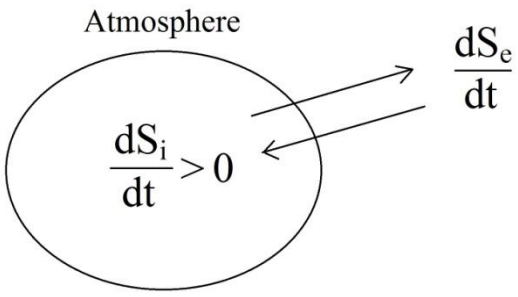

Figure 6.3 Schematic diagram indicating the transfer of entropy across the boundaries and the production of entropy within the atmosphere.

Landau and Lifshitz (1980) described an approach to study the thermodynamic instability problem and to quantify the maximum work, W_{max}, and maximum entropy increase, $(\Delta S)_{max}$, that a conceptual isolated system can perform or achieve. Both variables represent the thermodynamic instability of a conceptual system. In this study, we extend and apply their approach to study the atmosphere, investigating its thermodynamic instability under the context of global warming using assimilated meteorological data from MERRA. The analysis provides a fresh perspective on the relationship among temperature, energy and entropy of the atmosphere and allows us to quantitatively investigate the deviation of the atmosphere from thermodynamic equilibrium.

6.2 Data

The study is based on meteorological data from the MERRA compilation covering the period January 1979 to December 2010. Air temperatures and geopotential heights were obtained on the basis of retrospective analysis of global meteorological data using Version 5.2.0 of the GEOS-5 DAS. We use the standard 3-hourly output available for 42 pressure levels with a horizontal resolution of 1.25 ^{o} latitude × 1.25 ^{o} longitude (Rienecker 2007). The global surface

temperature anomalies employed in this study are from the Goddard Institute for Space Studies (GISS) (Hansen et al. 2010).

6.3 Maximum work and maximum entropy increase problem

For a thermally isolated system consisting of several components out of thermal equilibrium, while equilibrium is being established the system can perform mechanical work on the external medium. The transition to equilibrium may follow a variety of possible paths. The final equilibrium states of the system represented by its energy and entropy may differ as a consequence. The total work that can be performed as well as the entropy increase that may occur from the evolution of a non-equilibrium system will depend on the manner in which equilibrium is established. Here, there are two extreme paths to thermal equilibrium: one consistent with performance of maximum work, W_{max}; the other appropriate for a maximum increase in entropy, $(\Delta S)_{max}$.

The system performs W_{max} when the process of reaching thermal equilibrium is reversible. Figure 6.4 provides the simplest case with the thermally isolated system consisting of only two bodies. When the hot component at temperature T_{hot} loses an amount of energy $Q_h = T_{hot}\delta S_{hot}$, where δS_h is the decrease in entropy for the hot component, the cold component at temperature T_{cold} gains energy $Q_c = T_{cold}\delta S_c$, where δS_c is the entropy increase for the cold component. If the process is reversible, then $\delta S_c + \delta S_h = 0$ and the work produced in the process is equal to $Q_h - Q_c$. As the reversible process continues, T_{hot} and T_{cold} converge to an equilibrium temperature T_{eq}^{S}, with the superscript " ^{S} " denoting zero entropy change, and the thermally isolated system reaches thermal equilibrium with work output of W_{max}. In this study, the transition to thermal equilibrium with W_{max} is identified as Evolution 1.

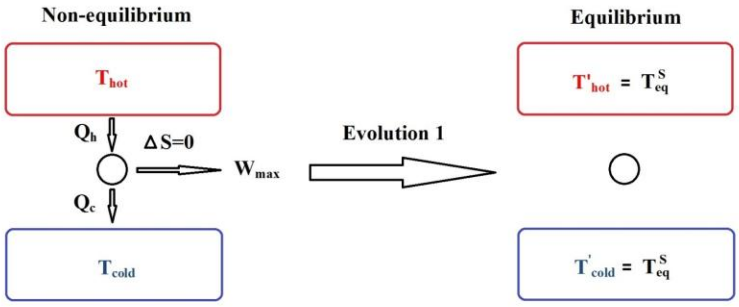

Figure 6.4 Illustration of W_{max} produced from a non-equilibrium system. Initially, the thermally isolated system is out of equilibrium and can perform a maximum of mechanical work through reversible processes ($\Delta S = 0$). Finally, the system reaches equilibrium at T_{eq}^{S} in which the temperature contrast between its subcomponents has been eliminated.

The system achieves $(\Delta S)_{max}$ when the process of reaching thermal equilibrium is totally irreversible and the internal energy remains constant. Figure 6.5 provides the simplest case for this with energy transfer, Q, occurring directly between the components without performing any work. The process is thermally irreversible, and the entropy of the combination of the two components increases by $Q(1/T_{cold} - 1/T_{hot})$. As the energy transfer continues, T_{hot} and T_{cold} converge to another equilibrium temperature T_{eq}^{W}, with the superscript "^{W}" representing the condition where no work is performed and the subscript "$_{eq}$" representing equilibrium. T_{eq}^{W} is greater than T_{eq}^{S}, since zero work is performed on the external medium. Maximum increase in entropy, $(\Delta S)_{max}$, of the entire system occurs in the end. In this study, the transition to thermal equilibrium with $(\Delta S)_{max}$ is indicated as Evolution 2.

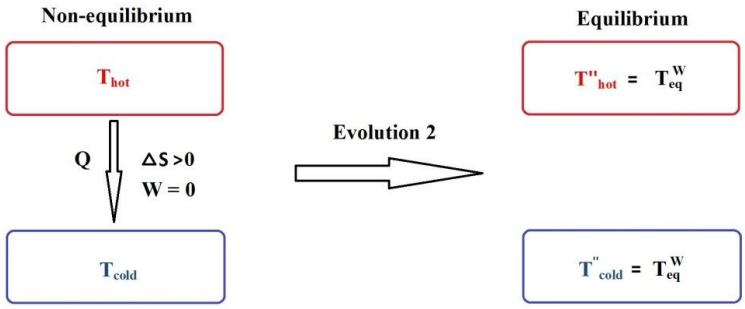

Figure 6.5 Illustration of $(\Delta S)_{max}$ for the entire non-equilibrium system. Initially, the thermally isolated system is energetic and out of equilibrium. There is a flux of energy Q from the high temperature component at T_{hot} to the low temperature component at T_{cold}. As heat transfer continues, the system reaches thermal equilibrium at T_{eq}^{W} in which the temperature contrast between its subcomponents has been eliminated.

The maximum work and maximum entropy increase can be depicted in an Entropy-Energy Diagram. If a system is in thermal equilibrium, its entropy, S_{eq}, and temperature, T_{eq}, are functions of its total energy, E_{eq}: namely $S_{eq} = S_{eq}(E_{eq})$ and $T_{eq} = T_{eq}(E_{eq})$. In Figure 6.6 the continuous line defines the behavior of the function $S_{eq}(E_{eq})$ in an Entropy-Energy Diagram. For a non-equilibrium system with thermal condition (E, S) corresponding to point b in Figure 6.6, the horizontal segment ΔE represents the work performed as the system approaches equilibrium through Evolution 1 while the vertical segment ΔS illustrates the increase in entropy associated with Evolution 2. Consequently $T_{eq}(E_{eq})$ at point a corresponds to T_{eq}^{W}, and $T_{eq}(E_{eq})$ at point b corresponds to T_{eq}^{S}. The maximum work, W_{max}, and the maximum entropy increase, $(\Delta S)_{max}$, reflect the magnitude of the thermodynamic instability of a non-equilibrium system: if the isolated system is moved further from equilibrium, W_{max} and $(\Delta S)_{max}$ are increased; and vice-versa.

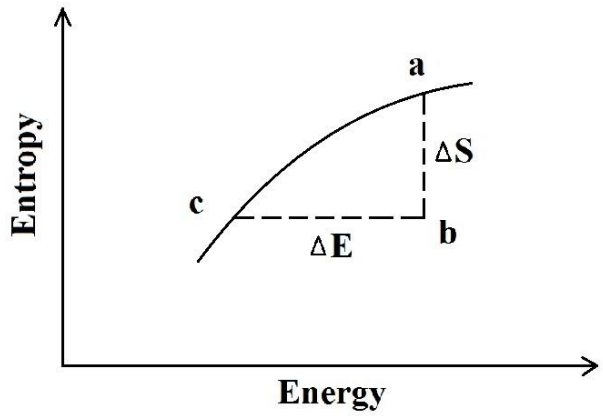

Figure 6.6 Schematic illustration of the evolution of maximum work and maximum entropy increase in an Entropy-Energy Diagram.

6.4 Ideal gas in a gravitational field

In a uniform gravitational field with height represented by z, the potential energy, u, of a molecule is given by $u = mgz$, where m is the mass of a molecule and g is the gravitational acceleration. The distribution of density for a system consisting of an ideal gas at thermodynamic equilibrium is given by the barometric formula:

$$\rho(\vec{r}) = \rho_0 e^{-mgz/(k_B \cdot T_{eq})} \tag{6.4}$$

where ρ_0 is the mass density at level $z = 0$, T_{eq} is the equilibrium temperature and k_B is Boltzmann constant. The pressure in equilibrium, P_{eq}, at height z is given by:

$$P_{eq}(z) = \int_z^{\infty} \rho_0 e^{-mgh/(k_B T_{eq})}\, g \cdot dh \tag{6.5}$$

or

$$P_{eq}(z) = P_0 e^{-mgz/(k_B \cdot T_{eq})} \tag{6.6}$$

where P_0 is the pressure at level $z = 0$.

For a single mole of ideal gas, the associated entropy, S_m, is given by:

$$S_m = C_{p,m} \ln T - R \ln p + S_{m0} \tag{6.7}$$

where $C_{p,m}$ is the molar heat capacity at constant pressure, R is the gas constant, T is the temperature of the gas, p is the pressure and S_{m0} is a constant of integration. Thus, the total entropy of the system is defined by:

$$S = \int \left(C_{p,m} \ln T - R \ln p + S_{m0} \right) \cdot dn \tag{6.8}$$

and the total static energy (internal plus potential), E, is given by:

$$E = \int C_{v,m} T \cdot dn + \int \rho g z \cdot dv \tag{6.9}$$

where n is the number of moles, v is volume and $C_{v,m}$ is the molar heat capacity at constant volume.

If the initial density distribution of a system departs from equation (6.4), the system consisting of the ideal gas will not be in equilibrium. It can approach equilibrium through a number of paths including evolution 1 depicted in Figure 6.4 and evolution 2 depicted in Figure 6.5 Consequently, maximum work, W_{max}, is produced by the system if the transition to equilibrium at temperature T_{eq}^S is reversible (evolution 1 in Figure 6.4), namely $\Delta S = 0$. The maximum work, W_{max}, is equal to ΔE, according to the first law of thermodynamics. W_{max} may be expressed as:

$$W_{max} = \int C_{v,m} \left(T - T_{eq}^S \right) \cdot dn + \int \left(\rho - \rho_{eq}^S \right) g z \cdot dv \tag{6.10}$$

where $\rho_{eq}^S(z) = \rho_0^S e^{-mgz/(k_B \cdot T_{eq}^S)}$. Reflecting the principle of mass conservation, $\int \rho_{eq}^S \cdot dv = \int \rho \cdot dv$, or equivalently, $\rho_0^S = (\int \rho \cdot dv) / \left(\int e^{-mgz/(k_B \cdot T_{eq}^S)} \cdot dv \right)$.

Similarly, the system achieves maximum entropy increase if the transition to equilibrium at temperature T_{eq}^{W} is thermally irreversible and produces no work (evolution 2 in Figure 6.5), $\Delta E = 0$. And the maximum entropy increase may be expressed as:

$$(\Delta S)_{max} = \int \left[C_{p,m} \left(\ln T_{eq}^{W} - \ln T \right) - R \left(\ln P_{eq}^{W}(z) - \ln p \right) \right] \cdot dn \qquad (6.11)$$

where $P_{eq}^{W}(z) = P_0^{W} e^{-mgz/(k_B \cdot T_{eq}^{W})}$. Because of the principle of mass conservation, $\iint_{surface} P_{eq}^{W}(z) \cdot dxdy = \iint_{surface} P \cdot dxdy$.

6.5 A thermodynamic perspective on the atmosphere

Oxygen (O_2) occupies 20.95% by volume of dry air in the atmosphere. Nitrogen (N_2) accounts for 78.08%. The next two most abundant gases are argon (Ar) (0.93%) and carbon dioxide (CO_2) (0.04%). To simplify the calculation in this study we assume that O_2 occupies 21% of dry air, N_2 78% and Ar 1% for well mixed dry air by volume. The molar masses of O_2, N_2 and Ar are set equal to 32 g/mol, 28 g/mol and 40 g/mol respectively.

For one mole of O_2, N_2 and Ar, the associated entropies $S_m^{O_2}$, $S_m^{N_2}$ and S_m^{Ar} are given by:

$$S_m^{O_2} = C_{p,m}^{O_2} \ln T - R \ln P^{O_2} + S_{m0}^{O_2} \qquad (6.12)$$

$$S_m^{N_2} = C_{p,m}^{N_2} \ln T - R \ln P^{N_2} + S_{m0}^{N_2} \qquad (6.13)$$

$$S_m^{Ar} = C_{p,m}^{Ar} \ln T - R \ln P^{Ar} + S_{m0}^{Ar} \qquad (6.14)$$

where $C_{p,m}^{O_2}$, $C_{p,m}^{N_2}$ and $C_{p,m}^{Ar}$ represent the molar heat capacities at constant pressure for O_2, N_2 and Ar; P^{O_2}, P^{N_2} and P^{Ar} denote the partial pressures for O_2, N_2 and Ar; $S_{m0}^{O_2}$, $S_{m0}^{N_2}$ and S_{m0}^{Ar} are the related constants of integration. Since O_2 and N_2 are diatomic gases, $C_{p,m}^{O_2}$ and $C_{p,m}^{N_2}$ are set equal

to $\frac{7}{2}R$. Ar is monatomic gas, thus $C_{p,m}^{Ar}$is equal to $\frac{5}{2}R$. Since in this study we are interested in changes in entropy, constants of integration are set to zero. The total entropy of dry air, S_{atm}, in the atmosphere may be expressed then as:

$$S^{atm} = S^{O_2} + S^{N_2} + S^{Ar} \tag{6.15}$$

where $S^{O_2} = \int \left(C_{p,m}^{O_2} \ln T - R \ln P^{O_2}\right) dn_{O_2}$, $S^{N_2} = \int \left(C_{p,m}^{N_2} \ln T - R \ln P^{N_2}\right) dn_{N_2}$ and $S^{Ar} = \int \left(C_{p,m}^{Ar} \ln T - R \ln P^{Ar}\right) dn_{Ar}$ respectively.

The total static energy of dry air, E_{atm}, is given by:

$$E^{atm} = E^{O_2} + E^{N_2} + E^{Ar} \tag{6.16}$$

where $E^{O_2} = \int C_{v,m}^{O_2} T \cdot dn_{O_2} + \int \rho^{O_2} gz \cdot dv$, $E^{N_2} = \int C_{v,m}^{N_2} T \cdot dn_{N_2} + \int \rho^{N_2} gz \cdot dv$ and $E^{Ar} = \int C_{v,m}^{Ar} T \cdot dn_{Ar} + \int \rho^{Ar} gz \cdot dv$ respectively.

For a specific equilibrium temperature, T_{eq}, the partial pressures, $P_{eq}^{O_2}$, $P_{eq}^{N_2}$ and P_{eq}^{Ar}, and the densities, $\rho_{eq}^{O_2}$, $\rho_{eq}^{N_2}$ and ρ_{eq}^{Ar}, for O_2, N_2 and Ar in equilibrium can be quantified according to the principle of mass conservation. For example, $\rho_{eq}^{O_2}$can be computed based on $\int \rho_{eq}^{O_2} \cdot dv = \int \rho^{O_2} \cdot dv$ and $\rho_{eq}^{O_2} = \rho_0^{O_2} \cdot e^{-m_{O_2} gh/(k_B \cdot T_{eq})}$. Subsequently, the entropy, S_{eq}^{atm}, and the static energy, E_{eq}^{atm}, of the atmosphere in equilibrium at T_{eq} can be computed based on equation (6.15) and (6.16).

The continuous line in Figure 6.7 illustrates the function $S_{eq}^{atm}\left(E_{eq}^{atm}\right)$ for the atmosphere. The thermodynamic condition, (E^{atm}, S^{atm}), of the atmosphere on May 30, 2002 is identified by point b in the Entropy-Energy Diagram in Figure 6.7, below the line of $S_{eq}^{atm}\left(E_{eq}^{atm}\right)$,

confirming the fact that the atmosphere was out of thermodynamic equilibrium, with the associated $W_{max} = 29.2\ MJ/m^2$ and $(\Delta S)_{max} = 117\ J/(m^2 \cdot K)$.

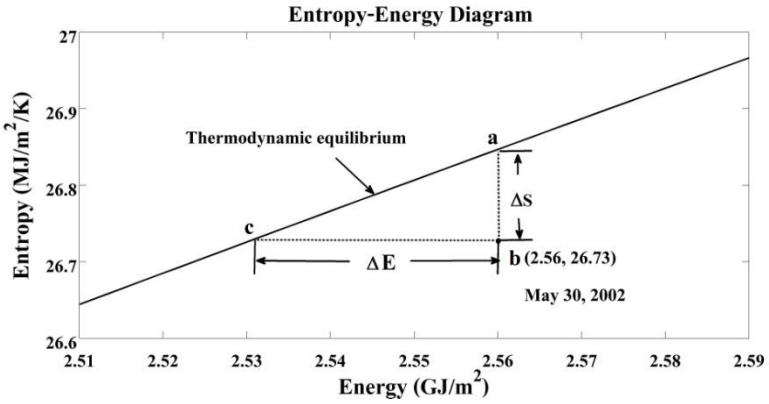

Figure 6.7 The thermodynamic condition, (E^{atm}, S^{atm}), of the atmosphere on May 30, 2002 displayed in an Entropy-Energy Diagram. The ΔE in the figure represents the maximum work, W_{max}, which can be performed in a thermally reversible process; ΔS represents the maximum increase in entropy, $(\Delta S)_{max}$, that can arise in a thermally irreversible process with zero work.

The seasonality of the thermodynamic condition, (E^{atm}, S^{atm}), of the atmosphere in an Entropy-Energy Diagram is plotted in Figure 6.8. The loop-shaped seasonality reflects the asymmetric distribution of land with the equator as the reference. If the land-sea contrast in the Northern Hemisphere had been the same as that in Southern Hemisphere, the thermodynamic condition on June 22 (summer solstice) identified in an Entropy-Energy Diagram would have overlapped by that on December 22 (winter solstice) and the seasonality in Figure 6.7 would have been line-shaped with the conditions of June 22 and December 22 at one end, the conditions for March 21 (vernal equinox) and September 23 (autumnal equinox) at the other.

A greater content of static energy in the atmosphere does not necessarily correspond to higher thermodynamic instability and vice versa. For example, the total static energy on May 1 is

close to that on October 1. Since the associated total entropy on May 1 is greater than on October 1, the atmosphere was thermodynamically more stable on May 1.

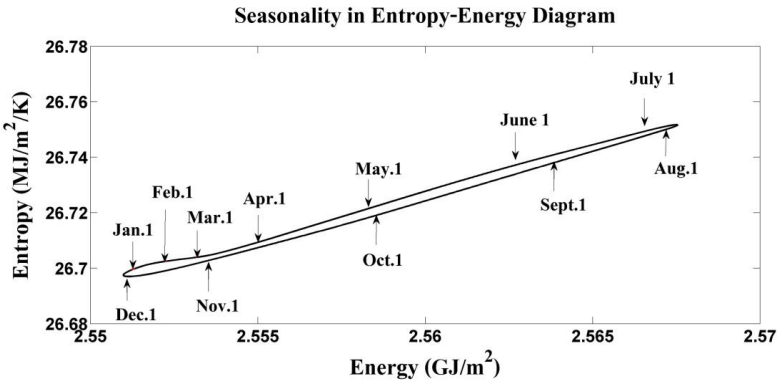

Figure 6.8 The seasonality of the thermodynamic conditions, (E^{atm}, S^{atm}), of the atmosphere in an Entropy-Energy Diagram.

The seasonalities of W_{max} and $(\Delta S)_{max}$ are plotted in Figure 6.9. The atmosphere reaches its state of highest thermodynamic instability in late July with $W_{max} = 31.4\ MJ/m^2$ and $(\Delta S)_{max} = 126\ kJ/(m^2 \cdot K)$, its lowest state in mid January with $W_{max} = 27.7\ MJ/m^2$ and $(\Delta S)_{max} = 112\ kJ/(m^2 \cdot K)$. W_{max} can be approximated as $W_{max} \approx 248K \cdot (\Delta S)_{max}$. Large values of W_{max} are associated with large values of $(\Delta S)_{max}$, corresponding to high states of thermodynamic instability.

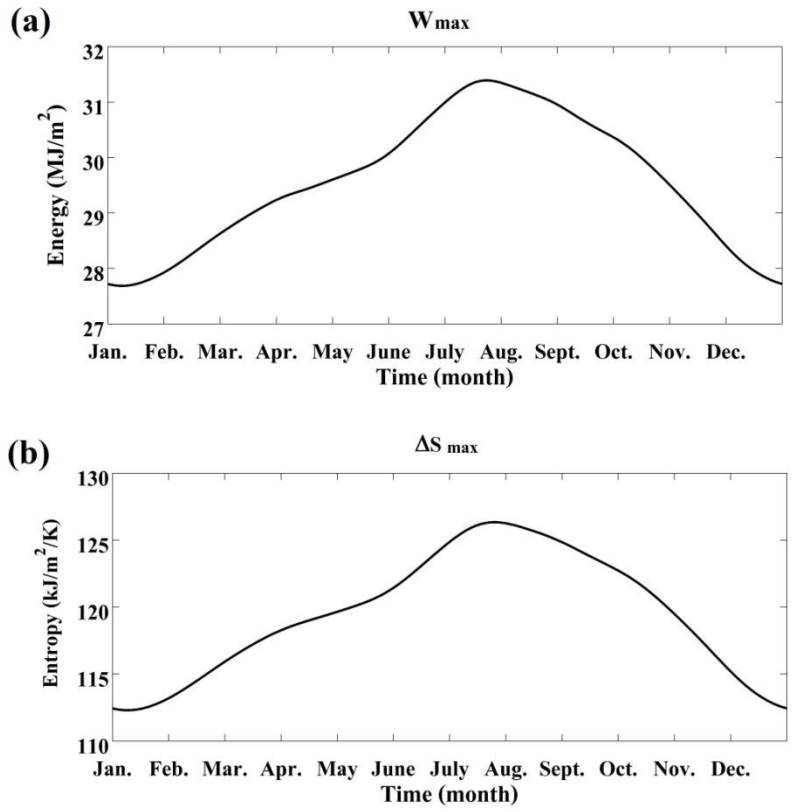

Figure 6.9 The seasonalities of W_{max} and $(\Delta S)_{max}$ based on an average of data for the past 32 years' data.

The long-term variation of W_{max} from January 1979 to December 2010 is illustrated in Figure 6.10. The conspicuous intra-seasonal fluctuation in the red line reflects the strong seasonal variation of the W_{max}. The blue line, computed using a 365-day running average, reflects the existence of an inter-annual variation. Linear regression of the annual mean average over this period provides a regression slope of $2.4\,J/(m^2 \cdot yr)$ with R^2 = 0.004, indicating no statistically significant trend in thermodynamic instability.

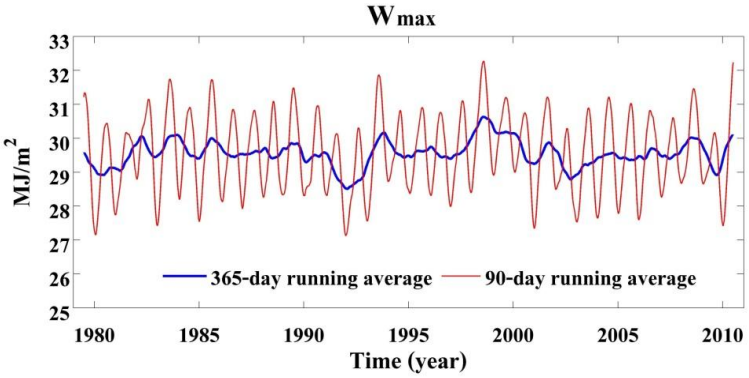

Figure 6.10 Variation of W_{max} from January 1979 to December 2010.

The seasonalities of equilibrium temperatures, T_{eq}^{S} and T_{eq}^{W}, are displayed in Figure 6.11. T_{eq}^{W} is greater than T_{eq}^{S}, reflecting the fact that no work is performed in evolution 2. Both T_{eq}^{S} and T_{eq}^{W} reach their peak values in late July, corresponding to the highest content of static energy as shown in Figure 6.7. The 32-year averaged values for T_{eq}^{S} and T_{eq}^{W} are $248.9\,K$ and $251.8\,K$ respectively. The gap between T_{eq}^{S} and T_{eq}^{W} reflects the thermodynamic instability of the atmosphere.

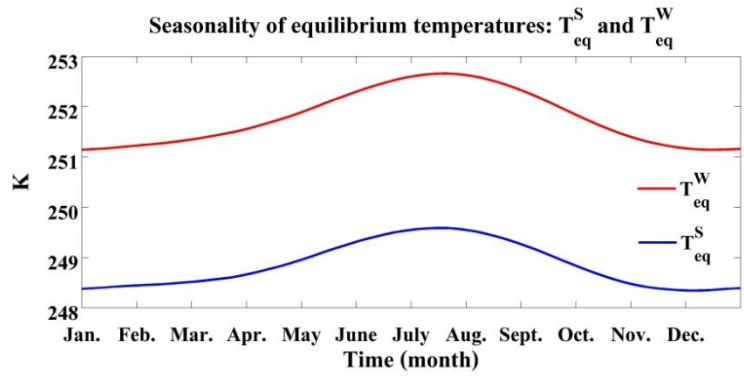

Figure 6.11 The seasonalities of the equilibrium temperatures, T_{eq}^{S} and T_{eq}^{W}, based on an average of data for the past 32 years' data.

In this study, the variation of T_{eq}^{S} is indicated by:

$$\Delta T_{eq}^{S} = T_{eq}^{S} - 248.5K \tag{6.17}$$

and the variation of T_{eq}^{W} is defined by:

$$\Delta T_{eq}^{W} = T_{eq}^{W} - 251.5K \tag{6.18}$$

The variation of T_{eq}^{S} and T_{eq}^{W} with the seasonal cycle removed is shown in Figure 6.12. The increases of ΔT_{eq}^{S} and ΔT_{eq}^{W} generally follow the global surface temperature change, $\Delta T_{surface}$, with the correlation between ΔT_{eq}^{S} and $\Delta T_{surface}$ equal to 0.87 and correlation between ΔT_{eq}^{W} and $\Delta T_{surface}$ equal to 0.91. Thus, as the global surface temperature increased from January 1979 to December 2010, the thermodynamic conditions (E^{atm}, S^{atm}) of the atmosphere on an Energy-Entropy Diagram moved on a trajectory parallel to the line of $S_{eq}^{atm}(E_{eq}^{atm})$ in Figure 6.7, resulting in increases in T_{eq}^{S} and T_{eq}^{W}, with W_{max} and $(\Delta S)_{max}$ remaining relatively constant.

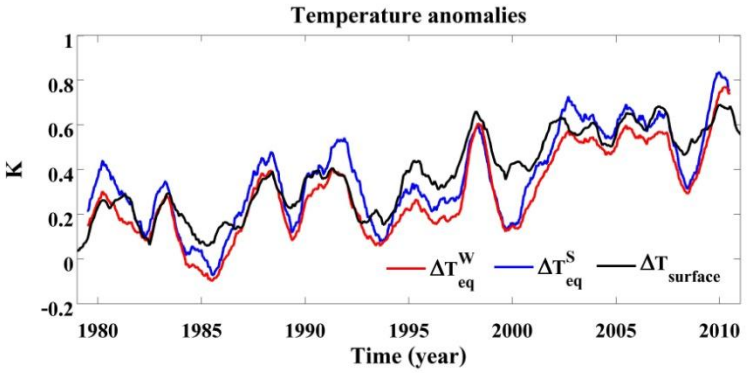

Figure 6.12 Variation of ΔT_{eq}^{S}, ΔT_{eq}^{W} and $\Delta T_{surface}$ from January 1979 to December 2010.

6.6 Discussion and Summary

This study presented an approach for analysis of the relationship among temperature, energy and entropy of the atmosphere, and proposed two variables, W_{max} and $(\Delta S)_{max}$, as measures of the thermodynamic instability of the atmosphere. W_{max} is approximately a linear function of $(\Delta S)_{max}$: $W_{max} \approx 248K \cdot (\Delta S)_{max}$. The annual mean value of W_{max} was estimated at 29.6 MJ/m^2 with 31.0 MJ/m^2 for JJA and 28.0 MJ/m^2 for DJF.

Based on the same assimilated meteorological dataset as used in this study, Kim and Kim (2013) estimated the global averaged APE at 4.34 MJ/m^2 for the annual mean, 4.02 MJ/m^2 for JJA and 4.75 MJ/m^2 for DJF. There are considerable differences in the absolute values and magnitudes of the seasonal cycles for APE and W_{max}.

Figure 6.13 provides a schematic illustration of the relationship between APE and W_{max} with point b corresponding to the thermodynamic condition, (E^{atm}, S^{atm}). APE is defined as the difference in total static energy between the current state of the dry air component of the atmosphere and that of an idealized reference state corresponding to the minimum content of static energy present following a sequence of reversible isentropic transformations. When the atmosphere fully releases its APE through a isentropic and adiabatic process to perform mechanical work and reaches the associated reference state, the total value of S^{atm} should stay constant. On the Entropy-Energy Diagram in Figure 6.13, this process corresponds to a thermodynamic transition from point b to point d with entropy preserved. However, the reference state in mechanical equilibrium is not in thermal equilibrium, and the maximum work, W_{max}, has not as yet been completely exerted. Thus, APE corresponding to the b-to-d displacement in Figure 6.13 should be smaller than W_{max} corresponding to the b-to-d

displacement in Figure 6.13. It follows that APE may be considered as the mechanical component of W_{max}.

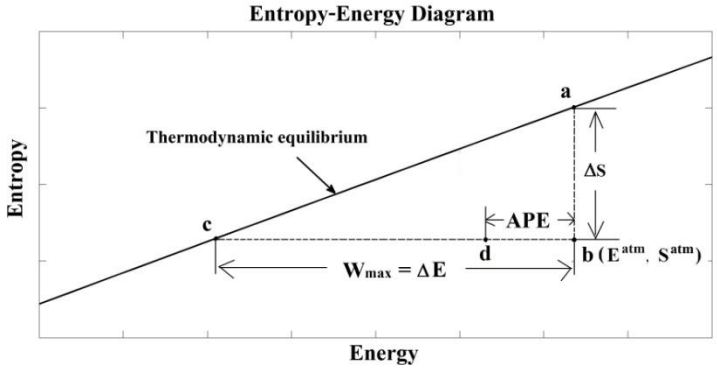

Figure 6.13 Schematic illustration of the relationship between APE and W_{max}. The distance between b and d represents APE, and the distance between b and c represents W_{max}.

Figure 6.14 presents a schematic illustration of the c-to-d displacement in Figure 6.13. The upper panels in Figure 6.14 display the zonal-average potential temperature, θ, and zonal-average temperature, T, appropriate for the associated reference state proposed by Lorenz, with its thermodynamic condition, (E^{atm}, S^{atm}), corresponding to point d in Figure 6.13. The lower panels display zonal-average potential temperatures, θ, and zonal-average temperatures, T, for the associated thermodynamic equilibrium state with its thermodynamic condition, (E^{atm}, S^{atm}), corresponding to point c in Figure 6.13. When the thermal non-equilibrium reference state proposed by Lorenz approaches thermodynamic equilibrium through Evolution 1, an amount of work equal to $(W_{max} - APE)$ is performed.

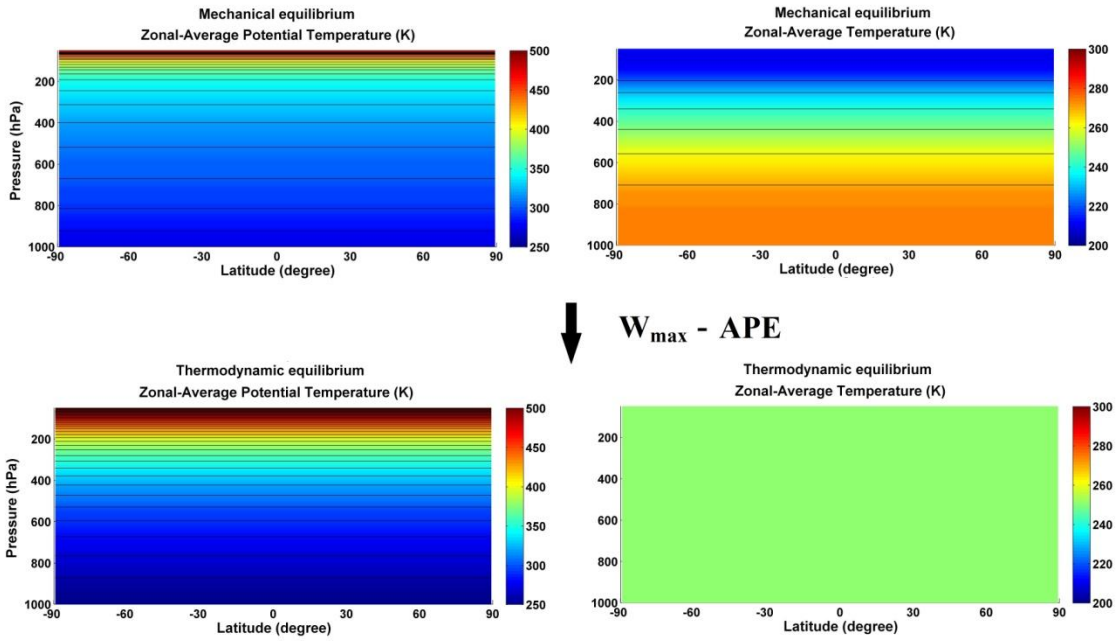

Figure 6.14 Schematic illustration of $(W_{max} - APE)$. The upper panels display zonal-average potential temperatures, θ, and zonal-average temperatures, T, for the associated reference state proposed by Lorenz. The lower panels present zonal-average potential temperatures, θ, and zonal-average temperatures, T, for the associated thermodynamic equilibrium state.

According to Kim and Kim (2013), APE changes by $(4.75 - 4.02)\ MJ/m^2 = 0.73\ MJ/m^2$ from JJA to DJF. Whereas, based on this study, W_{max} changes by $(28.0\ - 31.0)\ MJ/m^2 = -3.0\ MJ/m^2$ from JJA to DJF. If atmospheric phenomena provided solely with expenditure of APE, which constitutes a fraction of W_{max}, APE and W_{max} should have fluctuated on the same pace. The difference in magnitudes of the seasonal cycles indicates that the LEC theory may not fully explain the energetics of the atmosphere. A key question is how W_{max} is consumed by atmospheric processes while sustaining the general circulation. In the LEC theory, Lorenz developed a framework illustrating the creation term and consumption term of APE. A

counterpart framework illustrating the source and sink terms for W_{max} should be identified in future studies.

Regarding the long-term variability of W_{max}, as the global surface temperature, $T_{surface}$, increased from January 1979 to December 2010, the equilibrium temperatures, T_{eq}^{S} and T_{eq}^{W}, increased at about the same pace as $T_{surface}$. Consequently, there was no statistically significant trend in W_{max} over this interval. It is important to understand how the atmosphere adjusted its thermodynamic structure over this period, including its vertical temperature profile in order to maintain a relatively constant W_{max}. A number of studies pointed out that the lower-tropospheric temperatures have experienced slightly greater warming since 1958 than those at the surface. Lower-stratospheric temperatures have exhibited cooling since 1979 while tropopause height has increased by 200m between 1979 and 2001 (e.g. Randel et al. 2000; Grody et al. 2004; Santer et al. 2004; Simmons et al. 2004; Fu and Johanson 2005; Karl et al. 2006; Vinnikov et al. 2006). It is important to explore the pertinent implications for W_{max}.

The global thermodynamic instability of the atmosphere was analyzed retrospectively in this study based on the MERRA data. A relevant question is whether the conclusions reached here may be conditioned by the use of this specific data base. Other datasets including NCEP-1, NCEP-2, ERA-40 and JRA-25 should be employed in future work to compare with the results presented here.

Acknowledgements

The work described here was supported by the National Science Foundation. Junling Huang was also supported by the Harvard Graduate Consortium on Energy and Environment. We acknowledge helpful and constructive comments from Michael J. Aziz, Eli Tziperman, Brian F. Farrell and Zhiming Kuang.

References

Bannon, P. R., 2012: Atmospheric Available Energy. *J. Atmos. Sci.*, **69**, 3745-3762.

Becker, E., 2009: Sensitivity of the upper mesosphere to the Lorenz energy cycle of the troposphere. *J. Atmos. Sci.*, **66**, 647-666.

Boer, G. J., and S. Lambert, 2008: The energy cycle in atmospheric models. *Climate dynamics*, **30**, 371-390.

De Groot, S. R. and P. Mazur, 2013: Non-equilibrium thermodynamics. Courier Dover Publications.

Dutton, J. A., 1973: The global thermodynamics of atmospheric motion. *Tellus*, **25**, 89-110.

Goody, R., 2000: Sources and sinks of climate entropy. *Q. J. R. Meteorol. Soc.*, **126**, 1953-1970.

Goody, R. and W. Abdou, 1996: Reversible and irreversible sources of radiation entropy. *Quarterly Journal of the Royal Meteorological Society*, **122**, 483-494.

Grody, N. C., K. Y. Vinnikov, M. D. Goldberg, J. T. Sullivan, and J. D. Tarpley, 2004: Calibration of multisatellite observations for climatic studies: Microwave Sounding Unit (MSU). *J. Geophys. Res.: Atmos.*, **109**, 24.

Fu, Q., and C. M. Johanson, 2005: Satellite-derived vertical dependence of tropical tropospheric temperature trends. *Geophys. Res. Lett.*, **32**, 10.

Hansen, J., R. Ruedy, M. Sato and K. Lo, 2010: Global surface temperature change. *Rev. Geophys.*, **48**, RG4004.

Hernández-Deckers, D., and J. S. von Storch: 2010: Energetics Responses to Increases in Greenhouse Gas Concentration. *J. Climate*, **23**, 3874-3887.

Huang, J., and M. McElroy, 2014: Contributions of the Hadley and Ferrel Circulations to the Energetics of the Atmosphere over the past 32-years. *J. Climate.*, **27**, 2656-2666.

Karl, T. R., S. J. Hassol, C. D. Miller and W. L. Murray, 2006: Temperature trends in the lower atmosphere. steps for understanding and reconciling differences.

Landau, L. D., and E. M. Lifshitz, 1980: Statistical physics, vol. 5. Course of Theoretical Physics, 30.

Li, L., A. P. Ingersoll, X. Jiang, D. Feldman, Y. L. Yung, 2007: Lorenz energy cycle of the global atmosphere based on reanalysis datasets. *Geophys. Res. Lett.*, **16**, L16813.

Lorenz, E. N., 1955: Available potential energy and the maintenance of the general circulation. *Tellus*, **7**, 157-167.

Lorenz, E.N., 1967: The natural and theory of the general circulation of the atmosphere. World Meteorological Organization, 161pp.

Lucarini, V., K. Fraedrich and F. Ragone, 2011: New Results on the Thermodynamic Properties of the Climate System. *J. Atmos. Sci.*, **68**, 2438-2458.

Marques, C. A., A. Rocha, J. Corte-Real, J. M. Castanheira, J. Ferreira, and P. Melo-Gonçalves, 2009: Global atmospheric energetics from NCEP–Reanalysis 2 and ECMWF–ERA40 Reanalysis. *International Journal of Climatology*, **29**, 159-174.

Marques, C. A. F., A. Rocha, and J. Corte-Real, 2010: Comparative energetics of ERA-40, JRA-25 and NCEP-R2 reanalysis, in the wave number domain. *Dynamics of Atmospheres and Oceans*, **50**, 375-399.

Marques, C. A. F., Rocha, A. and J. Corte-Real, 2011: Global diagnostic energetics of five state-of-the-art climate models. *Climate dynamics*, **36**, 1767-1794.

Oort, A. H., and J. P. Peixóto, 1974: The annual cycle of the energetics of the atmosphere on a planetary scale. *J. Geophys. Res.*, **79**, 2705-2719.
Oort, A. H., and J. P. Peixóto: 1976: On the variability of the atmospheric energy cycle within a 5-year period. *J. Geophys. Res.,* **81**, 3643-3659.

Ozawa, H., A. Ohmura, R.D. Lorenz and T. Pujol, 2003: The second law of thermodynamics and the global climate system: a review of the maximum entropy production principle. *Rev. Geophys.*, **41**, 4.

Paltridge, G. W., 1975: Global dynamics and climate - a system of minimum entropy exchange. *Q. J. R. Meteorol. Soc.*, **101**, 475-484.

Paltridge, G. W., 2001: A physical basis for a maximum of thermodynamic dissipation of the climate system. *Q. J. R. Meteorol. Soc*, **127**, 305-313.

Pauluis, O. and I.M. Held, 2002a: Entropy Budget of an Atmosphere in Radiative–Convective Equilibrium. Part I: Maximum Work and Frictional Dissipation. *J. Atmos. Sci.*, **59**, 125-139.

Pauluis, O. and I.M. Held, 2002b: Entropy Budget of an Atmosphere in Radiative–Convective Equilibrium. Part II: Latent Heat Transport and Moist Processes. *J. Atmos. Sci.*, **59**, 140-149.

Peixoto, J. P., and A. H. Oort, 1992: *Physics of climate*. American institute of physics, 520pp.

Peixoto, J. P. and A. H. Oort, M. De Almeida, A. Tomé, 1991: Entropy budget of the atmosphere. *J. Geophys. Res.: Atmos.*, **96**, 10981-10988.

Pauluis, O., 2007: Sources and Sinks of Available Potential Energy in a Moist Atmosphere. *J. Atmos. Sci.*, **64**, 2627-2641.

Prigogine, I., 1962: Introduction to non-equilibrium thermodynamics. Jonh Wiley & Sons, NY.

Rienecker, M., et al., 2007: The GEOS-5 data assimilation system—Documentation of versions 5.0.1 and 5.1.0. NASA GSFC, Tech. Rep. Series on Global Modeling and Data Assimilation, NASA/TM-2007-104606, Vol. 27.

Randel, W. J., F. Wu, and D. J. Gaffen, 2000: Interannual variability of the tropical tropopause derived from radiosonde data and NCEP reanalyses. *J. Geophys. Res.: Atmos.*, **105**, 15509-15523.

Romps, D. M., 2008: The dry-entropy budget of a moist atmosphere. *J. Atmos. Sci.*, **65**, 3779-3799.

Santer, B. D. and et al., 2004: Identification of anthropogenic climate change using a second generation reanalysis. *J. Geophys. Res.: Atmos.*, **109**, 21.

Simmons, A. J. and et al., 2004: Comparison of trends and low-frequency variability in CRU, ERA-40, and NCEP/NCAR analyses of surface air temperature. *J. Geophys. Res.: Atmos.*, **109**, 24.

Vinnikov, K. Y., N. C. Grody, A. Robock, R. J. Stouffer, P. D. Jones and M. D. Goldberg, 2006; Temperature trends at the surface and in the troposphere. *J. Geophys. Res.: Atmos.*, **111**, 3.

Wulf, O. R. and L. Davis Jr, 1952: On the efficiency of the engine driving the atmospheric circulation. *J. Meteorol.*, **9**, 80-82.